國立交通大學

機械工程學系

博 士 論 文

渦卷壓縮機軸向順從機構設計與應用之研究

Research on Design and Applications of Axial-compliance Mechanism for Scroll-type Compressors

研 究 生：湯岳儒

指導教授：洪景華　教授

中 華 民 國 一 百 零 二 年 一 月

渦卷壓縮機軸向順從機構設計與應用之研究

Research on Design and Applications of Axial-compliance Mechanism for Scroll-type Compressors

研 究 生：湯岳儒　　Student：Yuehju Tang

指導教授：洪景華　　Advisor：Chinghua Hung

國 立 交 通 大 學
機 械 工 程 學 系
博 士 論 文

A Dissertation
Submitted to Department of Mechanical Engineering
College of Engineering
National Chiao Tung University
in partial Fulfillment of the Requirements
for the Degree of
Doctor of Philosophy
In
Mechanical Engineering

January 2013

Hsinchu, Taiwan, Republic of China

中華民國一百零二年一月

渦卷壓縮機軸向順從機構設計與應用之研究

研究生：湯岳儒　　指導教授：洪景華 教授

國立交通大學機械工程學系博士班

摘 要

對於講究節能環保的現代化高效率變頻冷凍空調系統而言，搭載直流無刷變頻馬達之變頻渦卷式壓縮機已成為技術發展之主流。而欲克服渦卷壓縮機因應變頻容量調節伴隨而來的容積壓縮效率變化問題，首要解決之關鍵便是變頻壓縮泵的內部洩漏問題。本研究所探討之渦卷壓縮機軸向順從機構，由作用於固定渦卷背部的背壓機構與提供渦卷間隙控制的懸吊機構所組成。此順從機構可動態調整渦卷間隙使維持於一固定最佳值，以減少當負載變動時因渦卷壓縮腔室間的內部洩漏所造成的容積壓縮效率變化，使渦卷壓縮機得以在負載變動時可持續維持高容積效率。

用於實現高性能變頻低壓外殼型渦卷壓縮機的幾個軸向順從機構的關鍵技術已在本研究中完成開發與調查。首先進行軸向洩漏路徑幾何數學模型建構與數值模擬分析研究，隨後實際開發一軸向順從機構，並裝置於一低壓外殼 R22 冷媒空調變頻渦卷壓縮機雛型進行性能測試。實驗結果證實，藉由適當的順從機構設計，在各種轉速操作條件，皆可維持雛型壓縮機的高容積效率。而實測結果亦發現，軸向順從機構的作用能擴展空調用渦卷壓縮機可變轉速操作範圍至更高及更低轉速，並提升效率 4.7%~13.5%。此外，由實測觀察發現，此軸向順從機構尚可減輕低壓外殼型壓縮機泵體機件運轉碰撞之噪音問題。

最後，為驗證所研究的軸向順從機構設計原理可廣泛適用於不同種冷媒之應用，實際

進行了 R410A 及 R744(CO_2)冷媒低壓外殼型渦卷壓縮機雛型開發案例研究，其中導入有限元素法協助進行軸向順從機構設計變更。實驗證實，本研究之軸向順從機構可成功應用於不同種冷媒之壓縮機應用。

關鍵字：*變頻冷凍空調、渦卷式壓縮機、洩漏、軸向順從機構、軸向間隙*

Research on Design and Applications of Axial-compliance Mechanism for Scroll-type Compressors

Student：Yuehju Tang **Advisor：Dr. Chinghua Hung**

Department of Mechanical Engineering
National Chiao Tung University

ABSTRACT

A variable-speed scroll-type compressor (STC) with brushless DC convertor motor has become the mainstream of the technological development because of the requirements for energy-saving and environmental protection in modern high-efficiency inverter refrigeration and air conditioning systems. To overcome the problem of the volume compression efficiency change by the inverter capacity adjusting, the primary key to the solution is to solve the internal leakage problem of the variable-speed compression pump.

In this study, the axial-compliance mechanism (ACM), which is composed of a backpressure regulating mechanism acting on the fixed scroll back and a suspension mechanism controlling the scroll clearance, was studied. The use of the ACM enables dynamical adjustments, which allow the scroll clearance to be maintained at a fixed optimal value in order to reduce the varying of volume compression efficiency by the internal leakage in the scroll compression chambers and the high volumetric efficiency can thus be maintained while the system load changed.

Several critical techniques for accomplishing a high-performance, variable-speed low-pressure-side (LPS) STC with an ACM have been developed and investigated. First, the

mathematical model of axial leakage value was constructed, and the advantages of this model were confirmed by numerical simulations and experimental validations with the developed ACM in an R22 LPS STC prototype. The experimental results showed that if the compliance mechanism is designed appropriately, the compressor can achieve a high volumetric efficiency, irrespective of the operating speed conditions. Because of the ACM, the speed range of the variable-speed scroll compressor can be extended and the efficiency can be improved by 4.7–13.5%. In addition, from the experimental observations, a fact was discovered that the ACM can also reduce the noise between the colliding components of the LPS STC.

Finally, for the understanding and verification of the proposed ACM design method could be extended its application to different refrigerant STCs. Case studies of a R410A and a R744 (CO_2) applications in the LPS STC prototypes was formulated in this study. Furthermore, the application of the finite element method was introduced for the ACM mechanism design changes. From the experiment results, the proposed ACM design methods can successfully applications in these different refrigerant STCs.

Keywords: *Inverter air conditioner, Scroll type compressor, Leakage, Axial-compliance mechanism, axial clearance*

誌 謝

感謝洪錫源老師引領學生進入創造知識的研究行列，在博班求學的前三年鼓勵學生將職場與學校的工作鏈結起來，激發學生對研究的興趣與對探索未知的熱忱，在您指導期間，學生著實受益良多。學生在此更要由衷感謝指導教授洪景華老師，願意不辭辛勞地延續指導學生的博士研究工作，在研究過程中適時給予學生信心與鼓勵，除幫助學生建立專業領域的學養與知識外，更引領學生培養獨立研究的精神與嚴謹的邏輯思維，讓學生得以順利完成博士論文，邁向新的階段。

非常感謝口試委員，宋震國教授、陳俊勳教授、馮展華教授、張鈺炯博士和陳伸岳博士，感謝您們在百忙中仍願意撥空冒著寒風細雨來參加學生的學位口試，感謝您們提出諸多寶貴的建議與指導，讓學生的論文可以更加完整。

求學期間特別要感謝能源局經費支持，使學生能順利進行各項研究工作，感謝工研院的長官與同事們的諸多照顧與提攜，也要感謝實驗室學長與學弟妹們多年的幫助與關懷。

細數在交大歷經八個寒暑的學生生涯，有辛勞也有歡樂，求學階段雖將告一段落，然而更漫長的人生學習才正要開始。雖然，這一路帶職求學的旅程，辛苦多於快樂，尤其是面臨工作的轉換、生活的壓力以及指導教授的變更，種種無形的壓力讓我常常陷入低潮，甚至一度想放棄學業，在此要感謝我的家人們在精神上給予無限的支持與鼓勵，在這段期間，親情是我最大的精神支柱。

最後，謹以此論文獻給我最敬愛上帝、我的雙親與我的愛妻。

TABLE OF CONTENTS

LIST OF TABLES

LIST OF FIGURES

NOMENCLATURE

A	cross-sectional area of the check valve, mm^2
A_d	discharge chamber area, mm^2
A_m	middle chamber area, mm^2
A_s	suction chamber area, mm^2
B	scroll height, mm
CR	system pressure ratio
Dl	inner diameter of pipe, m
D	cylinder diameter, mm
f	friction factor
F_b	backpressure gas force, N
F_{boss}	gas force on boss, N
F_{bd}	solid (body) force, N
F_{disk}	disk spring force, N
F_g	axial gas force, N
F_m	tangential accelerate force of scroll, N
F_θ	tangential gas force, N
F_{pd}	net forces resulting from pressure difference, N
F_{pin}	gas force on pin, N
F_{spring}	leaf spring force, N
F_t	tangential force, N
F_{tx}	contact force, N
F_chamber	chamber gas force, N
F_lower	lower (suction) gas force, N
F_backpressure	backpressure gas force, N
g	acceleration due to gravity, m/s^2
hf	head loss, m
Io	moment of crankshaft, N-m
K	spring stiffness
l	scroll wrap thickness, mm
L	sealing line length, mm
Ll	length of pipe, m
L_b	orbiting bias, mm

$L_{leakage,center}$	center leakage path, mm
$L_{leakage,circle}$	circle leakage path, mm
M	tilting moment, N-m
M_{Φ}	Transfer matrix
Ms	Orbiting scroll mass, kg
Mo	Oldham ring mass, kg
n	normal vector of mesh point
n_f	inner normal vector of mesh point
n_o	outer normal vector of mesh point
N	number of the leaf spring
P	pressure, MPa
P_{cond}	saturated condenser pressure, MPa
P_d	discharge pressure, MPa
P_{eva}	saturated evaporator pressure, MPa
Pin_area	backpressure pin area, mm^2
P_m	medium pressure, MPa
P_o	outer pressure, MPa
P_s	suction pressure, MPa
P_i	inner pressure, MPa
r	involute basic circle radius, mm
r_b	base circle radius, mm
r_m	mean radius, mm
ro	crankshaft radius, mm
rs	crankpin radius, mm
R	scroll wrap function
R_e	Reynolds number
R_f	fixed-scroll wrap function
R_o	orbiting-scroll wrap function
R_p	compressor pressure ratio
R_{lc}	point of tooling edge
R_{io}	inner scroll profile
R_{fo}	outer scroll profile
R_{oi}	inner orbiting scroll profile

R_{oo}	outer orbiting scroll profile
R_{β}	moving vector of orbiting scroll
s	involute length, mm
S_1	cutting tool center
T	temperature, ℃
t	scroll thickness, mm
T_{abi}	environmental temperature, ℃
T_e	evaporator temperature, ℃
T_s	suction temperature, ℃
T_p	scroll pitch, mm
T_condensor	temperature of condenser, ℃
T_{vi}	pressure valve temperature, ℃
V_1	fixed scroll velocity, m/s
V_2	tool movement velocity, m/s
V_{12}	relative velocity, m/s
Vs	suction volume, cm^3
v	velocity of fluid, m/s
X	displacement of leaf spring, mm
Xc	involute x coordinate
Yc	involute y coordinate

Greek letters

τ	unit tangential vector
μ_{mn}	mean dynamic viscosity, Pa · s
ρ_{mn}	mean fluid density, kg/cm^3
δ	scroll clearance; scroll gap, μm
δ_a	axial clearance, μm
δ_r	radial clearance, μm
u	flow velocity in x direction
v	flow velocity in y direction
υ	average viscosity, rad/s
ω	tooling angular velocity, rad/s
φ	involute extension angle, rad
φi	involute angle of the scroll, rad
θ	involute angle, rad

ς	angle between the modified straight line and the x axis
ξ	constant
λ_a	axial empirical friction factor
λ_r	radial empirical friction factor
ΔP	pressure difference, MPa
κ	specific heat ratio

Subscripts

axial	axial direction
ar	argument
b	base circle
c	center position
dis	discharge
e	end-side
fi_i	inner involute of fixed scroll
fi_o	outer involute of fixed scroll
g	gas
l,e	end-side leakage
l,f	flank leakage
ob	orbiting scroll
r	radial direction
t	tangent coordinate
tu	tube

CHAPTER 1 INTRODUCTION

1.1 Background

A scroll-type compressor (STC) (Fig. 1.1) is a kind of positive displacement compressor that is capable of both intake and exhaust in one compression cycle and has high efficiency, low noise, and few components. The concept for STC was derived from the U.S. Patent (Rotary Engine) granted to L. Creux in 1905 [1]. However, the name "scroll compressor" (or involute) was not used until the announcement of the U.S. Patent (Scroll Pump) by J. L. Jones in 1958 [2]. The STC has been extensively developed since the 1980s because of the great improvement in computerized numerical control milling. Further, it has been widely used by Hitachi since 1983 in small air conditioners.

The STC pump has two main components: a fixed scroll and an orbiting scroll. Each scroll has a circular base plate and an involute (spiral) profile protrusion extended from the plate surface. The involute wall has often been called a "scroll". Fig. 1.2 shows the compression cycle of the STC. The scroll pair compresses the gas from the suction port into the chambers and pushes it progressively toward the center, gradually decreasing the volume of the gas until it reaches the discharger step. In this step, the gas is exhausted through the discharge port of the fixed scroll and then out of the STC to the condenser. Usually, after three rounds in the compression circle, the STC begins its simultaneous compression and discharge movements in several continuous symmetrical chambers. Therefore, the STC is operated with a low torque variation, low noise, and low vibration. Because of the absence of suction or discharge valves in the STC, the gas pulsation and flow losses can be reduced; this results in a smooth flow pattern, which indicates that the STC can start and restart easily. In addition, low flow losses result in a high volumetric efficiency, smooth operation, and high reliability.

Today, with the strengthening of effects of global warming and increase in awareness about energy conservation, attention worldwide has been focused on developing highly efficient compressors that consume low power. Therefore, in recent years, variable-speed STCs demonstrating optimum efficiency under different operating conditions have been studied. The operating conditions can be indicated and defined as the ratio of the saturated condenser pressure to the saturated evaporator pressure (P_{cond}/P_{eva}) and can thus be determined for ambient operating

conditions. Further, the pressure ratio comes from the air-conditioner (or refrigerator) system phenomenon, and this influences the inner pressure difference (P_d/P_s) in the STC.

In general, the inner pressure difference arises from the compressor pressure ratio (volumetric ratio) has been fixed, as the geometrical parameters of the STC are set beforehand. The intrinsic limitation of the fixed volumetric ratio and the mismatch between the pressure and volumetric ratios of the STC cause over-compression or under-compression. Interestingly, inner leakage also causes a mismatch between the pressure and volume ratios. Thus, repetitive compression occurs and extra power is consumed.

Nevertheless, repetitive compression can be reduced by using a compliance mechanism incorporated in the fixed scroll to reduce inner leakage. However, tip leakage is a more serious problem than flank leakage [3]. Application of the axial-compliance mechanism (ACM) can decrease the inner leakage to match the varying operating conditions. Therefore, using the ACM, we can design and produce an STC having superior efficiency.

1.2 Motivation and objectives

For the energy-saving and environmental protection in modern high-efficiency inverter refrigeration and air conditioning systems, it is very important to improve the power consumption efficiency of the compressors.

In this study, the improvement of the STC's performance is by introducing a new leakage-controlled mechanism, so called axial-compliance mechanism (ACM), to solve the internal leakage problem. However, the ACM mechanism design concept is come from patent research. For the understanding of the leakage mass flow rate is determined by the scroll profile, scroll constructions, scroll clearance size and operating conditions of the compressor. This study constructs a simple leakage model (transform the involute leakage path to a circular path) and integrates it into the developed STC-performance simulation package. From the numerically calculate using the STC package, the objective is to find out the best axial scroll clearance for design the optimum ACM and figure out the novel ACM design method.

Then the objective is to verify the proposed novel ACM which can maintain the best

clearance in an inverter driven variable-speed STC prototype. From the results of the experiments, the newly developed axial-compliance design should cause a considerable improvement in performance at both low and high operating speeds. Finally, the proposed ACM should be verified that it can apply in different refrigerant application with suitable design change.

1.3 Axial-compliance sealing methods

As the inner leakage can be minimized by several sealing mechanisms, it is important to solve the pressure-difference problem caused by the scroll pump for improving the sealing mechanism. This study has categorized the axial-sealing mechanisms for driving pressure difference into sealing forces. By reviewing over a thousand U.S. patents, we categorized the axial-sealing mechanisms of the scroll machines into four types:

(1) Tip sealing means on scroll wraps,

(2) Applying backpressure gas force to the back surface of the orbiting scroll,

(3) Applying backpressure gas force to the back surface of the fixed scroll,

(4) Using pressure members at the back of the fixed or orbiting scroll (or both),

(1) Tip sealing parts on scroll wraps

This kind of sealing method uses axial compliance with sealing parts to provide STC sealing. These parts comprise seal elements associated with the involute wraps, and the axial force forms a sealing contact with the end plates of the opposing scroll. The axial force may be applied pneumatically or mechanically. The axial contact resulting from the axial force is used to maintain the integrity of the radial sealing within the apparatus. The use of the axial compliance sealing allows the established contact between the end plates of the opposing scroll. The radial seal is machined to conventional accuracy and provides automatic compensation for temperature differentials and for any uneven wear of the scrolls.

(2) Applying backpressure gas force to the back surface of the orbiting scroll

This kind of sealing method uses an intermediate-pressure-level gas drawn from the operating scroll pump chambers during compression. This gas force is applied to the entire area of the back of the orbiting scroll to force the orbiting scroll tightly against the fixed scroll for providing an axial seal to the pair of scrolls.

(3) Applying backpressure gas force to the back surface of the fixed scroll

This kind of sealing method is used to enhance the axial sealing for a scroll machine, including a mu1ti-function floating seal, for isolating the axial biasing fluid from the working fluid under pressure; further, this method provides vacuum protection and maintains a high pressure ratio.

(4) Using pressure members at the back of the fixed or orbiting scroll (or both)

This kind of sealing method involves the use of a frame member having a thrust surface adjacent to the back surface of the orbiting scroll. A non-sea1ing stabilizer ring is disposed between the frame member and the orbiting scroll to eliminate the wobbles resulting from small perturbations. A stabilizer ring is mechanically or positively spring-loaded by a wave spring to axial force the orbiting scroll toward the fixed scroll.

Fig. 1.7 shows the gas–pressure distribution. The axial pressures cause the scrolls to separate. The tangential forces (F_θ & F_m) result in an overturning moment and cause the scrolls to wobble. Both of these behaviors result in leakage. The above sealing methods are used to solve the leakage problem using the four basic mechanisms.

Appendix A listed the Details of patents on the research and analysis of axial sealing.

1.4 Variable-speed STC

The STC was designed for operation at a constant speed by using a single-phase or multiphase induction motor for traditional refrigeration applications. This implies that the STC was suitable only for a specified operating condition or for thermal loading (cooling or heating capacity) with its best performance. If the STC was operated out of the specified condition, the performance decreased. In other words, the STC operating under one condition has high performance, but deviation from this specific operating condition results in various types of thermal loading owing to varied environmental temperatures.

Hence, in the traditional refrigeration applications, the STC switching on/off to match the different types of thermal loading once the environmental temperature changed. However, these switching actions caused unnecessary power consumption with loud noise and large vibrations in the pipes and the frame of the STC. Therefore, the STC did not have high efficiency when the operating speed increasing beyond the specific design point. The best approach for correcting the problem of on/off control of the constant-speed STC is to match the capacity of the air conditioner to the variation in thermal load. According to past research, the best solution is to use a variable-speed compressor for providing variable cooling capacity [4].

An inverter-fed controller for providing much cooling capacity to the varying thermal load drives the variable-speed compressor, which uses a variable-speed motor. In addition, the variable-speed compressor can replace a series of traditional constant-speed compressors. However, in order to enable variable-speed operation, balancing the inner forces and moments is essential. The best candidate for the variable-speed air conditioning system would be the STC wherein the chambers are compressed and discharged simultaneously at any speed and the characteristics of loading condition results in low-level vibration and small change in torque [5]. Therefore, the fluctuation in speed and the extent of mechanical vibration in the STC are considerably lower than those in the other types are. Because of the developed variable-speed STC, in this study, we implement an equivalent STC with an ACM to match the required performance under the extended operating conditions. Meanwhile, the performances of the developed STC with and without the ACM are compared.

1.5 Different sealing in low-side and high-side STCs

Two major configurations with different types of gas distribution housing are used in STCs: low (-pressure)-side (LPS) type and high (-pressure)-side (HPS) type. In the low-side type, the motor and the scroll set are located on the suction pressure side. The suction gas passes through the housing into the chamber around the compressor's mechanism and motor. On the other hand, in the high-side type, the housing is filled with discharge pressure and the inlet is directly connected to the suction cavity.

Fig. 1.8 shows the schematics of these two types of STCs. The selection of shell configuration is a key determinant in STC design. The design configurations, forces generated by the scroll set during compression, leakage models, sealing mechanisms, oil lubricating flow designs, temperature distributions, noise controlling strategies, etc., are different for both types of STCs.

In 1992, Richardson and Gatecliff [6] presented the design requirements of the high-side and low-side types of the STC in detail. Further, they showed that the high-side configuration has several advantages, such as minimal suction gas heating and discharge pressure pulses, a simple axial and radial compliance mechanism, and a simple flow path for the lubricant. However, the drawback of this configuration is that the motor overheats easily under a high compression ratio and the STC has a low operating efficiency because of operation at a high discharge temperature and high oil circulation, which are not mentioned in the paper presented by Richardson and Gatecliff.

From an analysis of the launched commercial small STC products, we found that almost all the STCs that achieved high efficiency were developed with a high-side configuration. However, we believe the low-side STC could achieve high efficiency as high-side STCs are. For improving the low-side pressure type STC's efficiency, the leakage problem needed to be solve first. Therefore, we adopted the STC developed by Chang et al. [7], which uses a low-side STC configuration, to be an original STC model.

1.6 Structure of dissertation

The contents of this dissertation are described below:

Chapter 1 briefly introduced the operation of the STC, the ACM for scroll sealing, and variable speed STC. The motivation and objectives also discussed in this chapter.

Chapter 2 presented the investigation of the leakage mechanism and the effect by the numerical analysis. In this chapter, a mathematical model was constructed and integrated into the developed STC package. The numerical simulation results of the leakage effect for different STC operation speeds also described in this chapter, which discussed in terms of energy conservation and performance improvement. These results will be verified by conducting experiments with one test platform constructed for an R22 LPS STC prototype with/without ACM mechanism in Chapter 4.

In chapter 3, the complete structure design of the ACM was presented. First, several important literatures were reviewed, and mathematical models depicting the geometry, thermodynamics, and dynamics of the mechanism, which are built on the basis of these literatures, were described. Case studies on designing the ACM module of STC products were introduced in section 3.3~3.5, which also presents numerical simulations and experimental studies. The results presented in chapter 4 show energy conservation and an improvement in the performance of the R22 LPS STC prototype at the extended operating speeds.

In order to understand how the thermo-physical characteristics of the refrigerant influence the ACM design, a study on the thermo-physical characteristics of the refrigerant comparison is discussed in Chapter 5 before presenting case studies of the R410A and R744 (CO_2) LPS STCs with ACM for air conditioning and refrigeration application. The scroll clearance for R744 LPS STC ACM design in our research is different from that in the studies presented in chapter 4. However, the pressure difference is the main issue in refrigeration application.

Finally, the important conclusions are summarized and future works are discussed in Chapter 6.

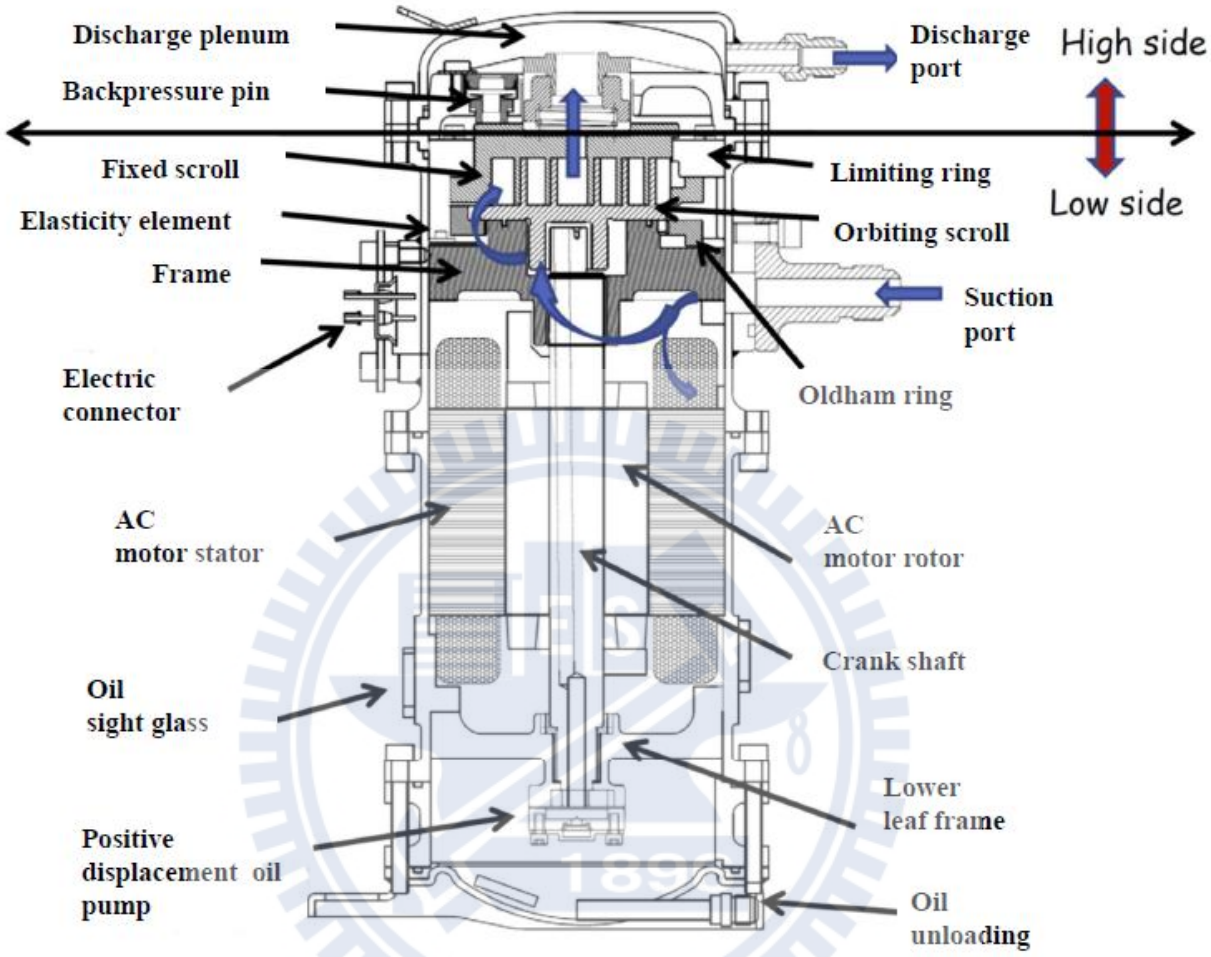

Fig. 1.1 Low(-pressure)-side scroll-type compressor (LPS STC)

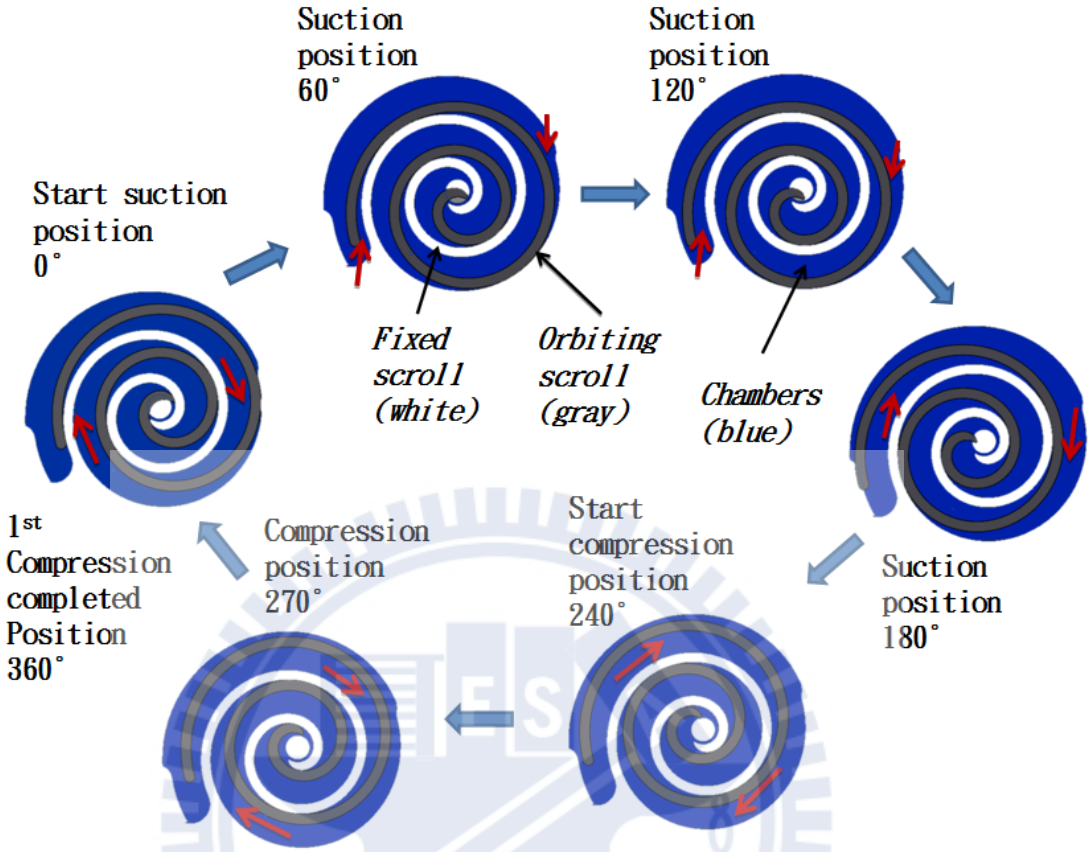

Fig. 1.2 Complete cycle of STC compression process

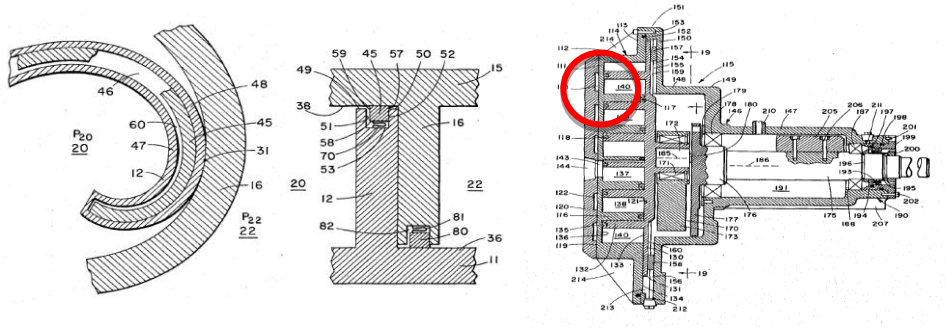

Fig. 1.3 Tip sealing means: Arthur D. Little, Inc., US 3,994,636, Nov. 30, 1976

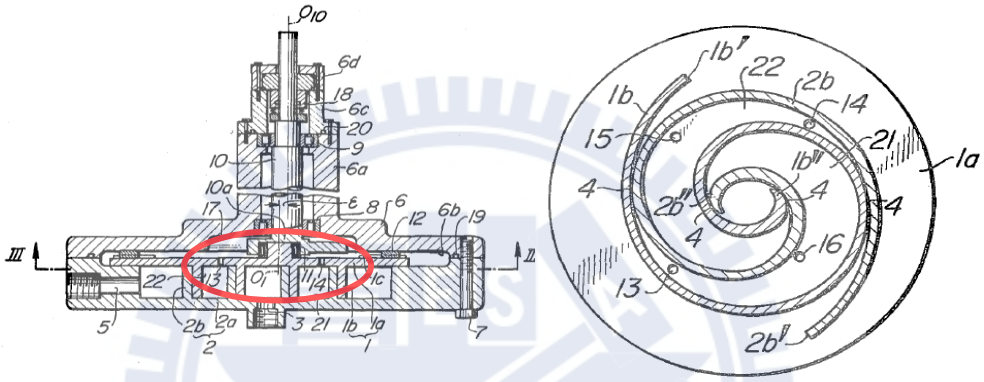

Fig. 1.4 Pressurized gas to back of orbiting scroll: Hitachi, US 4,475,874, Oct. 9, 1984

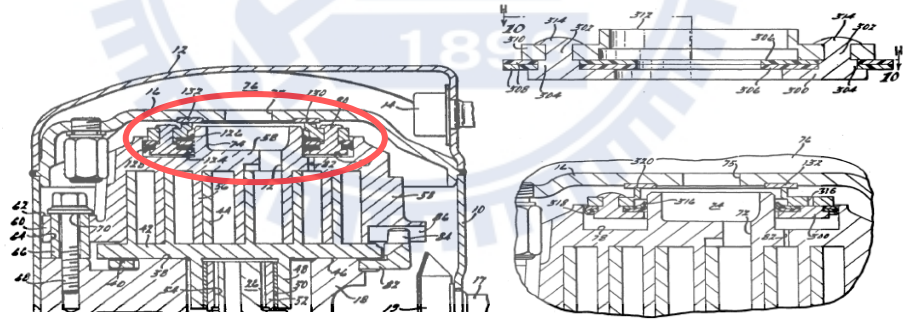

Fig. 1.5 Pressurized gas to back of fixed scroll: Copeland, US 5,156,539, Oct. 20, 1992

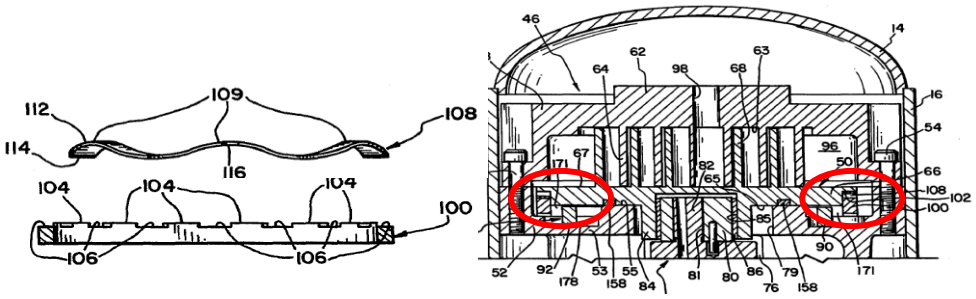

Fig. 1.6 Pressing member: Tecumseh Co., US 5,383,772, Jan. 24, 1995

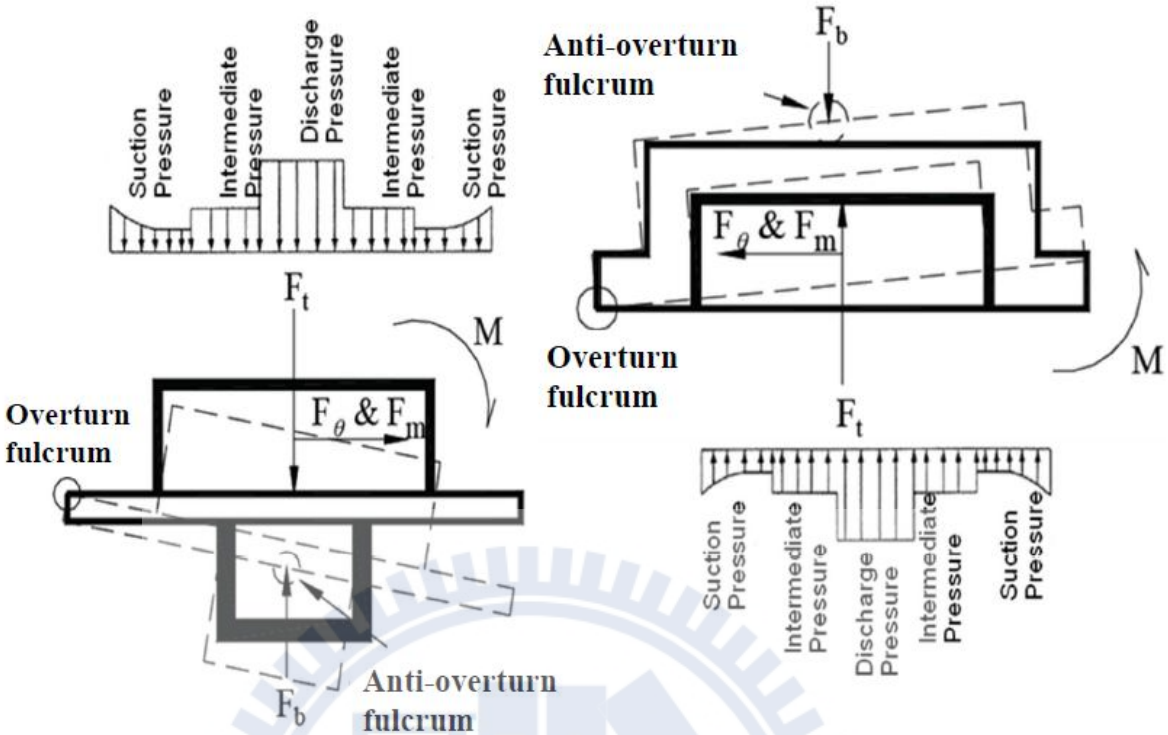

Fig. 1.7 Fluid pressure as backpressure on scroll member

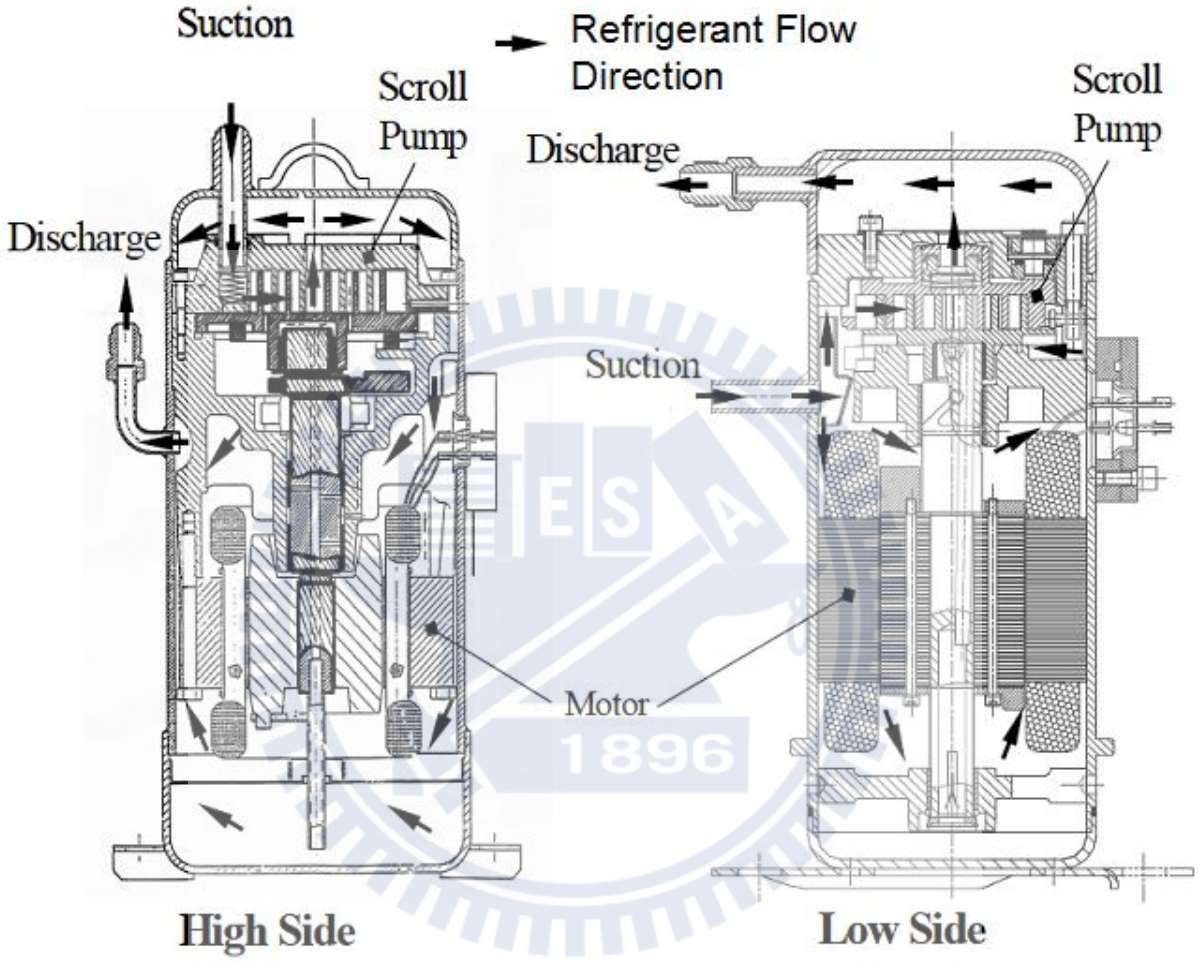

Fig. 1.8 High-side and-low side shell configurations of STC

CHAPTER 2 STUDY ON LEAKAGE EFFECT IN LOW-PRESSURE-SIDE STC

2.1 Literature review

The STC is an important component of modern air conditioners because of its high efficiency, low noise, simple mechanism, and high reliability. Further, in recent years, studies on STCs have primarily focused on enhancing their performance by employing new technologies. For example, one such technology—the variable-speed control (or inverter-fed drive)—can improve efficiency and reduce energy consumption [8~10]. However, the construction of a variable-speed STC prototype is very expensive and impractical. Therefore, many researchers have employed numerical methods for investigating the performance of STCs.

Most of these numerical methods can be classified into two categories: "dynamic analysis of compliances" and "thermodynamic analysis of scroll operations." The design theories of STCs and their geometric aspects have been reported previously [11] [12]. Further, investigations on the variations in the compressor performance when a self-adjusting backpressure mechanism is employed for axial compliance have been conducted [13]. A suction process using a dynamic model also has been analyzed [14]. The losses resulting from friction, compression, and leakage have also been studied via numerical analyses and experiments [15].

Most of these studies indicated that the friction losses were due to the contact behavior whereas the leakage losses were a result of the type of sealing between the orbiting and fixed scrolls. This is because the internal leakages not only decrease the cooling capacity but also influence the balance of inner forces, particularly at extended (both higher and lower) operating speeds. Therefore, it is extremely important to resolve the leakage problem for ensuring high reliability and energy conservation.

The abovementioned studies have also suggested that the best method for reducing internal leakage is to control the balance of internal forces of the compressor by using a compliance mechanism, which helps to maintain an optimal clearance between the scroll wraps. However, in the previous studies, the authors have suggested that the compliance mechanism is quite different in high-pressure shell (HPS) STC and low-pressure shell (LPS) STC. Both these STC types have significantly different methods for controlling the optimum scroll clearance because of the

differences in the characteristics of the pressure difference [16~18].

The previous literatures have also reported investigations on the leakage characteristics in STCs, such as leakage mass flow rate, leakage model, experimental investigations, and computational fluid simulations. However, few studies have been conducted on robust ACM designs for achieving energy conservation in an LPS STC operating at extended operating speeds.

In this study, a simple leakage model is constructed by transforming the involute leakage path into a half-circular path and is integrated into a previously developed STC-performance simulation package (ITRI_STC) [19]. Further, use this package with the parameters of a R22 STC model to simulate the inner leakage of the LPS STC via varying the clearance of scrolls. These numerical studies show an optimum clearance value for maintaining good cooling performance and high volumetric efficiency. The research results will possibly help in designing an ACM for improving the performance of STCs.

2.2 Numerical simulations of inner leakage effect

Leakage flows have been analyzed previously using various models [20~25]. In these studies, both theoretical and experimental investigations have been conducted for the analysis of leakage parameters [20~22]. These researches demonstrated that radial leakage (also called tip leakage) is more critical than flank leakage because the path of radial leakage is considerably longer than that of flank leakage (Figs. 2.1 and 2.2). In this study, the radial leakage problems are investigated. The results contribute to the enhancement of the effectiveness of the ACM design at extended operating speeds.

2.3 Mathematical model of radial leakage

Usually, most of the commercially available sealing part designs (such as floating tip seals [25]) are applied to reduce radial leakages and to prevent friction losses in the STCs. However, the use of seals in STCs increases manufacturing costs and requires precise assembly. Furthermore,

low operating speed and low pressure differences cause the floating tip seal to fail. Therefore, compressor designs without floating tip seals, which have low radial leakage, are being used by manufacturers such as Copeland, Hitachi, and Matsushita. In such designs, the radial leakage path can be considered as a circular path (Fig. 2.3).

The radial leakage is calculated by introducing a leakage flow on a one-dimensional flat plate [26] (Fig. 2.4). The direct leakage path is the scroll wrap thickness (can be considered as a constant value). Although the direction of the leakage path along the scroll curve changes with the orbiting angle, the typical path can be projected as several concentric circles, and the simplified leakage path is similar to the ring-type leakage path (Fig. 2.5).

We employed the following assumptions in this leakage model in order to simplify the numerical analysis:

(a) The leakage along the y direction is extremely small, as shown in Fig. 2.4, and can be considered to be related only to the pressure, temperature, and mean fluid density, along the x direction.

$$P = P(x); T = T(x); \rho_{mn} = \rho_{mn}(x) \tag{2-1}$$

(b) The fluid is a mixture of a refrigerant and oil and can be considered a Newtonian fluid.

$$\tau = \mu_{mn} \frac{\partial u}{\partial y} \tag{2-2}$$

(c) For small clearances, the flow direction can be considered one-dimensional; moreover, the velocity in the y direction is considered to be zero.

For the clearance, (δ) is very small; the fluid flow direction can be considered

one-dimensional, which implies that the flow velocity in the y direction can be considered to be zero. ($v = 0$).

$$\frac{\partial u}{\partial x} + \frac{\partial v}{\partial y} = 0 \tag{2-3}$$

From assumptions (a) and (c), we can express the continuity equation as follows:

$$\frac{\partial u}{\partial x} = 0 \tag{2-4}$$

Thus, the flow velocity is a function of the y direction:

$$u = u(y)$$

The momentum equation of the leakage flow is as follows:

$$-\frac{\partial p}{\partial x} + \mu_{mn}\left(\frac{\partial^2 u}{\partial y^2}\right) = \rho_{mn}\left(u\frac{\partial u}{\partial x} + v\frac{\partial u}{\partial y}\right) \tag{2-5}$$

From equations (2-1)–(2-5), we find that

$$\frac{\partial^2 u}{\partial y^2} = \frac{1}{\mu_{mn}}\frac{dp}{dx} \tag{2-5a}$$

The variables p, dp/dx, and μ_{mn} are independent of y. Equation (2-5a) can be integrated with respect to y with the following boundary conditions:

$$u(y = 0) = 0 \tag{2-6}$$

$$u(y=\delta)=0$$

If the boundary conditions are substituted into equation (2-5a), the velocity distribution of the leakage depends only on the clearance, as follows:

$$u=-\frac{y}{2\mu_{mn}}(\delta-y)\frac{dp}{dx} \tag{2-7}$$

Hence, the leakage mass flow rate $(\frac{dM}{dt})$ is

$$\frac{dM}{dt}=L\int_0^{\delta}\rho u dy=-\frac{1}{2}L\rho_{mn}(\frac{\delta^3}{6\mu_{mn}}\frac{dp}{dx}) \tag{2-8}$$

The distribution of the pressure in the leakage channel is considered linear as follows:

$$\frac{dp}{dx}=\frac{p_o-p_i}{l}$$

The mass flow rate of the radial leakage can be calculated by

$$\frac{dM}{dt}=L\rho_{mn}(\frac{\delta^3(p_i-p_o)}{12\mu_{mn}l}) \tag{2-9}$$

This equation has several explanations:

(1) $\frac{dM}{dt}\propto L$; this shows that shorter the sealed length, the greater is the volumetric efficiency.

(2) The leakage mass is proportional to the scroll gap (δ).

(3) The leakage direction is identical to that of the pressure difference, and the mass leakage increases with the pressure difference.

(4) Leakage decreases with an increase in the coefficient of dynamic viscosity (μ_{mn}).

(5) As the direction of leakage is orthogonal to the scroll velocity which is tangential to the base circle of the scroll profile, the leakage may not always increase (or decrease) by the component of the direction with the component of the same direction of the scroll velocity. However, the leakage decreases with an increase of the compressor speed is because the leakage time has become shorter.

By introducing the ring leakage model of the rolling piston pump [26], we find that the leakage model is based on several half-ring leakage paths that are equivalent to the original involute leakage path (Fig. 2.4). The scroll wrap thickness (l) is equivalent to the mean radius (r_m)± half the wrap thickness ($\frac{l}{2}$), whereas the mean radius is $\frac{L}{2\pi}$ (Fig. 2.4).

Finally, the radial leakage model is expressed as follows:

$$\frac{dM}{dt} = \frac{\pi\delta^3(p_i - p_o)}{6\upsilon \ln(\frac{r_o}{r_i})} \qquad (2\text{-}10)$$

In equation (2-10), υ is an average value because it depends on the oil-mass percentage of the leakage fluid [26]. The overall leakage model assumed keeping in a thermal steady-state because of the compression chambers has been considered as a heat insulation system. The thermal dynamics calculation module is separator from the leakage module as the calculate flow chart shown in fig. 2.6. The leakage calculation module uses the thermal and pressure data from thermal dynamics calculation module, and it feedback the mass flow rate and leakage data to STC-package to calculate performance.

2.4 Case study on theoretical performance simulations

In order to investigate the effects of radial leakages on the LPS STC, we performed

simulations of certain case studies using ITRI_STC [19] combined with the refrigerant data base named REFPROP 8 [27]. Fig. 2.6 presents the algorithm for calculating leakage.

The following three definitions of efficiency are employed for evaluating the STC performance, and their formulas follow those in Chang's PhD thesis [28]:

(a) Coefficient of performance (COP)—the energy proportional to the cooling capacity and the power consumption of the compressor;

(b) Volumetric efficiency of leakage gas mass loss—the percentage of the ratio of actual mass flow rate (i.e., discharge mass flow rate with leakage) to the theoretical discharge mass flow rate;

(c) Isentropic compression efficiency—the ratios of the ideal isentropic compression work to the actual compression work (i.e., motor electric power consumption).

The main geometric parameters of the scroll in the LPS STC in this study are listed in Table 2-1, and the compressor's operating conditions are listed in Table 2-2. In order to eliminate the influence of flank leakage, the flank clearance was set to zero during the numerical calculations. Figs. 2.7–2.10 show the results of the simulation; here, the scroll clearance (δ) was varied from 0 to 21 μm, whereas the operating frequency of the compressor was varied from 40 to 80 Hz.

Clearly, the findings indicate that the COP is inversely proportional to the leakage clearance (Fig. 2.7). Fig. 2.8 shows that the volumetric efficiency of the refrigerant mass loss decreased with an increase in the clearance value. Fig. 2.9 and Fig. 2.10 show the refrigerant flow rate and cooling capacity, respectively. From a comparison of these results, we find that the radial clearance should be limited to within 6 μm in order to maintain a high performance of the STC. These results also help in achieving better ACM designs and performances.

2.5 Remarks

The value of 6 μm for axial clearance was obtained for the given geometry and operating condition. The manner in which it can be affected by variation in geometrical and operating parameters is the most important aspect in this research for designing the ACM.

Discussions:

Changing both the geometrical and operating parameters may affect the optimum clearance value.

However, we find that if the geometry is changed, the axial leakage path and the scroll thickness may affect the optimum clearance value. We believe that there should be some relationship between the scroll thickness and the axial clearance. However, in this study, we assume that the axial clearance should be considerably lower than the scroll thickness (b), i.e., $\delta/b << 1$.

If the geometry is not changed, the changes in the operating parameters can affect the pressure difference. The optimum axial clearance can be maintained by our ACM design because the backpressure pin design considers that the pressure difference originates from the different operating conditions.

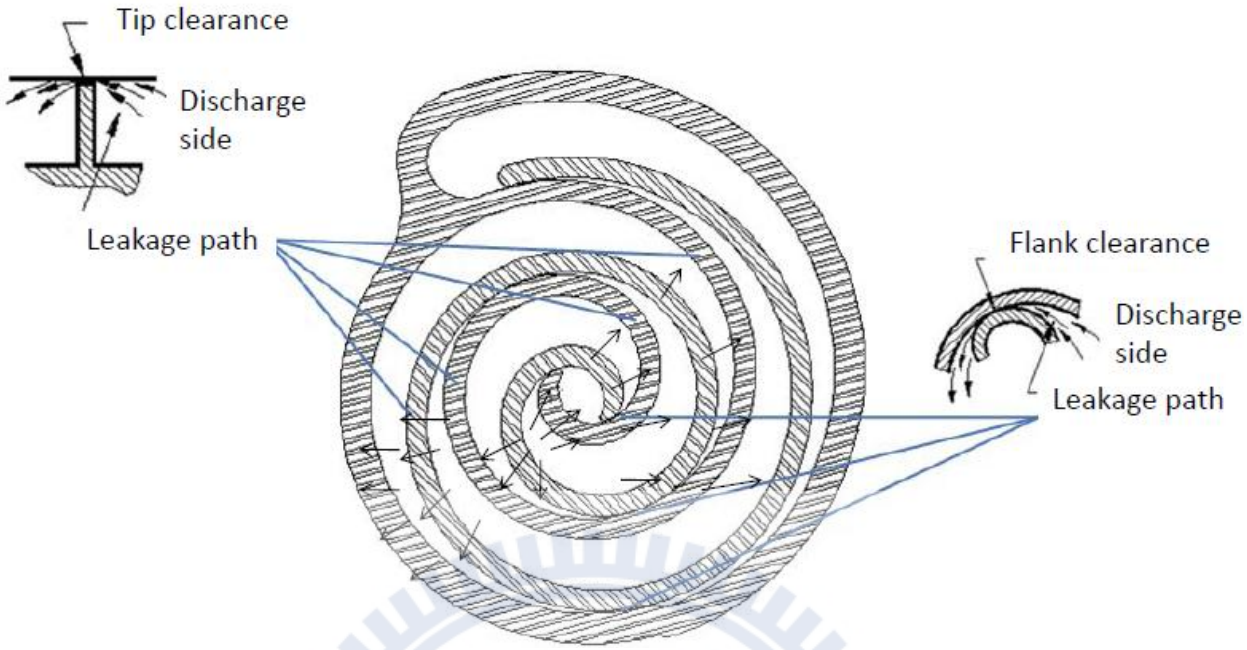

Fig. 2.1 Inner leakage type

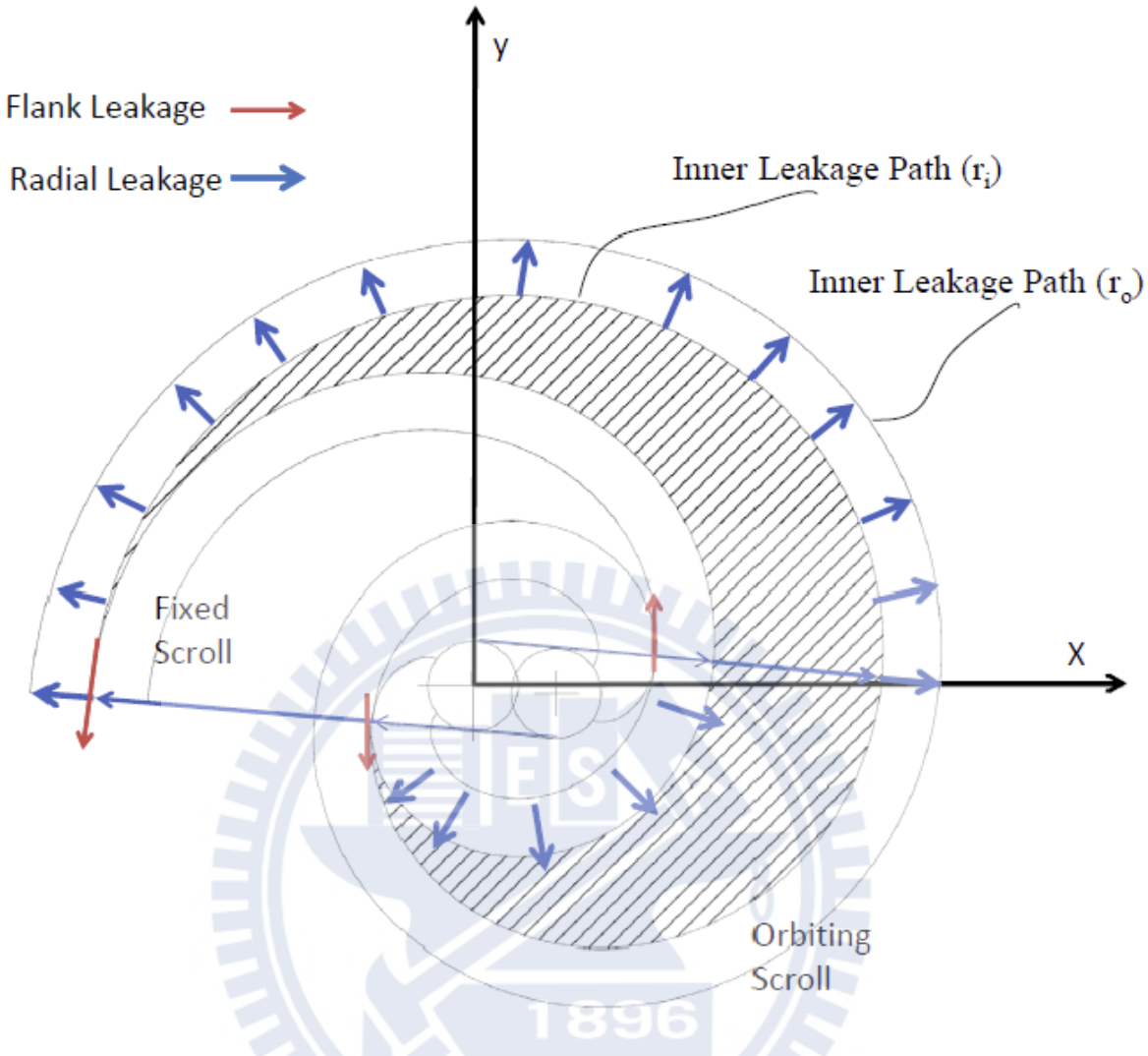

Fig. 2.2 Involute leakage path

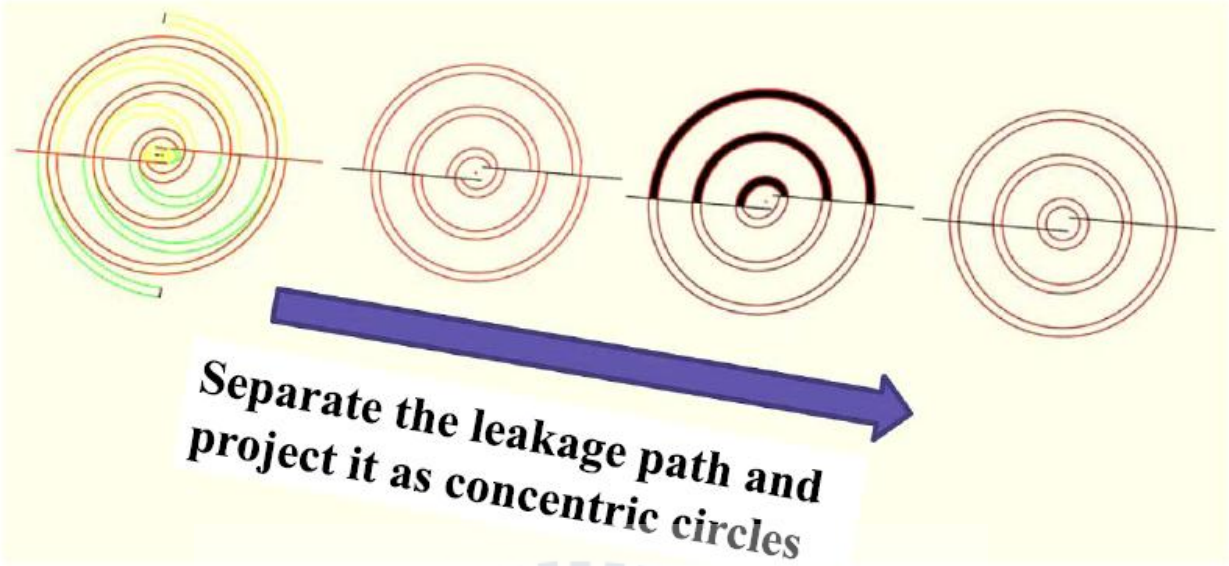

Fig. 2.3 Integrated and simplified leakage path model (as circular path)

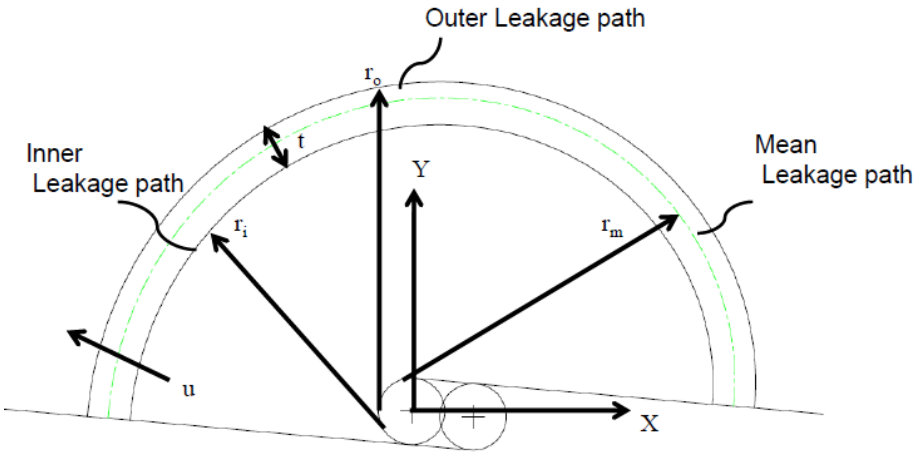

(a) Involute leakage path scheme for leakage analysis

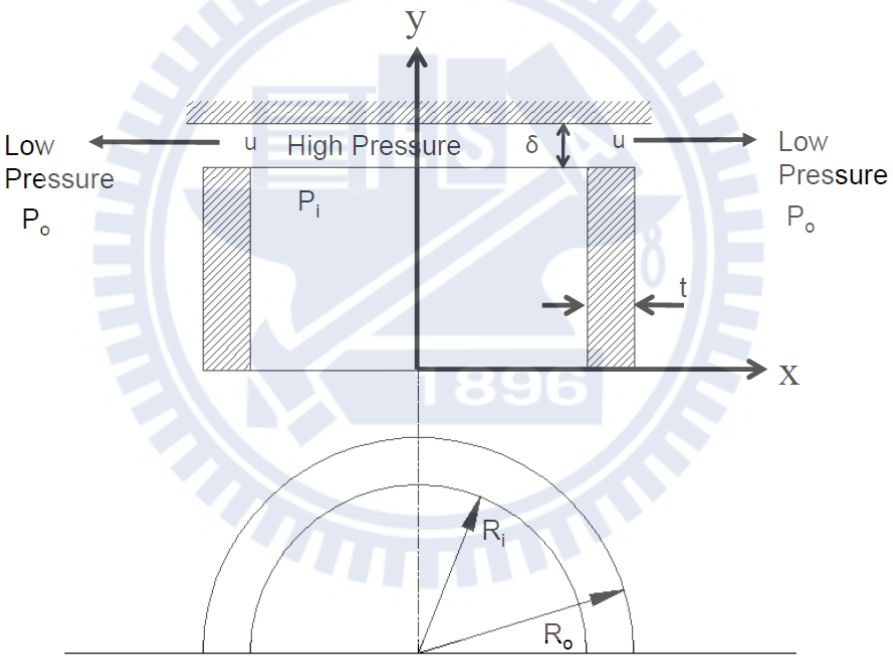

(b) Simplified half-circle leakage path for leakage analysis

Fig. 2.4 Leakage flow simulation model

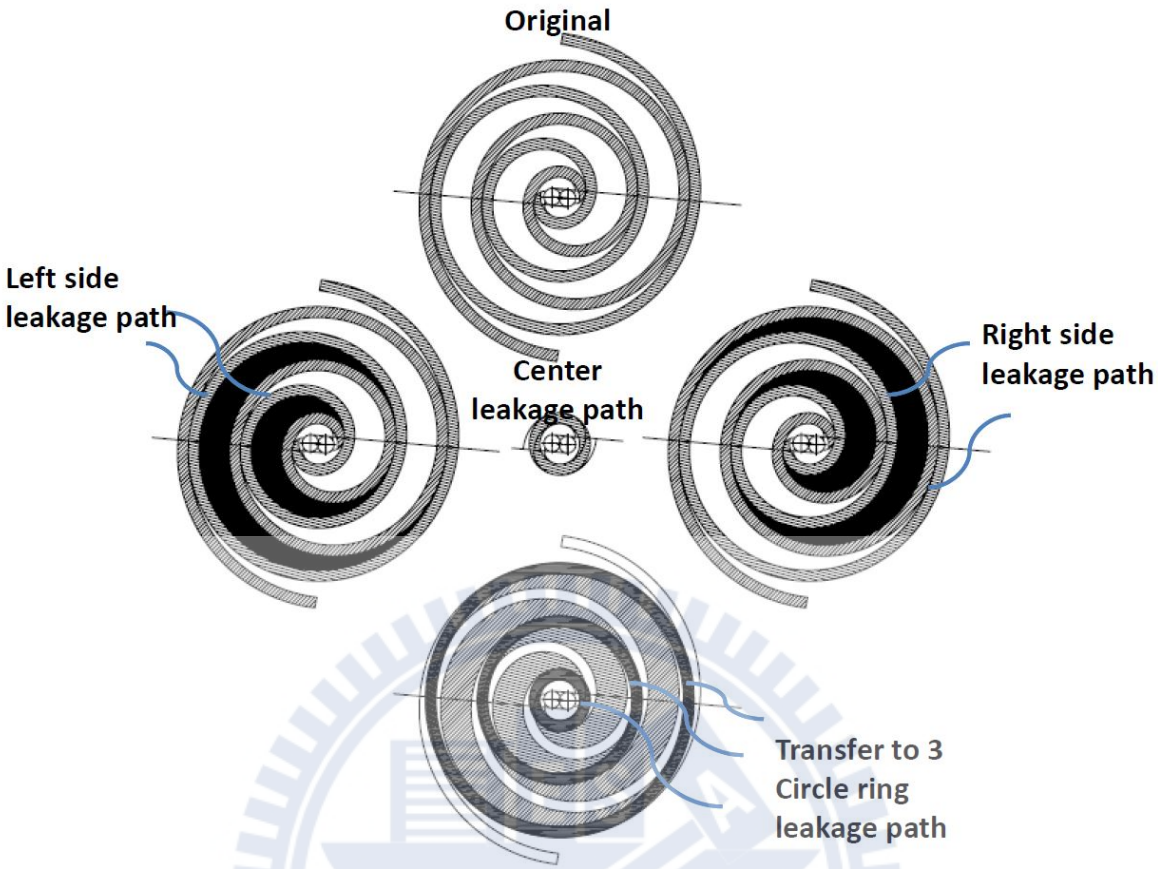

Fig. 2.5 Concentric circles as leakage path

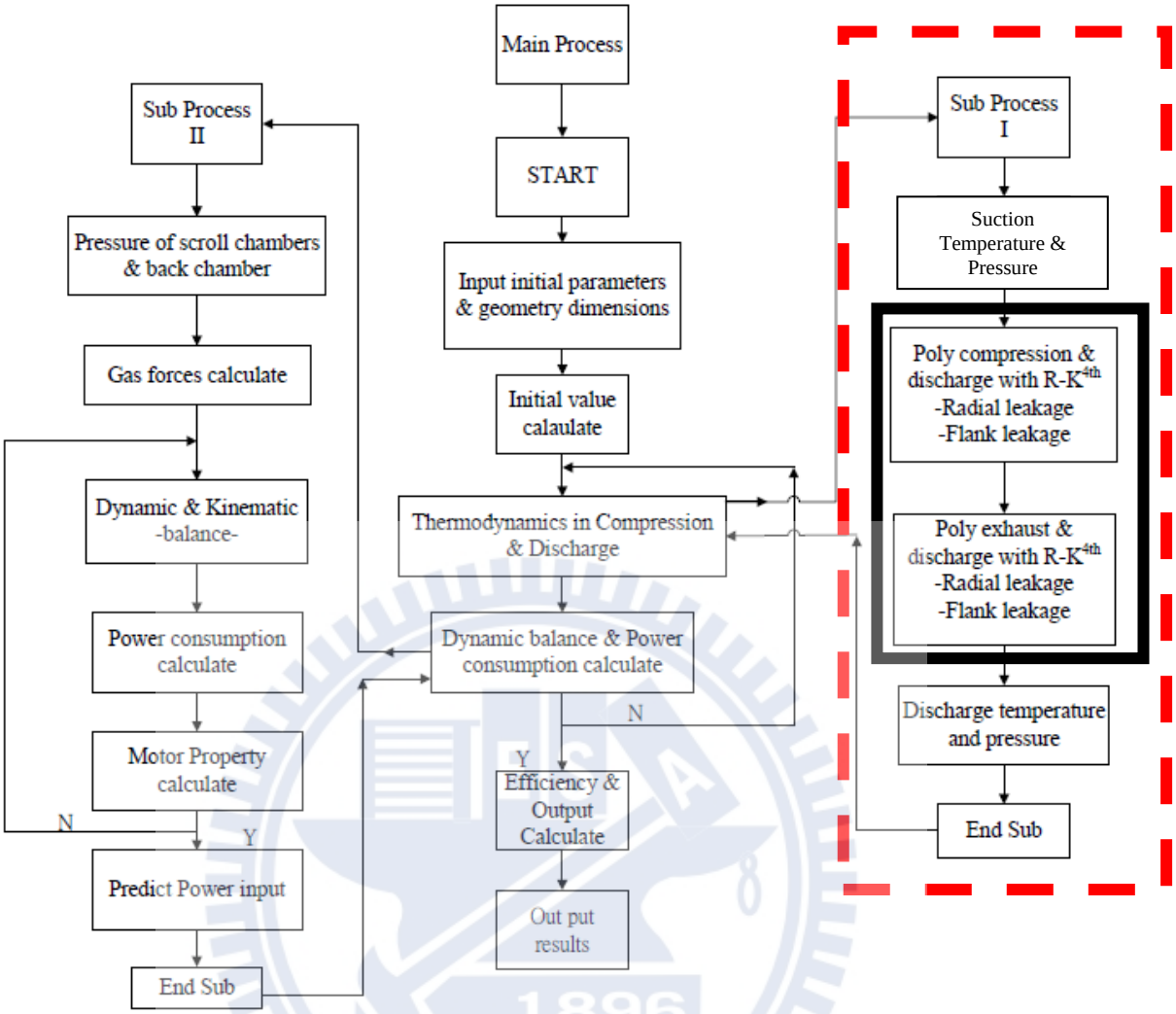

Fig. 2.6 Algorithm for calculating leakage

Table 2-1 STC parameters and experimental operating conditions

Parameters of the LPS STC	
Parameters	Value
Radius of the basic circle of the scroll(a)(mm)	2.062
Thickness of the scroll(t)(mm)	2.65
Involutes angle of the scroll(φi)(degree)	1150
scroll pitch(Tp)(mm)	12.956
scroll wrap height(hs)(mm)	25.2

Experiment operating conditions		
Environment conditions		Value
Condensing Temperature(℃)		54.4
Evaporator Temperature(℃)		7.2
Superheat(K)		10
Subcool(K)		8.3
Expansion valve Temperature(℃)		46.1
Refrigerant		R22
STC operation speed		
Condition	frequency setting(Hz)	actual revolution(rpm)
A	40	2261
B	50	2871
C	60	3454
D	70	4033
E	80	4612

Table 2-2 Compressor prototype and STC performance measurement specifications

Compressor Prototype Specification		
Compressor Characteristics		
Theoretical swept volume @ 60 Hz	7.5762 m3 /h	
Nominal speed	3450 rpm	
Maximum operating current	19.2 A	
Usual operating range		
Supply temperature :	18-25 ℃	
Exhaust temperature	80-120℃	
Supply pressure	0.3-0.7 MPa	
Refrigerant mass flow rate	87~290 kg/hr	
Electrical power	0.8-3.7 kW	
STC performance Measurement Specification		
Refrigerant	R22	
Range of cooling capacity	1.5kW~15kW	
Test standard- Capacity, COP and Volumetric Efficiency determination	ASHRAE 23 and ISO 917	
Parameter	Range	Stability
Discharge Pressure(MPa)	0.62~3.2	±0.01
Suction Pressure(MPa)	0.12~0.96	±0.015
Inlet Temperature(°C)	15 ~ 52	±0.1
Suction Temperature(°C)	-25 ~ 38	±0.1
Ambient Temperature(°C)	32	±2
Compressor Speed(rpm)	1200 ~ 7200	± 0.25%

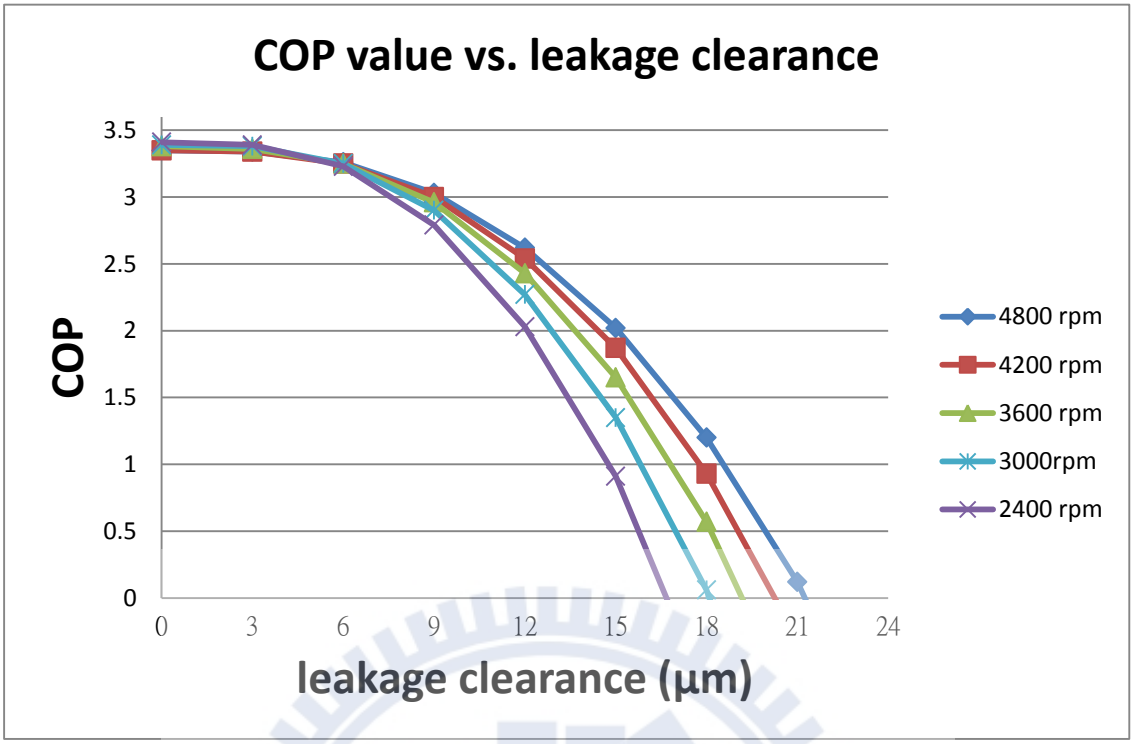

Fig. 2.7 Calculation results: COP value versus leakage clearance

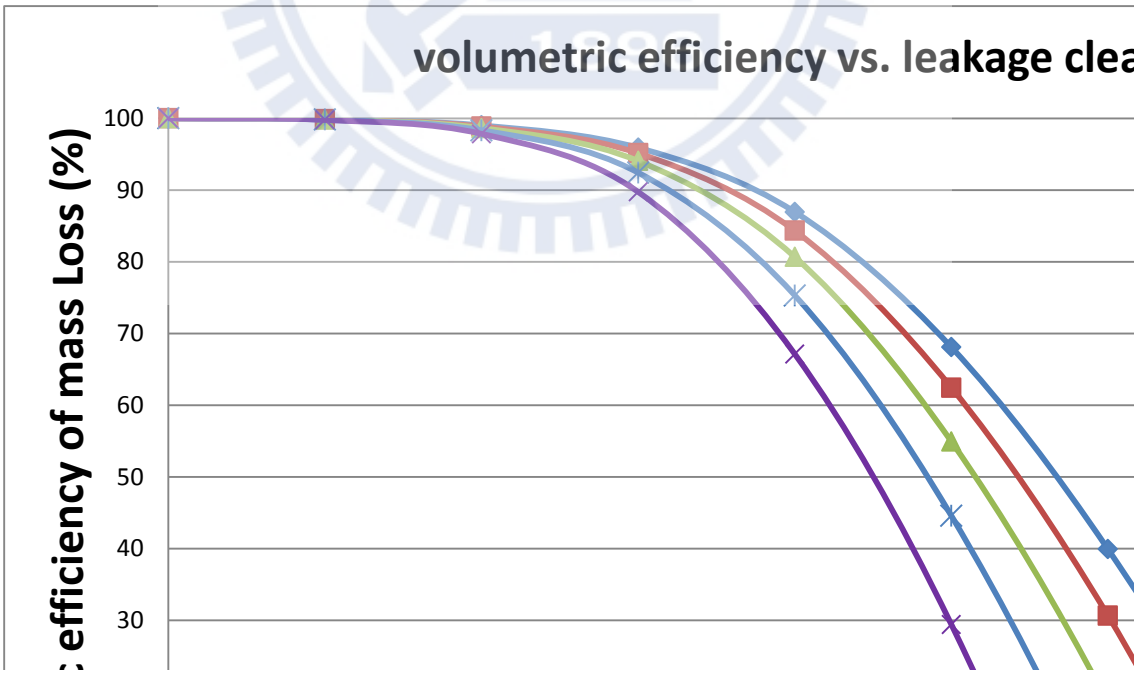

Fig. 2.8 Calculation results: Volumetric efficiency versus leakage clearance

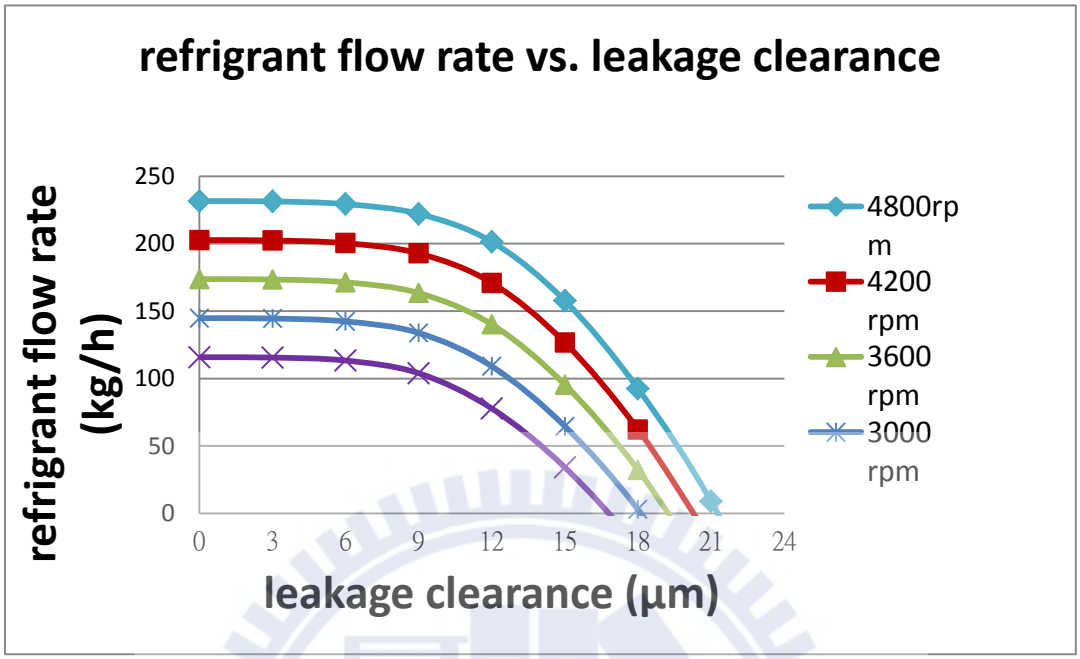

Fig. 2.9 Calculation result: Refrigerant flow rate versus leakage clearance

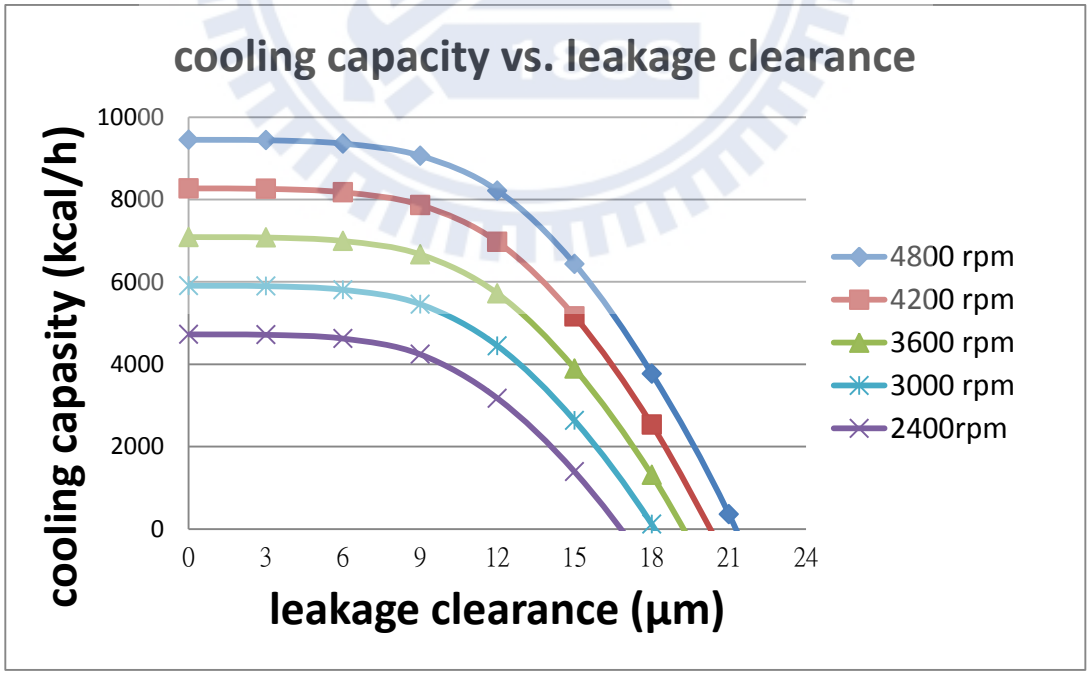

Fig. 2.10 Calculation results: Cooling capacity versus leakage clearance

CHAPTER 3 AXIAL-COMPLIANCE MECHANISM OF LPS STC

A cross-sectional diagram of the ACM designed for an LPS STC is shown in Fig. 3.1. A scroll pump sucks the suction gas from the low pressure side (Fig 1.1), compresses it, and then discharges it at high pressure to the plenum (high pressure side); the exhaust is then emitted out of the discharge port. During compression process, the orbiting scroll continues to move with a wobble because of the inner unbalanced forces and tilting moments; moreover, the reaction forces and moments cause the fixed scroll to wobble as well. Therefore, in this study, in order to prevent the occurrence of clearances owing to the wobble phenomenon, in this study, the fixed scroll was pressed by a backpressure mechanism to trace the orbiting scroll in the vertical direction and the orbiting scroll was enforced (by the compressed gas pressure) to keep the base plate close to the surface of the trust bearing. However, the tangential gas forces cause the fixed scroll to wobble (Fig. 3.2). In the following subsections, the backpressure mechanism and suspension ACM designs for limiting the scroll wobble and maintaining the axial clearance near the optimum value (within 6 μm) are described.

3.1 Backpressure mechanism design

From the patent analysis, the patent US 6,368,088 Bl [29] shows the backpressure regulation mechanism for the fixed speed STC under different working conditions. The mechanism is operated by pressure different. However, to consider the behavior of LPS STCs under variable-speed operations, the most important factor is the variation in the pressure difference between the high and low sides in the STC. Using the pressure difference to drive the ACM could be the same function of US 6,368,088B1. Nevertheless, the backpressure regulation

mechanism using the significant changes in backpressure during the variable-speed operation of the compressor leads to the following two shortcomings.

(1) When the compressor operates at low condensation temperatures or at low pressure differences, the backpressure decreases, leading to poor sealing between the two scrolls and, hence, leakage. Moreover, in the case of excess leakage, the compressor cannot build up the pressure difference.

(2) The previous scenario reverses when the compressor operates at high condensation temperatures or at high pressure differences. Excessive backpressure increases the contact at the two scrolls and causes friction loss on the interface between the base plate of the orbiting scroll and the thrust bearing. This friction loss drastically increases the power consumption of the compressor.

For overcome the two shortcomings, a self-adjusting, robust design of the backpressure mechanism by forces analysis is proposed (Fig. 3.3(a)). Curve A represents the net force that can push and separate the two scrolls (this force is called the scroll separation force, and only its maximum value is considered here). Curve B represents the sum of the backpressure force by boss and the three pressure-pin forces by three backpressure pins due to the discharge pressure. However, curve B can satisfy the backpressure only during the rating operations. When the STC is operating at the under un-rating conditions, the pressure difference either decreases or increases whereas the backpressure correspondingly decreases or increases, respectively. Further, at low backpressures, the leakage loss increases, whereas at high backpressures, the friction loss increases. Furthermore, from the force analysis, the pre-pressing force value (F_s) can be designed.

For providing an optimum backpressure, the backpressure force and the three pressure-pin forces should have a self-adjusting mechanism. (Fig. 3.4) Therefore, the optimum backpressure distribution curves should be curves C1 and C2, which provide a suitable and sufficient backpressure under any operating conditions. (Curve C1 represents the construction with the backpressure force, three pressure-pin forces, and disk spring forces. Curve C2 represents the construction only with the backpressure force and the three pressure-pin forces.) The designing points at P1 and P2 can be used to determine the point F1 and F2, respectively. Further, using the relationship between force and pressure, we can determine the backpressure areas via calculations.

The overall surface area of the boss and the pins can thus be determined which in turn determines the slope of Curve B. And the value of the area of the boss and the pins is also on the Curve C1 (called the point F1). From the same analysis, the overall surface area of the boss and the pins can thus be determined which in turn determines the slope of Curve C2, and the value of the area of the boss and the pins is also on the Curve C1(called the point F1). Fig.3.3(b) show the position design limited for the backpressure regulation pins. However, in this study, the position and location angles of the three pins are from the try-and-error method.

3.2 Suspension ACM design

In this study, an ACM design is developed to fine-tune the axial motion of the fixed scroll. In here, we take free body diagrams of each parts of the ACM (shown in fig. 3.4). The fig. 3.5 shows the exploded diagram of the suspension ACM. The design process of the two crescent leaf springs (as the elastic element) has been verified in detail by Tang et al. [30]. In their study, a design process was developed to determine the design parameters of the elastic element, and the

process was verified experimentally. Their results only demonstrate that the ACM can assist the compressor at low operating speeds from 50 Hz to 34 Hz under the rating conditions. Tables 3-1 and 3-2 list the results of the calculation of the inner forces for designing the backpressure and suspension ACMs, respectively. The tilting motion of the fixed scroll due to the tangential gas forces acted at the half-height of the scroll blend. As shown in Fig. 2.8, the limiting parts provided an anti-moment to overcome the tilting moment. Therefore, the contact noise and the leakage caused by tilting could be reduced.

3.3 Study on structural design and analysis of new leaf-spring-type ACM

Several factors can influence the efficiency of an STC, and one of them is the internal leakage problem. However, the traditional mechanism for preventing internal refrigerant leakage in the scroll pump is a sealing mechanism to dynamically seal the scroll clearance caused by the unbalanced inner forces and moments in the STC. We know that the leakage path has been determined and the scroll line length has been designed. Radial leakage is larger than flank leakage because of its longer path. In this study, we discuss a sealing mechanism called a leaf-spring-type ACM, and this mechanism could improve the volumetric efficiency and increase the cooling capacity.

The compliance mechanism is used for controlling the floating tolerance of the fixed scroll between the frame and a separate plate and for keeping the radial leakage to minimum. Further, the compliance mechanism is used for solving the incongruity in the backpressure of the fixed scroll in the axial direction, which can increase the forces exerted from the fixed scroll to the orbiting scroll. This backpressure causes more friction loss, which can induce a decrease in the

compressor efficiency. For eliminating the unnecessary losses, we consider case studies on designing an ACM with a leaf-spring structure to limit the floating distance of the fixed scroll and to keep the tip clearance in the optimum state. From finite element analysis and the experimental tests on the prototype, we find that this new sealing-function module can reduce noise and increase the cooling performance.

3.3.1 Literature review

In recent years, power conservation has become a critical aspect in the air conditioner and refrigerator industries. In order to conserve the electric power, improvement in the performance of a compressor has been proposed, which has led to considerable research on the behavior of leakage in a scroll pump (The internal leakage of a scroll pump can decrease the cooling capacity and increase the power consumption.) under the operating conditions (see Fig. 3.6). Tojo et al. [31] have proposed a self-adjusting backpressure mechanism for a HPS STC, wherein the fixed scroll is fastened to a frame and the orbiting scroll floats under the gas pressure between the fixed scroll and the frame. Suefuji et al. [32] have presented a method for calculating the performance of a hermetic STC by using a simplified thermal analysis model. Bush et al. [33] have discussed the stability characteristics of the backpressure-supporting orbiting scroll. Marchese et al. [34] have discussed the dynamics of an orbiting scroll with axial compliance.

Lee et al. [35] have proposed an optimum ACM for the LPS, which can increase efficiency by 15% under a fixed operating frequency. Park et al. [36] have discussed the results of the thermodynamic analysis of the performance of a variable-speed STC with refrigerant injection; however, the ACM has not been discussed. In any case, research and information on developing an ACM for the tip leakage of scrolls in a LPS STC are insufficient, particularly under a low operating frequency. This study presents a suspension-compliance mechanism in a LPS STC (see

Fig. 3.7).

This mechanism, using two leaf springs, can prevent scroll tip leakage and help to reduce the scroll contact noise. Normally, the fixed and orbiting scrolls in an LPS STC are subjected to unbalanced forces and moments that can cause the scroll plate to tilt, which causes leakage, noise, and additional frictional wear. With a suitable design such as the one proposed here, the compliance mechanism can eliminate the unbalanced forces on the scrolls, and prevent the additional frictional forces between the scroll tips during the operation of the STC. Several numerical methods have been adopted in this study. For example, a finite element model (FEM) code (ANSYS) has been used to predict the deformation in the compliance, and a compressor-performance simulation package developed by ITRI has been used to calculate the gas forces for the FEM boundary conditions. Further, the clearance between the two scroll tips has been optimized to design a leaf spring of suitable thickness (Fig. 3.8).

3.3.2 Basic analysis of inner force for the ACM design

To simplify the analysis of the proposed mechanism, the following basic assumptions are made:

1. The fixed scroll has a limited floating displacement in the axial direction.
2. Only four dynamic forces directly acting on the fixed scroll are calculated precisely.

The contact force between the orbiting scroll and the fixed scroll resulting from a tilting moment on the orbiting scroll is assigned a constant value determined on the basis of previous studies. In this study, the four dynamic force categories are axial gas pressure forces, leaf spring forces, pressure pin forces, and backpressure forces (see Fig. 3.9). During operation, the axial

clearance between the fixed scroll and the orbiting scroll is determined by the equilibrium of forces. The resultant force pushes the fixed scroll, eventually leading to contact between the fixed scroll and the orbiting scroll. This causes a frictional force, noise, and unnecessary mechanical contact vibration. These four force categories are defined as following.

I. Backpressure Force

The backpressure force is generated by the discharge gas pressure acting on the check valve, and it can be calculated from the following equation.

$$F_b = P_d \times A \tag{3.3.2-1}$$

Here, F_b is the back force of the gas acting on the check valve; P_d, the discharge gas pressure from the backpressure chamber; and A, the cross-sectional area of the check valve.

II. Pressure Pin Force

The pressure pin force is caused by the pressure difference between the suction gas and the discharge gas in the high backpressure chamber acting on the pressure pin surface and by the downward force of the fixed disk spring. It is calculated from the following equation:

$$F_{pin} = (F_{disk} + F_{pd}) \times 3 \tag{3.3.2-2}$$

where F_{disk} is the disk spring force and F_{pd} is the net forces resulting from the pressure difference between the suction gas and the discharge gas in the high backpressure chamber acting on the pressure pin surface. Three pins considered in this analysis.

III. Axial Gas Force

The axial gas force is caused by the pressure distribution in the compression chambers between the fixed and orbiting scrolls. The axial force acting on the fixed scroll is calculated from the following equation:

$$F_g = P_d \times A_d + P_m \times A_m + P_s \times A_s \qquad (3.3.2\text{-}3)$$

where F_g is the axial gas force; P_d, the discharge pressure; P_m, medium pressure; P_s, the suction gas pressure; A_d, the area of the discharge chamber, A_m, the area of the middle chamber; and A_s, the area of the suction chamber.

IV. Leaf Spring Forces

The total force caused by the displacement of the leaf spring is computed by the following equation:

$$F_s = N \times K \times X \qquad (3.3.2\text{-}4)$$

where N is the number of leaf springs; X, the displacement of the leaf spring; and K, the spring stiffness.

During the operation of the scroll, a tilting moment is exerted on the orbiting scroll, which can result in the application of a contact force to the fixed scroll (see Fig. 3.10). The contact force is a major cause of the decrease in the compression efficiency and an increase in the noise level. The resultant four dynamic forces need to be designed suitably for achieving stable motion. This can be achieved by satisfying the following conditions.

$$F_b \geq (F_g + F_{tx}) \tag{3.3.2-5}$$

Here, F_{tx} is the contact force. It is difficult to precisely calculate the value of F_{tx}. In general compressor design, a random value is initially assigned to Ftx on the basis of previous studies.

3.3.3 CAE simulation model for improving ACM design

In order to design a leaf spring of appropriate thickness used in the prototypes, a finite element simulation package (ANSYS) [37] is employed to calculate the axial displacement of the leaf spring. The active forces calculated from the compressor-performance simulation software (developed by ITRI) are introduced as the boundary conditions. In the FEM model, the leaf spring is made of SKD11 steel; the scrolls, FC300 cast iron; and the fixed ring for the fixed scroll, AISI 1040 steel. Further, all the screws are made of SCM435 steel. The FEM is shown in Fig. 3.8, and the results of the simulation are shown in Fig. 3.11. According to the results of the FEM analysis, four leaf-spring prototypes are fabricated by two different thicknesses (0.8 mm and 1.0 mm) and two shapes for further experimental analysis.

3.3.4 Prototype experimental results

For comparing the results of the FEA simulations and the universal testing machine tests, a preliminary experiment is conducted by controlling the clearance and measuring the reaction forces acting on the prototype that uses a scroll-pump assembly as shown in Fig. 3.13. Another experiment is conducted in a compressor-performance testing room (in ITRI), and the operating conditions are as listed in Table 3-3. All the tested prototypes are operated at the rating speed (3600 rpm).

In this study, four types of leaf springs are included in the prototype assembly. The results of the deformation test are listed in Table 3-4. Table 3-5 lists the results of the STC prototype performance test. The EER value has not improved considerably for the present shape of the spring in the prototype. This may be because of the resistance of the refrigerant in the STC. A new shape of the spring is then designed, as shown in Fig. 3.14. Table 3-6 lists the results of the STC prototype-performance test. It can be seen that the EER value still has not improved considerably with this new spring shape, but the noise value has improved slightly.

3.3.5 Discussion on development of leaf-spring ACM

(1) The dynamic backpressure in the back chamber can be increased (or decrease) under certain operating conditions. This causes an increase (or decrease) in the forces acting on the back plate of the fixed scroll. In this situation, the back clearance controlling method (leaf-spring ACM) would be more suitable for forces balancing.

(2) The axial motion of the fixed scroll stabilizes because of the constraint imposed by the leaf-springs fastened on the fixed scroll and main frame; therefore, back clearance can be controlled by the leaf spring's rigidity (Fig 3.7).

(3) The fixed scroll can be tilted during normal operation (as shown in Fig. 3.10); this tilting motion can cause the deterioration of the compressor efficiency in an STC. The tracing action from the fixed scroll to the orbiting scroll can decrease the contact effect caused by the tilting motion. in order to get more understanding of this phenomenon, further experimental analyses are required.

(4) More studies with extremely low operating speeds of the compressor should be conducted to obtain information that is more useful for enhancing this ACM, which is also suitable for a variable-speed STC.

(5) For reliability, the crack of the feet on the four guide pillars of the frame should be improved.

3.3.6 Remarks on development of leaf-spring ACM

In this design case study, a suspension compliance mechanism with a leaf spring fixed directly on the frame is proposed for an LPS STC and the compressor performance for the prototype is measured. The following conclusions are drawn.

(1) Back clearance can influence the leakage of scroll tips. On maintaining a back clearance value between 0.04 and 0.09 mm, which was assumed in this study, we can increase the volumetric efficiency up to 93%.
(2) The leaf spring's rigidity depends on its thickness. In this study, the operating spring forces of an STC using an ACM with a 0.8-mm-thick spring decreased to almost half that of an STC using an ACM with a 1.0-mm–thick spring.
(3) From the mechanism prototype experiment, we find that the suspension-compliance mechanism functions well when the STC is under the standard compressor testing condition, and the STC's noise value is low.

3.4 Study of novel compliant suspension mechanism in LPS STC

In this section, we present a novel compliance mechanism that combines a fixed ring with two leaf springs as suspension in the fixed scroll in an LPS STC. The prototype has been developed by considering the dynamic balance of forces acting on the fixed scroll. Further, we

analyze the design with a leaf-spring thickness that constrains the floating behavior in the axial direction of the fixed scroll and is helpful in maintaining the balance of the dynamic inner axial forces. The experimental results of the prototype show that this novel design can provide the required balance and can ensure high volumetric efficiency, low noise, and low power consumption during compression.

3.4.1 Background

In recent years, power conservation has become a critical factor in designing compressors, particularly in the air conditioner and refrigerator industries. For achieving the advantage of power saving, variable frequency control in a compressor has spurred a great deal of research on the behavior of a scroll pump's leakage (the leakage can decrease the cooling capacity) under various operating conditions. The study presented here is of a novel suspension-compliance mechanism in an LPS STC (see Fig. 3.15). This mechanism, which involves the combination of a fixed ring and two leaf springs, can prevent the scroll tip leakage under a low operating frequency.

Normally, the fixed and orbiting scrolls in an LPS STC are subjected to unbalanced forces and moments, which can lead to tilting of the scroll plate and cause leakage, noise, and additional frictional wear. With a suitable design such as the one proposed here, we observe that the compliance mechanism can eliminate the unbalanced forces on the scrolls and prevent the additional frictional forces between the scroll tips for variable operating frequencies.

Several numerical methods are adopted during this analysis. For example, a finite element code (ANSYS) is used to predict the deformation of the compliance mechanism in the axial direction, a compressor-performance simulation package developed by us is used to calculate the gas forces for the FEM boundary conditions, and a method for optimizing the scroll tip clearance

between the two scrolls is implemented to design a leaf spring of suitable thickness.

3.4.2 Basic analysis

To simplify the analysis process of the proposed mechanism, the following basic assumptions are made.

- The fixed scroll has limited floating displacement in the axial direction.
- Only four dynamic forces directly act on the fixed scroll and are calculated precisely.
- The contact force between the orbiting scroll and the fixed scroll resulting from the tilting moment on the orbiting scroll is assigned a constant value determined on the basis of previous studies.

In this study, the four dynamic forces are axial gas pressure force, leaf spring forces, pressure pin forces, and backpressure force (see Fig. 3.16). During operation, the axial clearance between the fixed scroll and the orbiting scroll is determined by the equilibrium of the forces. The resultant force pushes the fixed scroll, eventually leading to contact between the fixed scroll and the orbiting scroll. This causes a frictional force and unnecessary mechanical loss, particularly at a low operating speed.

i. Backpressure Force

The backpressure force is the resultant force caused by the discharge gas pressure acting on the check valve, and it can be calculated from the following equation:

$$F_b = P_d \times A \qquad (3.5.2\text{-}1)$$

Here, F_b is the force acting on the check valve; P_d, the discharge gas pressure from the backpressure chamber; and A, the cross-sectional area of the check valve.

ii. Pressure Pin Force

The pressure pin force arises from the pressure difference between the suction gas and the discharge gas in the high-backpressure chamber acting on the pressure pin surface and from the downward force of the fixed disk spring. It is calculated from the following equation:

$$F_{pin} = (F_{disk} + F_{pd}) \times 3 \qquad (3.5.2\text{-}2)$$

where F_{disk} is the disk spring force and F_{pd} is the net force resulting from the pressure difference between the suction gas and the discharge gas in the high-backpressure chamber acting on the pressure pin surface. Three pins are considered in this analysis.

iii. Axial Gas Force

The axial gas force is caused by the pressure distribution in the compression chambers between the fixed and orbiting scrolls. The axial force acting on the fixed scroll is calculated from the following equation:

$$F_g = P_d \times A_d + P_m \times A_m + P_s \times A_s \qquad (3.5.2\text{-}3)$$

where F_g is the axial gas force; P_d, the discharge pressure; P_m, medium pressure; P_s, the suction gas pressure; A_d, the area of the discharge chamber; A_m, the area of the middle chamber; and A_s, the area of the suction chamber.

iv. Leaf Spring Forces

The total force caused by the displacement of the leaf spring is computed by the following equation:

$$F_s = N \times K \times X_s \qquad (3.5.2\text{-}4)$$

where N is the number of leaf springs; X, the displacement of the leaf spring; and K, the spring stiffness.

During scroll operation, a tilting moment is exerted on the orbiting scroll, which can result in the application of a contact force to the fixed scroll. The contact force is a major cause for the reduction in the compression efficiency and the increase in noise level. The four dynamic forces need to be designed suitably for achieving stable motion. This can be achieved by satisfying the following conditions.

$$F_b \geq (F_g + F_{tx}) \qquad (3.5.2\text{-}5)$$

Here, F_{tx} is the contact force. It is difficult to precisely calculate the value of F_{tx}. In general compressor design, an initial guess value will be assigned from experience.

3.4.3 Prototype

In order to design a leaf spring used in the prototypes with appropriate thickness, a finite element simulation package (ANSYS) is employed to calculate the axial displacement of the leaf spring (see Fig. 3.17). The active forces calculated from the compressor-performance simulation software (developed by ITRI) are introduced as the boundary conditions. In the FEM model, the leaf spring is made of SKD11 steel; the scrolls, FC300 cast iron; and the fixed ring for the fixed scroll, AISI 1040 steel. Further, all the screws are made of SCM435 steel. The FEM is shown in Fig. 3.18. One of the simulation results is shown in Fig. 319.

According to the results of the FEM analysis, the leaf spring prototype is fabricated to have three different thicknesses (0.5 mm, 1.0 mm, and 1.5 mm) for further analysis. An photograph of the prototype of the compliance structure is shown in Fig. 3.20.

3.4.4 Experiment

For comparing the influence of different back clearances between the scrolls, a preliminary experiment is conducted by controlling the clearance of the prototype from 0.03 mm to 0.05 mm using a bolted case STC (as shown in Fig. 3.15). This experiment is conducted in a

compressor-performance testing room (in ITRI), and the operating conditions follow the ARI 550/590 standard. A verification experiment is also conducted for gaining a better understanding of the compressor power consumption under a low operating frequency with our proposed ACM. In this experiment, three types of leaf-spring designs are tested and the compressor speed is varied from 50 Hz (~3000 rpm) to 34 Hz (~2040 rpm). In Fig. 3.21, leaf spring 1 is 1.5 mm thick, leaf spring 2 is 1.0 mm thick, and leaf spring 3 is 0.5 mm thick.

3.4.5 Results and discussion

Results

(1) From the back clearance test, we observe that the back clearance (from 0.03 mm to 0.05 mm) influences the power consumption and the noise level (see Table 3-7).

(2) Power consumption decreases with an increase in the back clearance. From the test results of the prototype, we find that power consumption decreases by 11.7% .

(3) The compliance mechanism effectively controls the axial floating motion of the fixed scroll. From the test results of the prototype at a low operating speed, we find that the power consumption decreases steadily up to 1.4 kW (see Fig. 3.22).

(4) The effect of the thickness of the leaf springs is shown in Fig. 3.22. With an increase in thickness, the operating range decreases and the power consumption increases.

Discussion

(1) The dynamic backpressure in the back chamber can be increased under certain operating conditions. This causes increasing forces to act on the back plate of the fixed scroll. In this situation, the method for controlling back clearance is expected to be effective.

(2) The axial motion of the fixed scroll stabilizes with constraint of fixed ring; therefore, back clearance can be controlled by the leaf spring's rigidity.

(3) The fixed scroll undergoes a tilting motion during the normal operation, which can cause the deterioration of the STC's efficiency. The tracing action from the fixed scroll to the orbiting scroll can decrease the effect of the contact owing to the tilting motion. However, further experimental analyses are required to confirm this.

(4) More studies with low operating speeds of the compressor should be conducted to obtain information that is more useful for promoting this ACM.

In this section, a suspension-compliance mechanism with a fixed ring and two leaf springs has been proposed for an LPS STC, and the compressor performance of the prototype has been measured. The following conclusions are drawn.

1. Back clearance can influence the leakage of the scroll tips. In this study, we found that maintaining the back clearance at 0.05 mm could increase the volumetric efficiency by 3%.
2. The leaf spring's rigidity depends on its thickness. In this study, the ACM with a 0.5-mm-thick leaf spring had an operating speed range that was 2.4 times that of the ACM with a 1.5-mm-thick leaf spring.
3. With this prototype, the suspension-compliance mechanism functioned well when the STC worked under an operating speed ranging from 50 Hz (~3000 rpm) to 34 Hz (~2040 rpm), and it effectively controlled the back clearance, which resulted in low power consumption.

3.5 Remarks

The types of design for the ACM have been studied in sections 3.3–3.4. Further, the studies of the suspension-type ACM demonstrate high performance of the STC at a low operating speed.

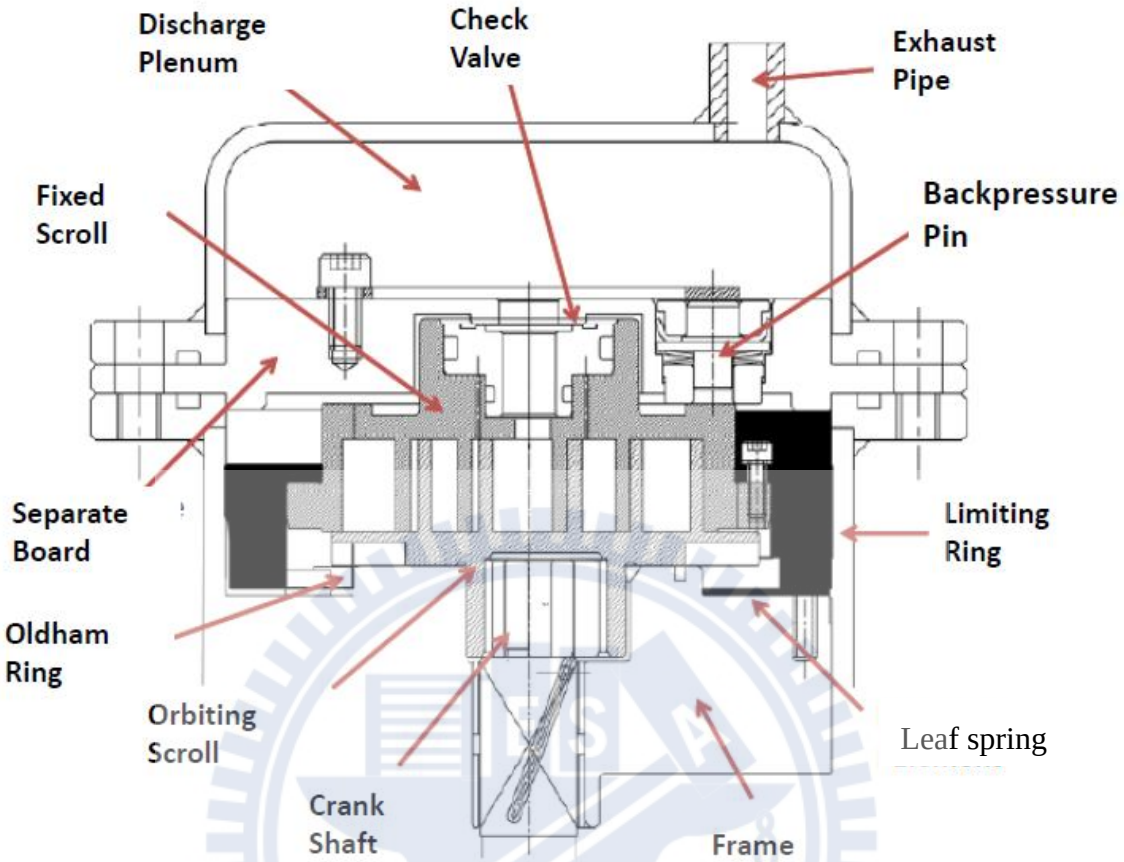

Fig. 3.1 Cross-sectional diagram of ACM designed for LPS STC

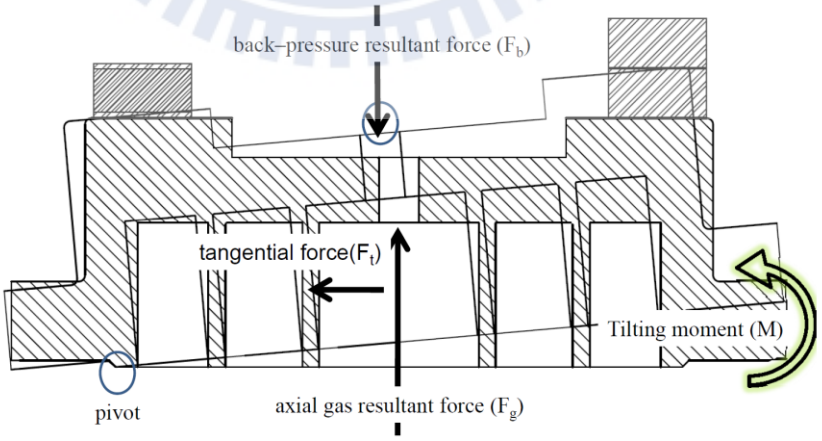

Fig. 3.2 Schematic of tilting motion and forces in fixed scroll

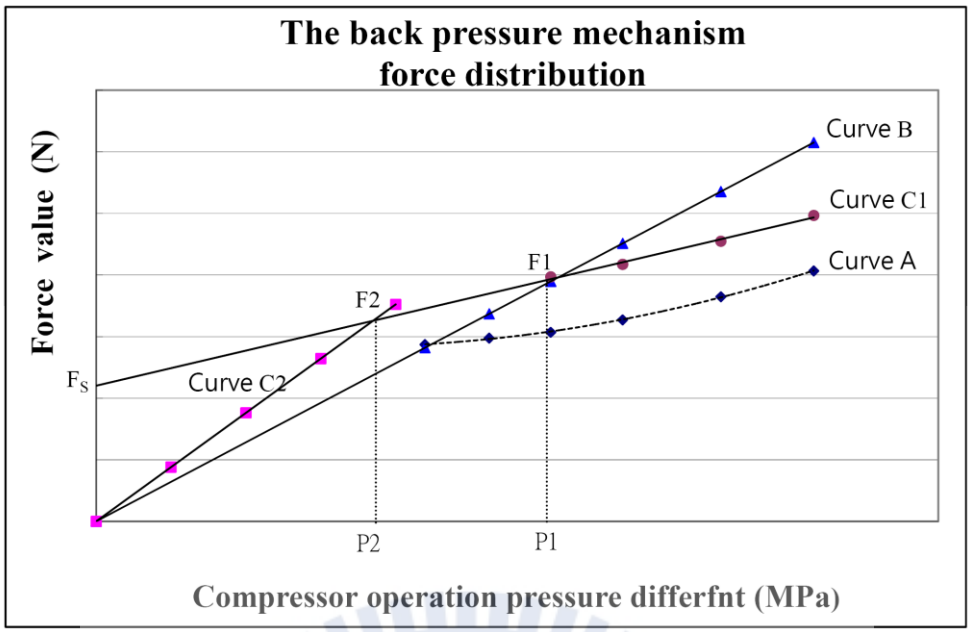

(a) The forces on the backpressure regulation mechanism

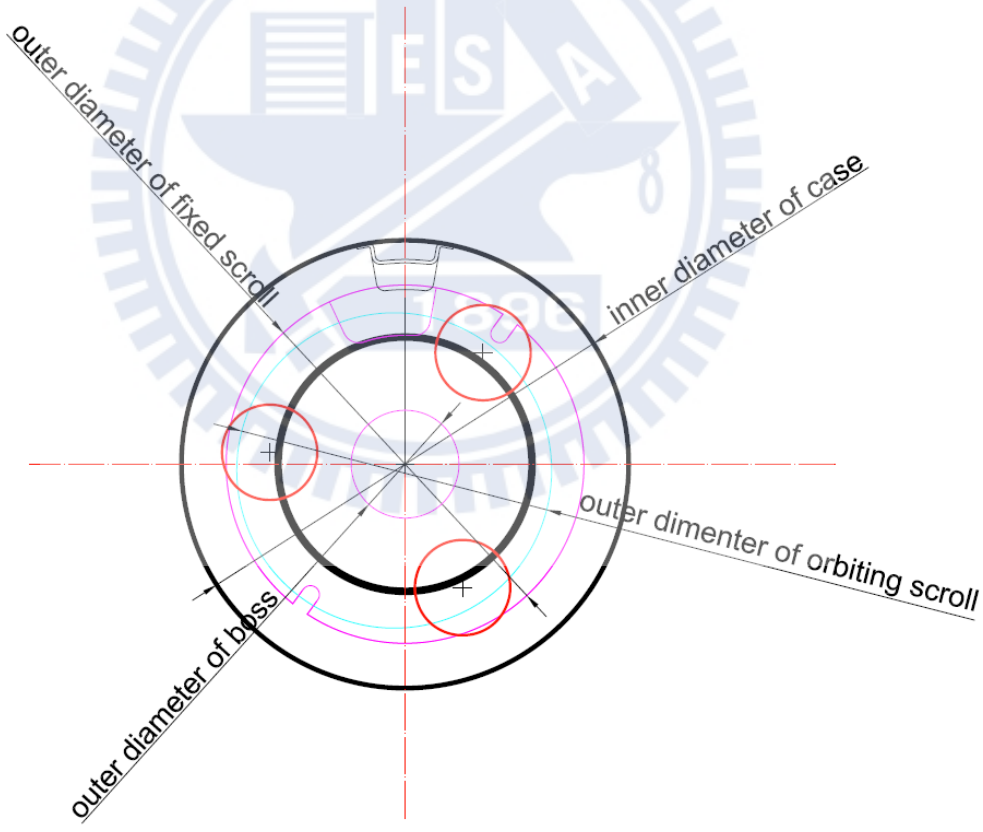

(b)The position design limited for the backpressure regulation pins

Fig. 3.3 The backpressure regulation mechanism

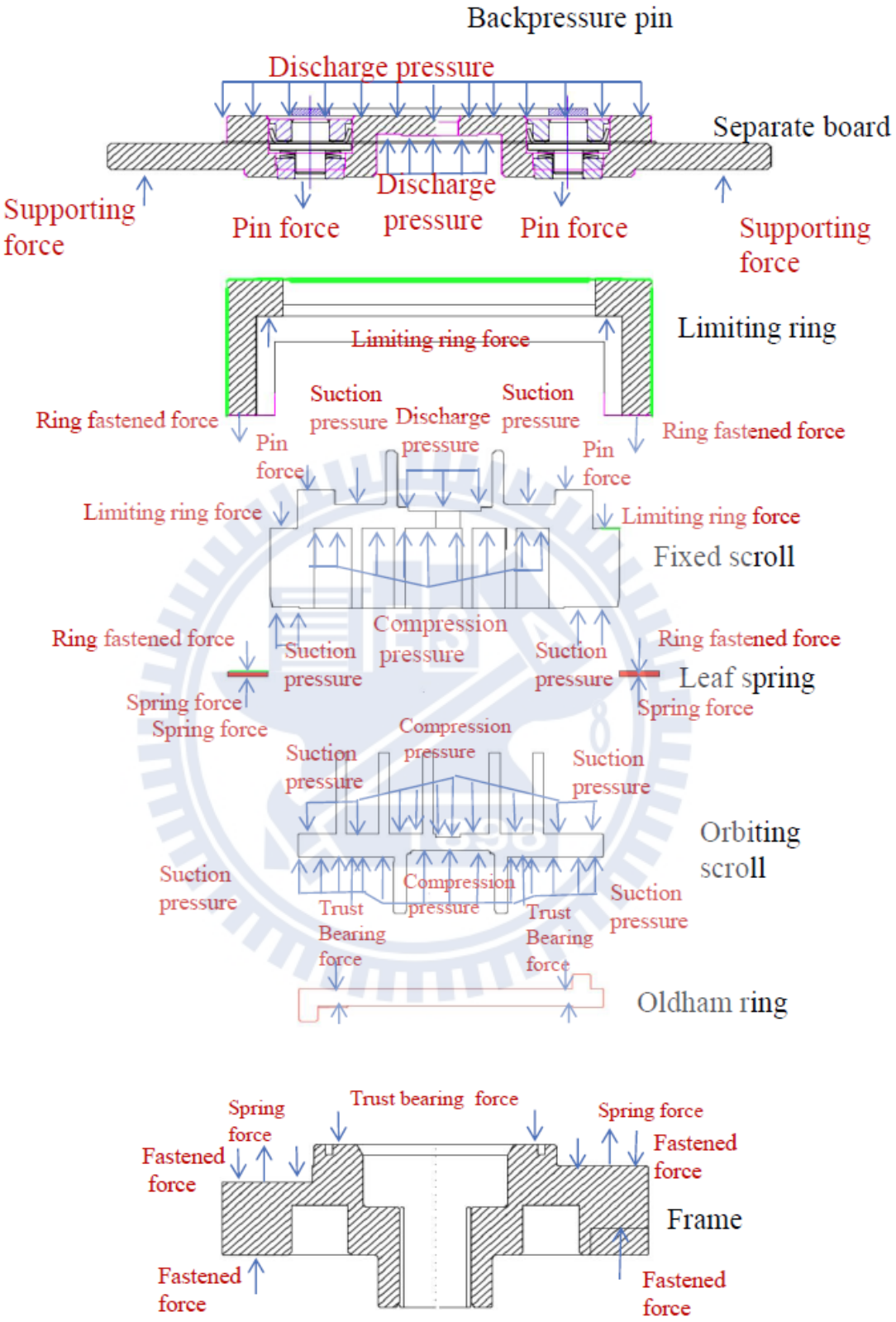

Fig. 3.4 The free body diagram of the ACM parts

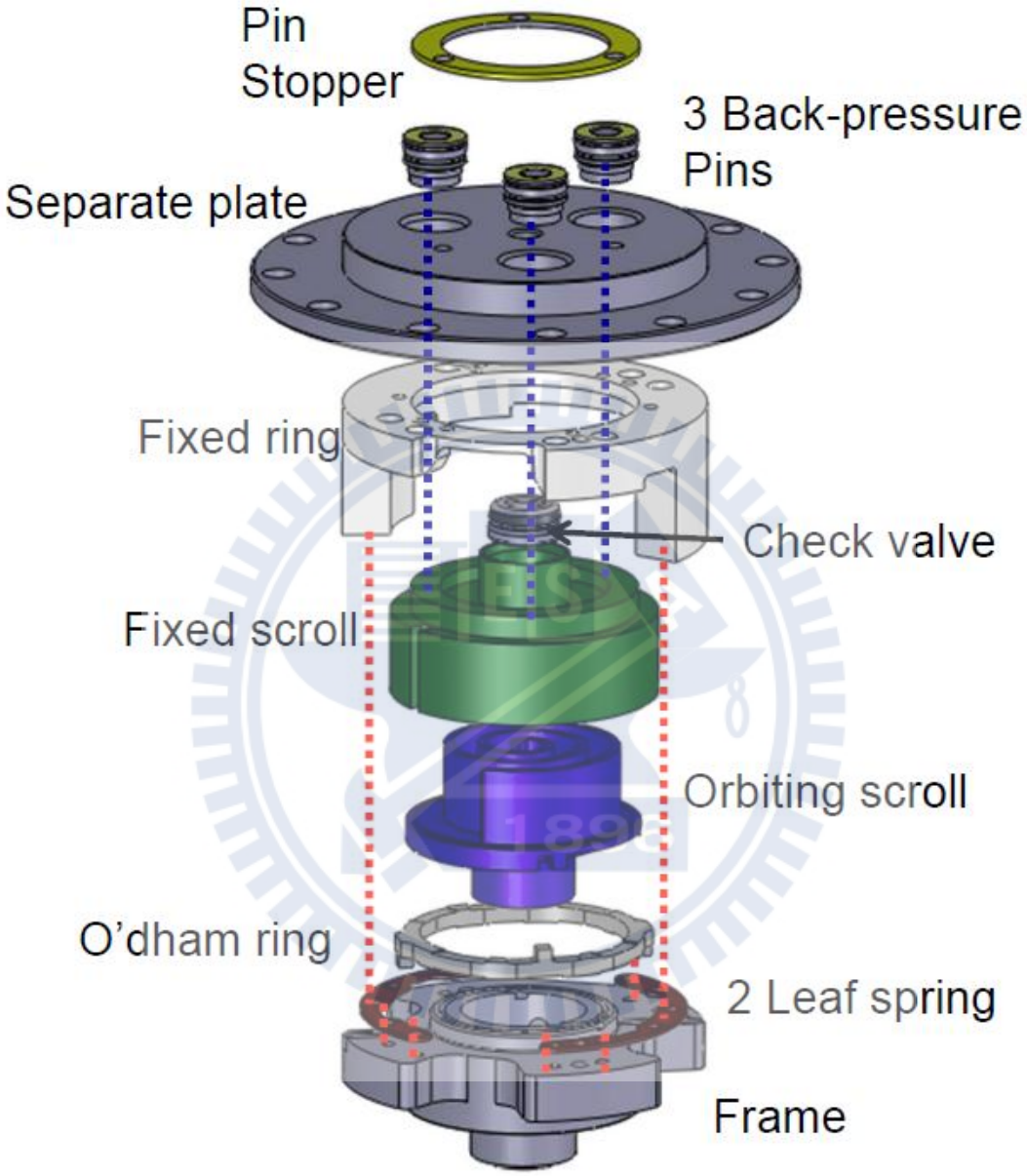

Fig. 3.5 The elements exploded diagram of the ACM

Table 3-1 Separate forces of fixed scroll at variable compressor operating conditions

(For backpressure mechanism design I)

Condenser Temperature (℃)	gas force in Scroll chambers (N)	force of the low pressure area (N)	Scroll separating force (N)
45.0	5571.61	2702.22	2869.39
50.0	5618.82	2702.22	2916.60
54.4	5711.98	2702.22	3009.76
60.0	5892.62	2702.22	3189.80
65.0	6236.24	2702.22	3534.02
70.0	6634.59	2702.22	3932.37

Note：

（1）Evaporator temperature @ 7.2 ℃.

（2）Superheat is10 ℃K and subcool is 8.3 ℃K.

（3）All values are calculated by ITRI STC simulation package.

Table 3-2 Simulation results of backpressure mechanism forces

(For backpressure mechanism design II)

Condition	Condenser Temperature (℃)	High Pressure (MPa)	Low Pressure (MPa)	Pressure Difference (MPa)	Pin Force (N)	Boss Force (N)
a	45.00	1.729	0.625	1.104	368.43	1657.72
b	50.00	1.943	0.625	1.318	440.35	1981.34
c	54.40	2.146	0.625	1.521	509.33	2291.81
d	60.00	2.428	0.625	1.803	589.87	2654.07
e	65.00	2.701	0.625	2.076	699.96	3149.41
f	70.00	2.997	0.625	2.372	803.98	3617.38

Note：

(1) Low pressure is the saturation pressure of the evaporator temperature @7.2℃.

(2) All pressures on the table are "absolute pressure".

(3) All values are calculated by NIST REFPROP 8.0.

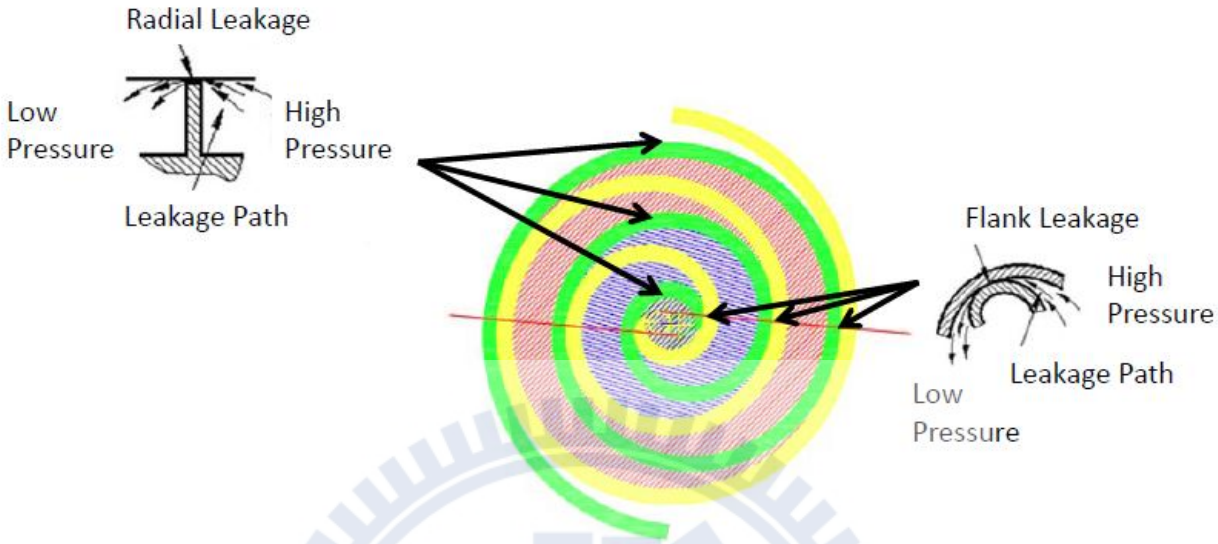

Fig. 3.6 Axial and side leakages

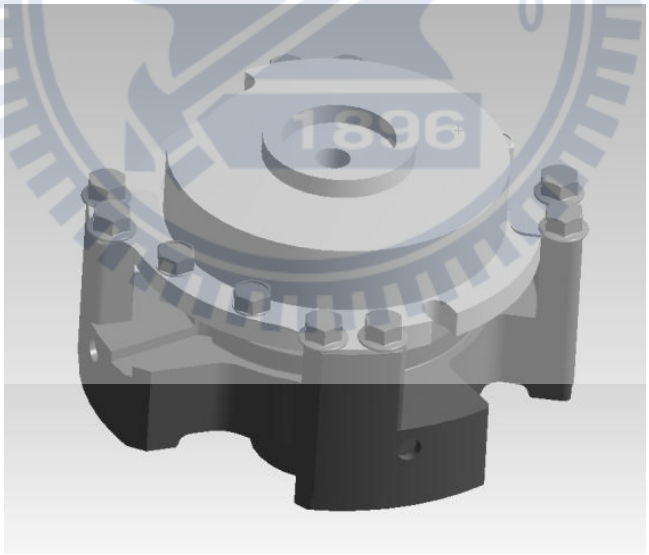

Fig. 3.7 Mechanism model I

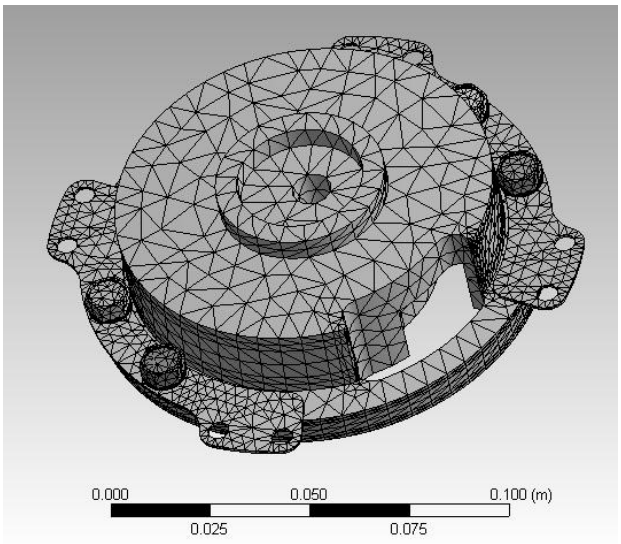

Fig. 3. 8 FEM mesh model I

3.

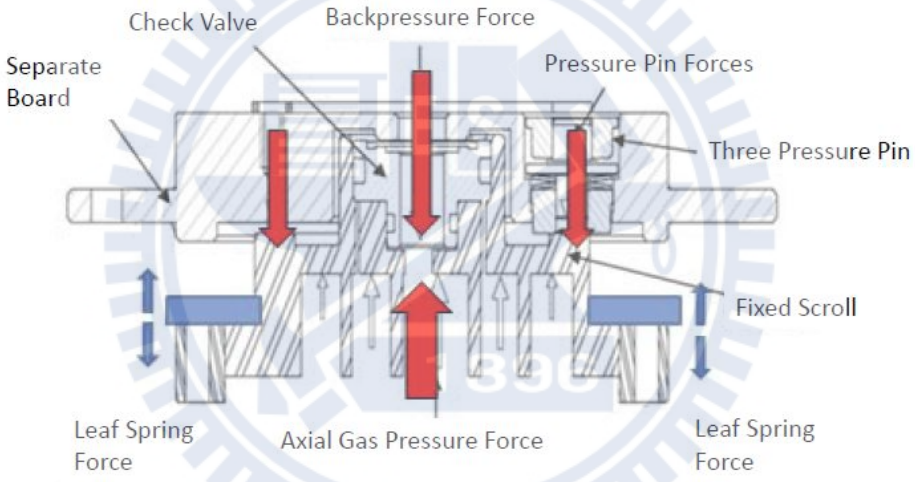

Fig. 3.9 Four forces acting on fixed scroll (model I)

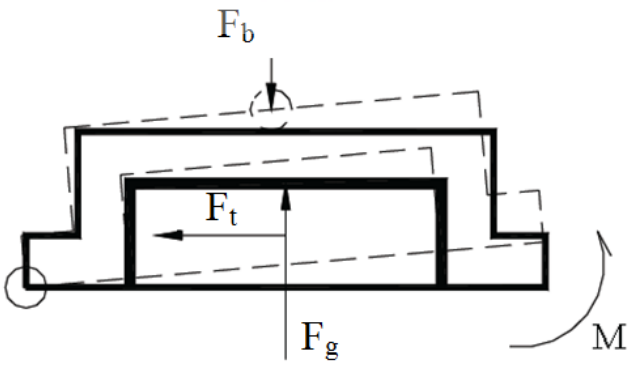

Fig. 3.10 Tilting moment on fixed scroll

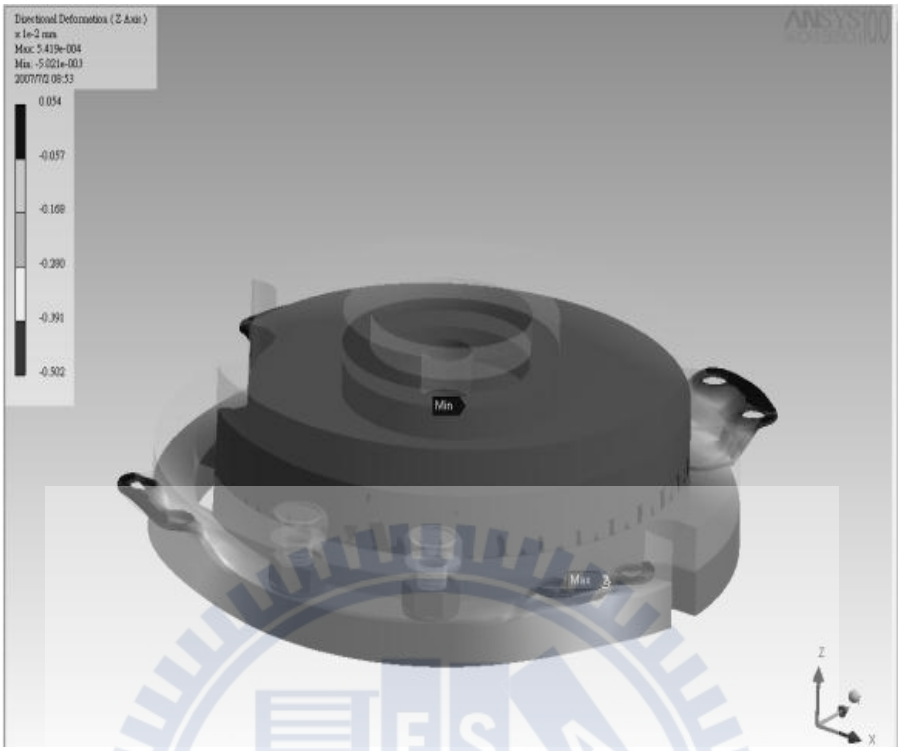

Fig. 3.11 ANSYS simulation of model I

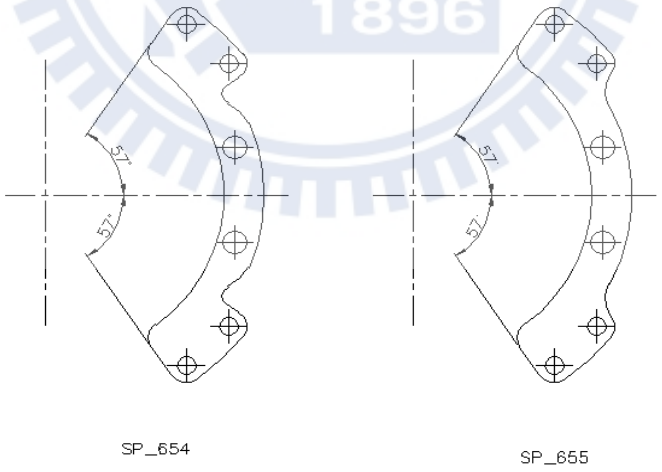

Fig. 3.12 Shapes of two leaf springs of model I

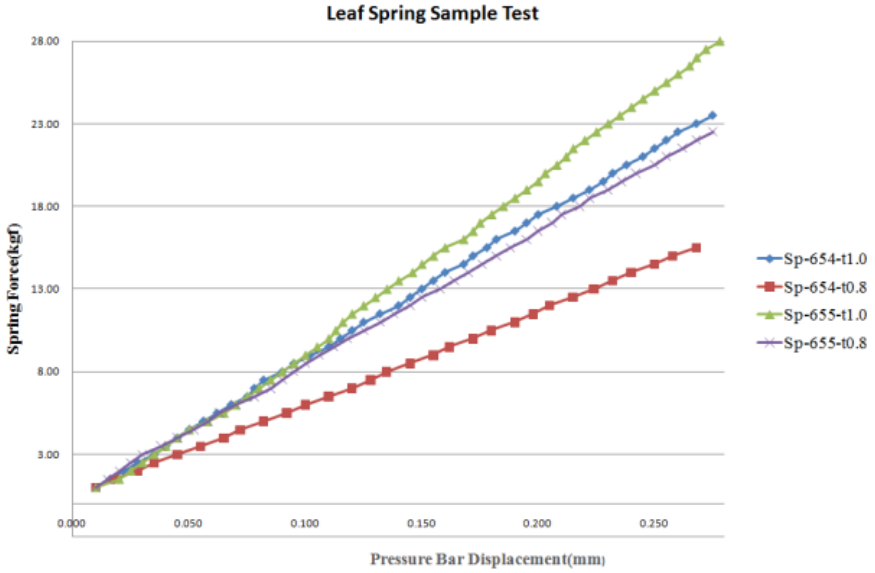

Fig. 3.13 Test results of spring prototype of model I

Table 3-3 Operating conditions of model I compressor

Condensing Temperature	Evaporating temperature	Degree of Subcooling	Degree of Superating
54.4℃	7.2℃	8.3℃	27.8℃

Table 3-4 Test results of leaf spring of model I

Leaf spring type		SP_655 / 1.0t	SP_655 / 0.8t	SP_654 / 1.0t	SP_654 / 0.8t
Plate washer	spring stiffence(kg/mm)	185.05	101.25	135.24	77.22
	spring force(kgf)@pressure 0.04mm	9	4.5	6.5	3.5
	spring force(kgf)@pressure 0.09mm	18	9	12.5	7
Spring washer	spring stiffence(kg/mm)	120.27	95.92	97.76	63.99
	spring force(kgf)@pressure 0.04mm	4	4	4	3
	spring force(kgf)@pressure 0.09mm	9.5	9	9	6

Table 3-5 Test results of model I compressors

Test Specification		TEC			
Prototype#		SP_655 / 1.0t	SP_655 / 0.8t	SP_654 / 1.0t	SP_654 / 0.8t
Discharge Tempera	℃	109.3	109.4	109.2	109.4
flow rate(cal-h)	kg/h	166.07	166.58	166.47	166.13
flow rate(meter)	kg/h	160.51	161.08	160.75	160.75
flow rate defense	%	-3.3	-3.3	-3.4	-3.2
power consumption	W	2451.4	2442.1	2438.0	2430.8
cooling capacity	kcal/h	6808.8	6825.0	6816.7	6809.7
EER	kcal/hW	2.78	2.79	2.80	2.80
volume efficiency	%	91.2	92.3	92.2	92.2

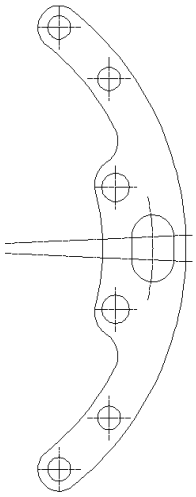

Fig. 3.14 Shape of leaf spring #Sp-663 in model I

Table 3-6 Test results of noise of model I

Test Condition		TEC
spring type		SP_663 / 0.8t
Discharge temperature	℃	108.3
Current	A	10.85
Motor speed	rpm	3469
power	W	2449.1
cooling capacity	kcal/h	6811.8
EER	kcal/hW	2.78
volumetric efficiency	%	91.5
noise	dB(A)	58.7
vibration	μm	24.0

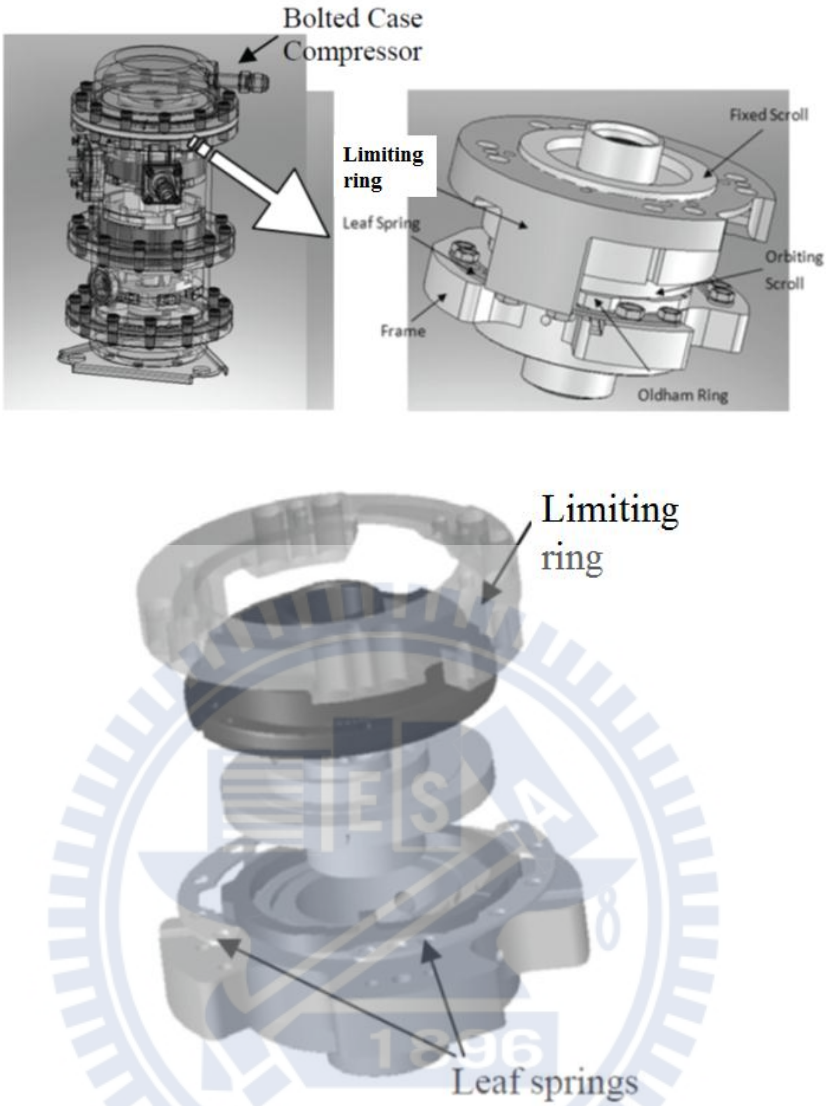

Fig. 3.15 Concept structure with suspension-compliant mechanism in LPS STC

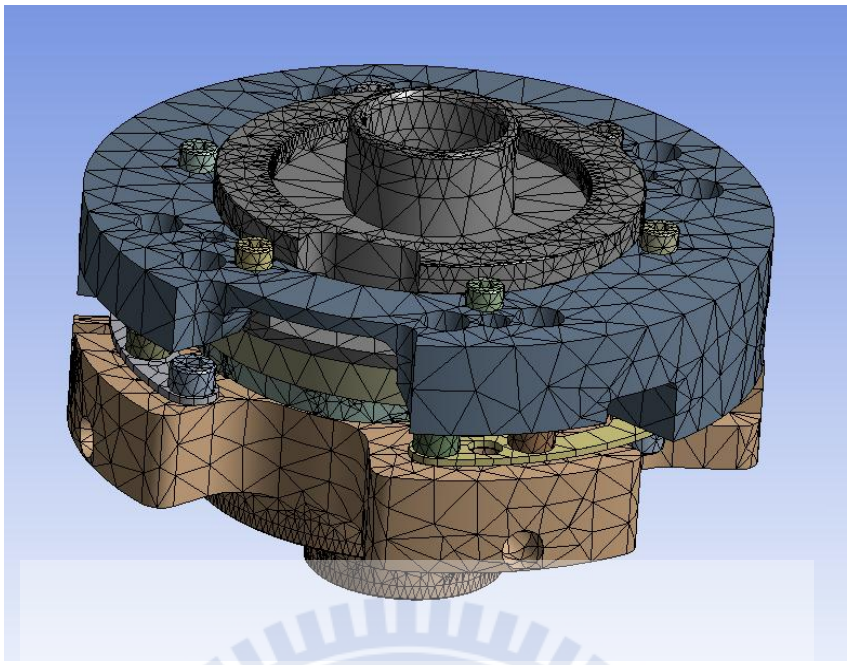

Fig. 3.16 Model for FEM analysis

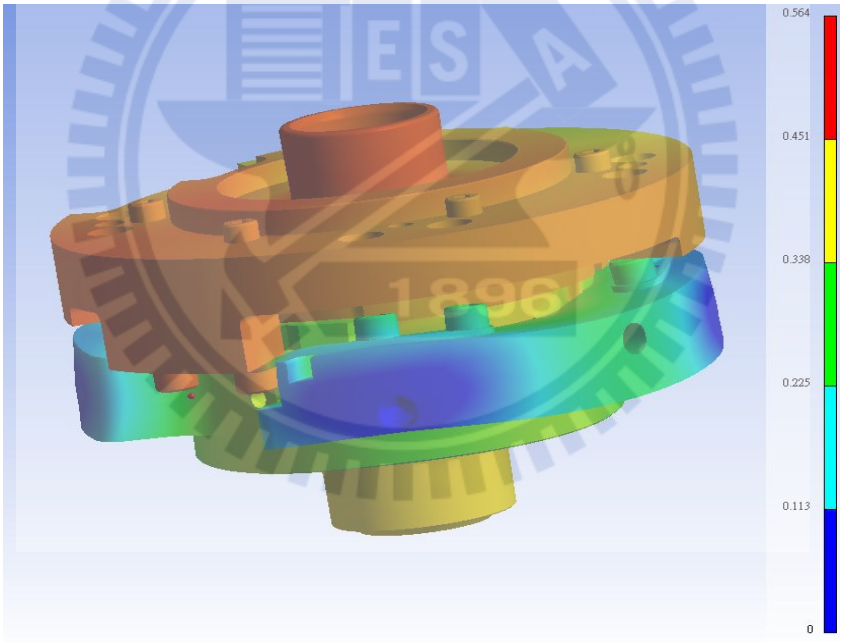

Fig. 3.17 Finite element analysis result

Fig. 3.18 Prototype of ACM

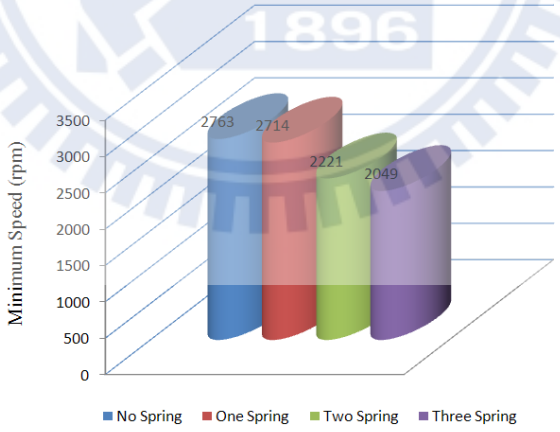

Fig. 3.19 Lifting spring thickness versus minimum speed

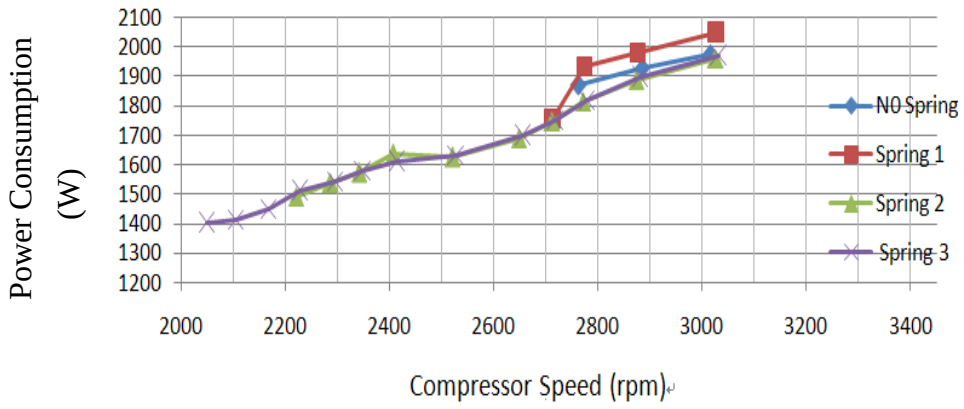

Fig. 3.20 Leaf spring thickness versus power consumption

Table 3-7 Test results

Back Clearance (mm)	Power (W)	Current (A)	Cooling Capacity (kcal/h)	Noise (dBA)	Semi-Amplitude (μm)	Flow Rate (kg/hr)	Volume (%)
0.03	2777.3	14.8	6277	65	15	153.9	89.3
0.04	2492.7	11	6603.8	64	13.8	161.9	92.4
0.05	2451.3	10.9	6590.7	61.74	12.75	161.6	92.3

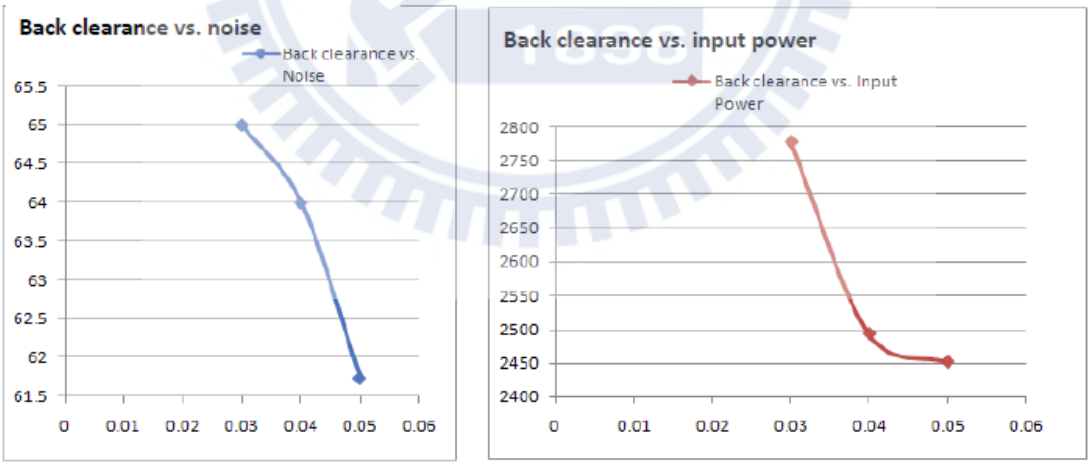

Fig. 3.21 Investigation of back clearance

CHAPTER 4 STUDY ON R22 STC DEVELOPMENT AS A DESIGN BASELINE

In this chapter, we discuss the influence of an extended operating speed of the STC. We use the ACM design method and the structure discussed in chapter 3. Here, the same design is used in the case study for developing a variable-speed LPS STC using R22 refrigerant.

4.1 Suspension ACM Model of R22 STC

In order to evaluate the ACM prototype, the developed STC was tested using a custom-built PWM inverter placed in a compressor's test load stand" or "compressor load stand. As shown in Fig. 4.1, the test load stand consists of three major parts: a control system, an arrangement of a water cooling/heating refrigeration system to maintain fixed suction and charge conditions, and a testing chamber to maintain constant environmental temperature.

The test bench was operated using a classical refrigeration cycle with three main components: a water-heated evaporator, water-cooled condenser, and electronic expansion valve. An oil-separator system was constructed to ensure the accuracy of the refrigerant mass flow meter. The STC performance was measured under ASHRAE-T conditions [38] by varying the operating speed from 40 Hz to 80 Hz (Table 2-1). A control system was used to maintain the specified suction pressure and temperature. The cooling capacity was determined by the refrigerant mass flow rate, compressor speed, and the gas density of the suction refrigerant.

In the case study, the condenser and evaporator temperatures were maintained constant by automatically adjusting the inlet/outlet water flow rate in the heat exchangers using a

proportional-integral-derivative (PID) controller. The uncertainty in the refrigerant flow rate was estimated to be ±1% of the measured value. The specifications of the load stand and the STC prototype (test sample) are listed in Table 2-2. The controlled operating conditions and the test method (test standard) are also listed in Table 2-1. The tested compressor is a semi-hermetic STC with the developed PWM inverter as the driver (Fig. 4.1(b)). The compressor speed is regulated by this inverter, and the inverter output is the adjusted magnitude and frequency.

In order to verify the thermal balances of each component and the overall system, the pressures, temperatures, electrical powers, and flow rates were measured at the main positions of the test bench. The test results are of the power consumption, refrigerant flow rate, isentropic efficiency, and COP.

4.2 Simulation and experiment

4.2.1 Results of variable-speed tests

In this section, we discuss the results of the performance of the developed STC with and without the ACM. The test conditions are listed in Table 2-1. The operating frequency of the compressor was varied from 40 Hz to 80 Hz; the actual revolutions measured are also listed in Table 2-1.

Fig. 4.2(a) shows the test results of the compressor power consumption. Under conditions A–E, which represent the compressor with the ACM, the power consumption ranges from 1.97 kW to 3.59kW. However, without the ACM, the power consumption ranges from 2.07 kW to 3.72 kW. Under the rating condition (condition C), the power consumption of the compressors

with and without the ACM is approximately identical. The results show that the power consumption of the STC with the ACM is less than 3%–5% of that of the STC without the ACM.

Fig. 4.2(b) shows that the overall COP increases from 4.7% to 13.5%. Under the rating condition (condition C), the COP values for the compressors with and without the ACM are also nearly identical. As shown in Fig. 4.3, the growth rate (under condition D) of the noise level decreases, which is characterized by the gentle curve. Overall, the tests show that the noise level improved from 0.7 dB to 1.4 dB, whereas a large divergence occurred under the rating condition (condition C). The results of the noise level tests also show a discrepancy within 3%.

4.2.2 Discussion of development of ACM for R22 STC

Fig. 4.2(a) and (b) implies that the ACM design reduces not only the leakage loss but also the frictional loss. Furthermore, the slightly increasing trend of the rating speed shows that the rating condition is suitable as a design base. The ACM operates extremely well for clearance control and maintenance of high volumetric efficiency. The power consumption increases from 3% to 5%, and the overall COP increases from 4.7% to 13.5%; however, the volumetric efficiency must also increase to improve the cooling capacity.

The stiffness effect of the elastic element increases the ability to maintain the position of the fixed scroll while decreasing the tilting moment; further, the limiting ring maintains the position of the fixed scroll and reduces the degree of freedom of the scroll motion in the axial (vertical) direction. In this manner, the ring limits the fixed scroll such that the scroll moves only in the axial direction. This reduces the probability of contact between the scrolls and lowers the compressor noise level. The ACM also reduces the high-frequency operation noise when the operating point is greater than that given under condition D. This is probably a result of

structural improvements.

4.3 Remarks on development of ACM for R22 STC

In this study, a suspension ACM with a limiting ring and two elastic elements (two crescent leaf springs) was proposed for improving the STC performance. For the theoretical simulations of the leakage effect, a simplified leakage model was introduced in a numerical simulation package to improve the calculation time. The radial leakage could be precisely controlled within a preferred clearance distance. The performance test results of our STC prototype with the ACM design demonstrated that the proposed mechanism improves the COP at operating speeds that are both lower and higher than the rating speed. The conclusions are summarized as follows:

(1) Radial clearance (tip clearance) influences the leakage of scroll tips. Our simulation results show that the clearance should be less than 6 μm; this ensures that the volumetric efficiency does not decrease with various operating speeds.

(2) The suspension ACM functions well at operating speeds from 80 Hz (condition E) to 40 Hz (condition A). The test results show that the overall COP increases from 4.7% to 13.5%; moreover, these values are maintained even at higher speeds because of the effective control of the radial clearance. Further, the power consumption is lower with the use of the ACM design.

(3) The fixed ring structure constrained the fixed scroll and limited it to movements only in the axial direction. On the other hand, the backpressure acting on the fixed scroll transferred its forces to the frame via the springs and caused a sufficient downward sealing force, leading to COP enhancement.

Finally, the limiting ring prevented the scrolls from crashing, which led to reductions in the

operating noise at extended operating speeds. The effect of the ACM mechanism is based on the difference between the suction pressure and the discharge pressure. However, different refrigerants have different operating pressure differences. In this study, the R22 refrigerant can be treated as the design base for other refrigerant applications. Future studies may focus on the R744 refrigerant for a considerably higher pressure difference. In this manner, our ACM mechanism design improves the performance of the LPS STC at extended operating speeds.

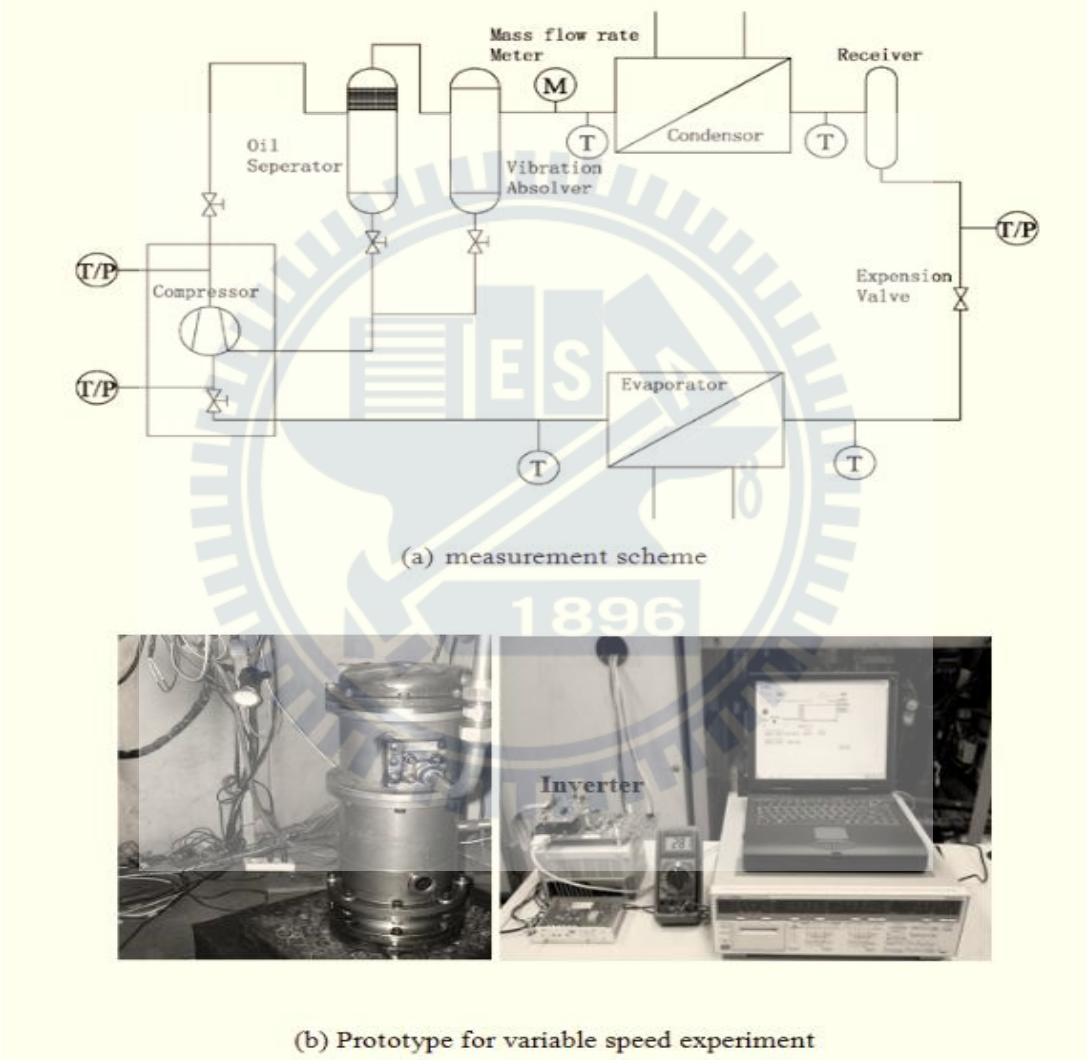

Fig. 4.1 Test rig scheme and experimental setup: (a) Measurement scheme (b) Prototype for variable-speed experiment

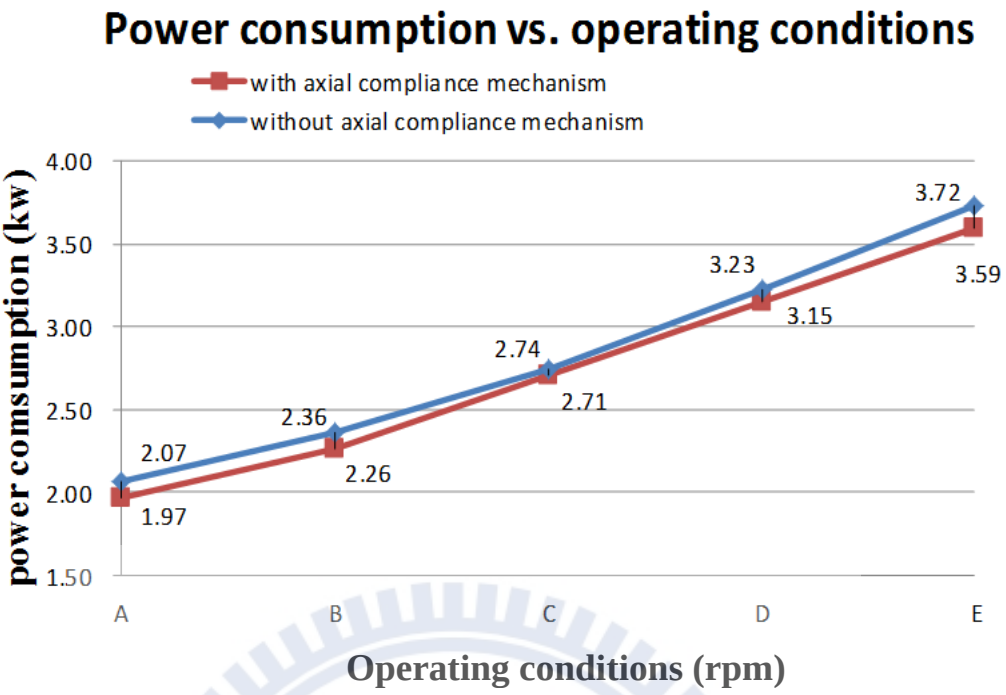

(a) **Power consumption vs. Operating conditions**

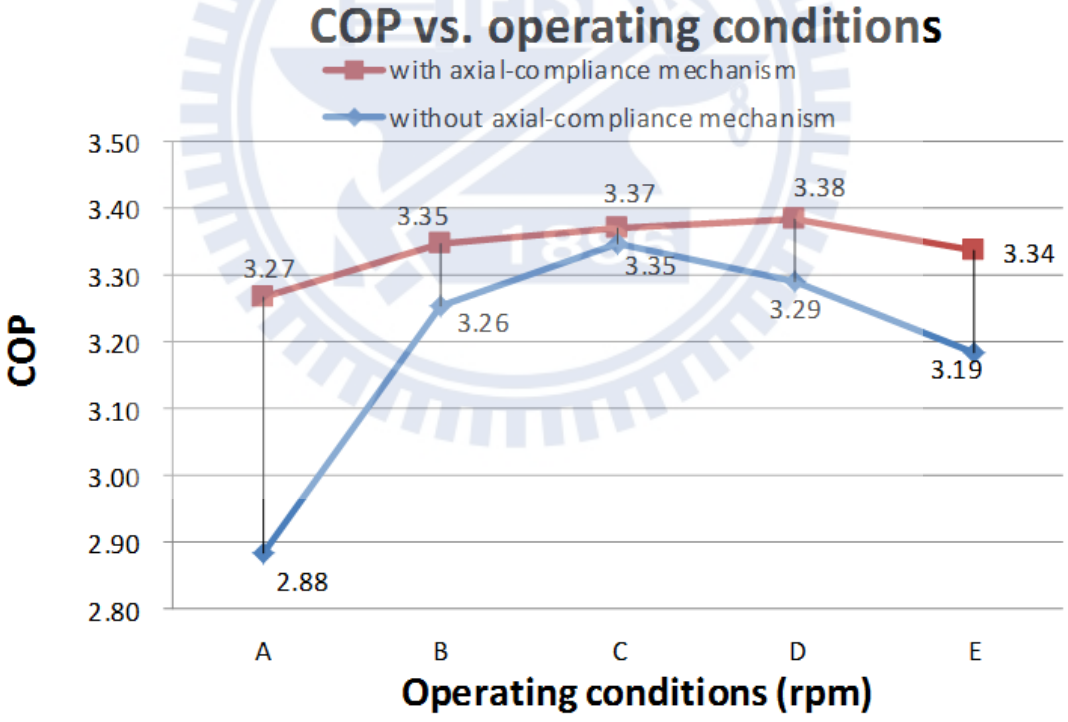

(b) **COP vs. Operation conditions**

Fig. 4.2 Experimental results: (a) Power consumption versus **Operation conditions** (b) COP versus **Operation conditions**

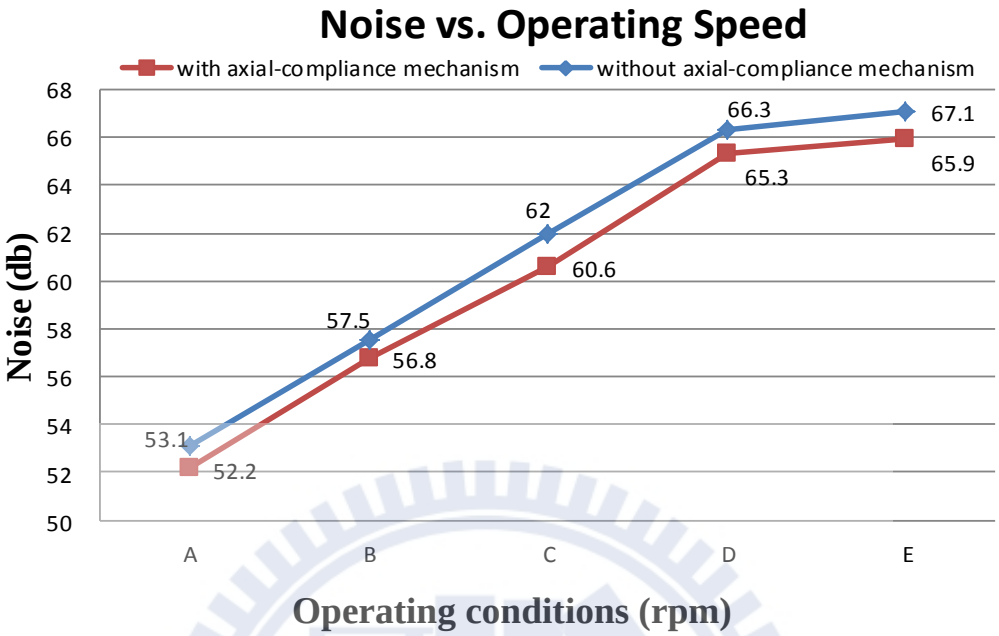

Fig. 4.2 Noise versus **Operation conditions**

CHAPTER 5 CASE STUDIES OF ACM APPLICATIONS

5.1 Comparative study on characteristics of alternative refrigerants

5.1.1Performance investigation of refrigerants as alternatives to R22

R22, as a high-performance artificial refrigerant, has been used widely for many years in vapor-compression refrigeration systems. Furthermore, it is generally accepted and is the most suitable refrigerant for many applications such as air conditioning (high temperature and high backpressure), refrigeration (medium temperature and medium backpressure), and freezing (low temperature and low backpressure) applications. Unfortunately, R22 belongs to the family of hydrochlorofluorocarbon (HCFC) refrigerants, which are considered harmful to the ozone layer. Now, the HCFC refrigerants are controlled substances according to The Montreal Protocol, and they will be phased out by 2020 in developed countries and by 2030 in developing countries [39~43]. Ozone-friendly alternative refrigerants can be grouped into the following three categories:

(1) Hydrofluorocarbons (HFCs) that are used in conventional vapor compression cycles, such as R134a, R410A, and R407C.

(2) Natural fluids, which include carbon dioxide (CO_2) and hydrocarbons (HCs), such as R600a, propane (R290), and ammonia (R717). Although these refrigerants have zero ozone depletion potential (ODP) and minimal global warming impact due to direct emissions, safety and environmental factors associated with these fluids exist, which would limit their widespread use as refrigerants.

(3) Alternative cycles that include absorption systems and the use of trans-critical CO_2 (R744) and air cycles. However, these alternative cycles do not offer the same energy efficiency as the vapor compression cycle using HFC refrigerants. Moreover, they

increase indirect global warming emissions via increased electrical power consumption [43~45].

Blends of the HFC refrigerants have been considered the preferred candidates for R22 alternatives because they are harmless to the ozone layer owing to the absence of chlorine, and these fluids are the most used substitutes [46][47] (Table 5-1). Research on refrigerants for R22 alternatives is a popular topic in the refrigeration and air conditioner industries. Many refrigerants show a great potential as R22 replacements [48]. The results of a search for ideal alternatives to R22 show that a binary mixture (R410A) was found to be a suitable substitute in air conditioning and medium-temperature applications [49]. Aprea et al. [50] evaluated the performances of R22 substitutes having a regulated refrigeration capacity in a vapor compression plant by a variable-speed compressor.

R410A is composed of R32 and R125 with weight percentages of 60% and 40%, respectively, and has the advantage of high heat transfer coefficients in the evaporator and the condenser. Therefore, R410A shows a further potential for increasing the efficiencies of the refrigeration system. Further, with very low temperature glide (<0.2 K), the general application of R410A is nearly identical to that of a pure refrigerant. [46]. However, the high pressure levels of R410A during operation may require major design changes to the compressor and other critical parts. Another disadvantage is its relatively low critical temperature of 73 ℃, which is a design limitation of the condensation temperature. R404A is a blend that is absolutely chlorine free (ODP = 0). Its basic components belong to the HFC group. Therefore, R404A has also been considered as a long-term alternative refrigerant. R404A is a mixture of R125, R134a, and R143a with weight percentages of 44%, 4%, and 52%, respectively. The major characteristic of all the three components is the very low isentropic compression exponent, which leads to a very

low discharge temperature. Thus, a highly efficient application of single-stage compressors with low evaporating temperatures is guaranteed [51].

In general, the compressor pressure ratio (R_p) is given as follows:

$$R_p = (\frac{p_d}{p_s}) \tag{5-1}$$

where p_d is the compressor discharge pressure (kg/cm^2) and p_s is the compressor suction pressure (kg/cm^2).

The values of p_d , p_s , and R_p result from the operation cycle and are influenced by the refrigerant used. Fig. 5.2 shows the different types of operation cycles with different refrigerants. The compressor pressure difference (p_d - p_s) is nearly identical in the R22 and R404A cycles. Furthermore, the pressure difference value of R410A is almost 1.2–1.5 times that of R22. Moreover, the value of R744 is nearly 2.2–3.0 times that of R22, but R_p of R744 is slightly smaller than that of R22. From equation (2-9), we can obtain a simple formula to demonstrate the relationship between total leakages with pressure difference:

$$\dot{M} = \sum \frac{dM}{dt} = L\rho_{mn}(\frac{\delta^3}{12\mu_{mn}l})[(p_d - p_m) + (p_m - p_s)] = L\rho_{mn}(\frac{\delta^3}{12\mu_{mn}l})(p_d - p_s) \tag{5-2}$$

The pressure difference can represented as

$$p_d - p_s = (CR - 1) * p_s \tag{5-3}$$

Here, CR is the ratio of the system pressure, and it is different for operating conditions with different refrigerants. It can be expressed as

$$CR = \frac{p_d}{p_s} \tag{5-3}$$

Generally, the suction state can be controlled by the system design, and the value of CR can be set by the designed operating conditions. For this reason, the case studies of the ACM applications in R410A, R404A, and R744 STCs can be considered for studying the backpressure mechanism with the same suspension structure (see the discussions in Chapter 3). In Fig. 5.3, R744 shows a higher pressure than the other refrigerants; the leakage in the R744 STC is discussed in section 5.2.

5.1.2 Literature review of leakage of CO2 gas with oil mixture in STC

In recent years, STCs, because of their low vibration, low noises, and high efficiency, have become an increasingly popular candidate for compressors in the refrigeration systems using CO_2 (R744) as the working fluid. These STCs have small axial and radial clearances between the orbiting and fixed scrolls, and the leakage of the compressed refrigerant gas through these small clearances has a strong, detrimental effect on the volumetric efficiency.

In order to carry out accurate compressor-performance simulations for efficiency optimization, it is necessary to establish a reliable method for calculating the leakage flow through these clearances. However, it should be noted here that the theoretical method for calculating the refrigerant gas leakages should be kept as simple as possible, as the numerical

simulations of the resultant performance include many complicated procedures. The previous studies by Ishii et al. [52] provide a very simple method for calculating the refrigerant gas leakage flows through the axial and radial clearances in an STC on the basis of the Darcy–Weisbach equation for incompressible, viscous fluid flow through a thin rectangular cross-section. The method proposed by Ishii et al. represents the gas leakage flows with the friction factor. In the beginning, a very simple experiment is carried out for studying the leakage flow through the axial and radial clearances for the dry refrigerants of R22, R410A, and CO2 (Fig. 5.4 & Fig. 5.5). Then, the leakage flow through the small clearances in the STCs is calculated using the Darcy–Weisbach equation to determine the empirical friction factors. However, the refrigerant gas is mixed with the oil for its sealing function during practical STC operation, and some researches show that the optimal oil content is about 5%, which results in the optimal performance of an air conditioning system.

Darcy–Weisbach equation:

$$h_l = f\frac{L_l}{D_l}\frac{V^2}{2g} \qquad (5\text{-}1)$$

The friction factor λ_a for dry and wet CO_2 gas leakage flows through the axial clearance can be given by (The friction factor λ_a can be given by Nikuradse's formula [53].) the following expression.

$$\lambda_a = 0.0032 + 0.35 \times R_e^{-1.52} \qquad \text{For dry } CO_2 \text{ gas leakage flow}$$

$$\lambda_a = 0.0032 + 0.30 \times R_e^{-1.22} \qquad \text{For wet } CO_2 \text{ gas leakage flow} \qquad (5\text{-}1)\ [52]$$

In Ishii's study, an oil-mixing device with a venture pipe was manufactured to permit very simple experiments on leakage flows of the wet CO_2 gas containing oil mist (Fig. 5.6). The wet gas with an oil mixture rate, initially pressurized in a large vessel, flowed out into the atmosphere through the axial clearance with a thin rectangular cross section. The pressure decay

due to gas leakage was measured at various initial pressures up to 3 MPa. The Darcy–Weisbach equation for incompressible, viscous fluid flow was applied to the leakage flow through the axial clearance for calculating the leakage mass flow rate.

Furthermore, the measured pressure decay was carefully simulated by assuming a polytropic process. The empirical friction factor was compared with that for the dry CO_2 gas. This result addressed the oil-sealing effect. The determined empirical friction factor for the wet CO_2 gas was incorporated into computer simulations to calculate the volumetric, mechanical, and compression efficiencies and the resultant overall efficiencies. By using the empirical friction factors, we can quantitatively address the oil–mist sealing effects on the compressor efficiencies by performing the computer simulations developed by Ishii et al. for optimizing the STC's performance [54~56].

Oku et al. [57] measured the pressure decay in the pressurized vessel due to leakage by using a maximum pressure of 3 MPa for CO_2 and 0.6 MPa for R22. The Darcy–Weisbach equation was applied for simulating the pressure decay characteristics. The simulation showed that the empirical friction factors for both axial and radial clearance leakage flows have nearly equal values for both CO_2 and R22, despite the significantly different working pressures. The friction factor was strongly dependent on the relative roughness of the leakage channel surface.

Table 5-2 lists the major specifications for CO_2 compressors, which are in accordance with those in Ishii's study. The inner compression ratio was 2.07 and system compression ratio was 2.57, resulting in a cooling capacity of 2.0 kW at the rated values of mean crankshaft speed. The suction and discharge pressures were 3.5 and 9.0MPa, respectively. The clearance between the orbiting and fixed scrolls was kept at 3.0 μm in the axial direction and 6.0 μm in the radial

direction. Although the abovementioned studies are focused on HPS STCs, the optimum axial clearance should be equal in both HPS and LPS STCs. Moreover, for different refrigerant applications, the results from Oku's study support the fact that the friction factor can be considered the same for both HPS and LPS STCs because "the friction factor was strongly dependent on the relative roughness of the leakage channel surface."

5.1.3 Numerical simulations of inner leakage effect on alternative refrigerants

For understanding the optimum scroll clearance of the alternative refrigerants-the R410A and the R744 (CO_2), in this study, we repeated the study steps in chapter 2 with the R410A and R744. Table 5-5 shows the parameters of R410A LPS STC and Table 5-7 lists the parameters of R744 LPS STC. Fig 5.7 show the simulation results of R410A and Fig. 5.8 show the results of R744. According to the simulation results, the optimum axial clearance can be considered to be 6.0 μm in the R410A application and 3.0 μm in the R744 application.

5.1.4 Remarks on the investigation of alternative refrigerants

(1) From sections 5.1.1 and 5.1.2, we find that the design of the ACM in LPS STCs should be determined with focus on the backpressure mechanism.

(2) The axial clearance can be considered to be 6.0 μm in the R410A applications.

(3) The axial clearance can be considered to be 3.0 μm in the R744 application.

(4) If the axial clearance is less than the values suggested in (2) and (3), then the friction factor strongly depends on the relative roughness of the leakage channel surface. However, this is a manufacturing problem and not a critical issue in design theory.

5.2 Basic ACM design configuration for case studies

5.2.1 Design configuration of backpressure pin mechanism

From section 5.1, the backpressure mechanism must be focused on for developing a suitable compliance mechanism in different refrigerant compressor applications. The optimum axial clearance between scrolls can be set to the values suggested in section 5.1. As the optimum clearances are objective factors and the backpressure mechanism can provide suitable compliance forces from the pressure pin design, the suspension mechanism can be used for maintaining the position of the fixed scroll for a wide range of operating conditions and at extended operating speeds.

First, the inner compressed gas forces should be determined by numerical calculations. From the design constraint in chapter 3, we observe that these forces are under a variable pressure differential arising from the variable condensation temperature at the designed rating speed. The curves of the forces (calculated by the ITRI compressor simulation package) presented in section 3.1 are used as the design base. However, the backpressure and the pin forces (curve B) are too large to force the fixed scroll down after the discharge pressure is designed. Therefore, the compliance forces exerted via the ACM (curve C1) should be slightly stronger than the scroll separation force (curve A) to provide the optimum sealing force. Therefore, the sum of backpressure and the pin disk spring forces (Fs) form curve C1. Curve C2 is formed only with the backpressure force and three pressure-pin forces. The design points at P1 and P2 can be used to determine the pushing forces F1 and F2, respectively.

In this section, it is shown that a different refrigerant application results in a different design base. However, the design point value depends on the pressure difference. Fig. 5.1 and Fig. 5.2

show that the pressure difference in R404A and R22 is nearly equal. Further, R410A has almost 1.5 times the pressure difference value of R22. Furthermore, these refrigerants are operated under subcritical thermal conditions. Unfortunately, the R744 application is operated under trans-critical thermal conditions, and its pressure difference value is about 3–5 times that of R22. The distribution of forces for the system using R410A and R744 are presented in section 5.3. The pin section and the disk spring specifications are determined from the force curves. The suspension mechanism design is focuses on the two-half-ring springs, and the mechanism is verified via CAE simulation. Section 5.2.2 shows the results of the CAE simulation for R410A. In addition, section 5.2.3 shows how to incorporate these results to design ACM for a small R744 STC.

5.2.2 Design configuration of suspension mechanism

In order to verify the leaf spring force design that can be used with R410A, numerical simulation of the pressure is carried out (using the ITRI package). The shape of the leaf spring can be designed as two half-rings to achieve balance. This study have considered the manufacture, assembly, and cost issues while designing the suspension mechanism described in this section. To resolve all the issues, two half-rings can be used for designing an appropriate system. This study use finite element analysis to determine the thickness of the leaf spring. The materials of the parts in the simulation model are as follows: SKD11 steel for the leaf spring, FC300 cast iron for the scrolls, and AISI 1040 steel for the fixed ring of the fixed scroll. All the screws are made of SCM435 steel. The simulation model in the finite element analysis is shown in Fig. 5.9. The pump of the compressor is assembled using a bolted case (see Fig. 1.1), and it is supported by the fixed support in the outer frame. In this simulation, the boundary conditions are calculated using the compressor-performance simulation program (developed by ITRI). Table

5-3 lists the boundary conditions used in this simulation. Table 5-4 lists the values of the backpressure force in this simulation. Fig. 5.10 shows the simulation results. These results show that the axial deformation can be constrained to within 6 μm by the designed ACM.

5.3 Case studies for different refrigerant applications

5.3.1 Case study of design for R410A STC

First, using the ACM design model from section 5.2, we have to modify the backpressure mechanism. The results of the analysis of the new forces are listed in Fig. 5.12. The R410A STC design parameters and operating conditions in the experiment are listed in Table 5-5. Here, the ACM design is applied to three prototypes of R410A STCs: One is a semi-hermetic vertical STC; the second, a semi-hermetic horizontal STC; and the third, a hermetic horizontal STC with the same mechanism as the semi-hermetic horizontal STC. All the three STC prototypes employ the same design of the scroll pump, ACM, and fixed-speed MS motor. The difference is that the second and third prototypes use a different oil circulation system. Fig. 5.13 shows the sections of the first two types of STCs. Fig 5.14 shows images of the prototypes being tested.

The hermetic horizontal R410A STC prototype follows the mechanism design of the semi-hermetic horizontal STC, but the assembly function is welded in the hermetic horizontal R410A STC prototype. Fig. 5.15 shows the photographs of the compressor parts and the final product. Table 5-6 presents a comparison of the performance data of the prototypes. The simulation data are obtained using the ITRI package to calculate the STC performance. However, the simulation results contain error within 5%, which may arise from the assembly tolerance, the motor quality, etc. In the simulation, the axial gap is set at 20 μm. For considering the simulation

error and the assembly tolerance, in the ACM design, the axial gap is set at 6 μm, which is in accordance with the mechanism for the R22 STC. The test results indicate that the leakage is reduced owing to the use of the ACM, as observed from the measured refrigerant mass flow rate data. The COP value is lower than the expected value. It is observed that this low value may be attributed to friction loss and the motor design (Fig. 5.16).

5.3.2 Case study of design for R744 (CO_2) STC

In this section, we discuss an R744 STC that is based on the 4.8 inch- frame R410A STC, which was evaluated in section 5.3.1, and has two applications. . From the comparison of refrigerants in section 5.1, we observe that the suction volume can be different for systems developed with the same design but with different refrigerants. This is because the refrigeration capacity of CO_2 is about 3.3 times that of R410A (please see table 5-1), which is due to the different operating conditions for the heat pump application and the refrigeration application. However, in this study, both the R744 STCs operate under the trans-critical cycle. The discharge and suction pressures are about three times those of the R410A STC. Therefore, the STC discharge volume is set at 4 cc/rev (in heat pump application; hpa) and 2.9 cc/rev (in refrigeration application; rea). For achieving a lower pressure ratio (2.7 in hpa and 2.4 in rea), the compressor frame should be small and the pump structure should be robust. In this study, the STC frame has a 4.4-in diameter and the ACM design follows the R410A design with a modified backpressure mechanism.

Fig. 5.17 shows the R744 semi-hermetic STC prototype for the CO_2 heat pump water heater (HPWH) application. Fig. 5.18 shows the R744 hermetic STC prototype with a high-pass voltage, and its mechanism is identical to that of the semi-hermetic STC prototype. For CO_2 HPWH

application, the discharge pressure is considerably higher than the other pressures because of the high discharge temperature. Fig. 5.19 shows the 3D model of the R744 LPS STC for the CO_2 bottle cooler application (BTCL). Fig. 5.20 shows the components of the BTCL STC prototype and the STC performance test. Unlike the HPWH application, the cooling capacity for the BTCL application is constrained by the inner volume of the BTCL. Furthermore, the evaporating temperature is below 0 ℃, and the suction pressure is the constraining factor. The inner leakage of the pump influences the speed at which the scroll pump builds up the lower suction pressure. Another constraining factor is the use of an internal heat exchanger (IHX). This increases the discharge temperature and the discharge pressure. The Fig. 5.21 shows the experiment results. According to the results, the R744 LPS STC with a suitable ACM design shows a good performance in bottle cooler application.

5.4 Remarks

In summary, the R410A and R744 LPS STCs with the ACM show a very good performance. The ACM design seems very suitable for all the refrigerants that can be used in the STC. However, the compressor test rig is designed only for testing the compressor performance under the specified suction and discharge conditions. The practical performance can be tested by using a feasible system such as the one discussed in appendix C. The R744 STC used for the BTCL application is only tested by the compressor test rig. The original 500-L BTCL prototype is built for a fixed-speed reciprocating compressor. The STC performance is better than that of the reciprocating compressor, although the refrigerant mass flow rate is not the same under the same operating condition. It cannot be established that the developed STC is indeed better than the reciprocating compressor. However, we could establish that the CO_2 STC can be used in medium-temperature refrigeration applications and has a better volumetric efficiency.

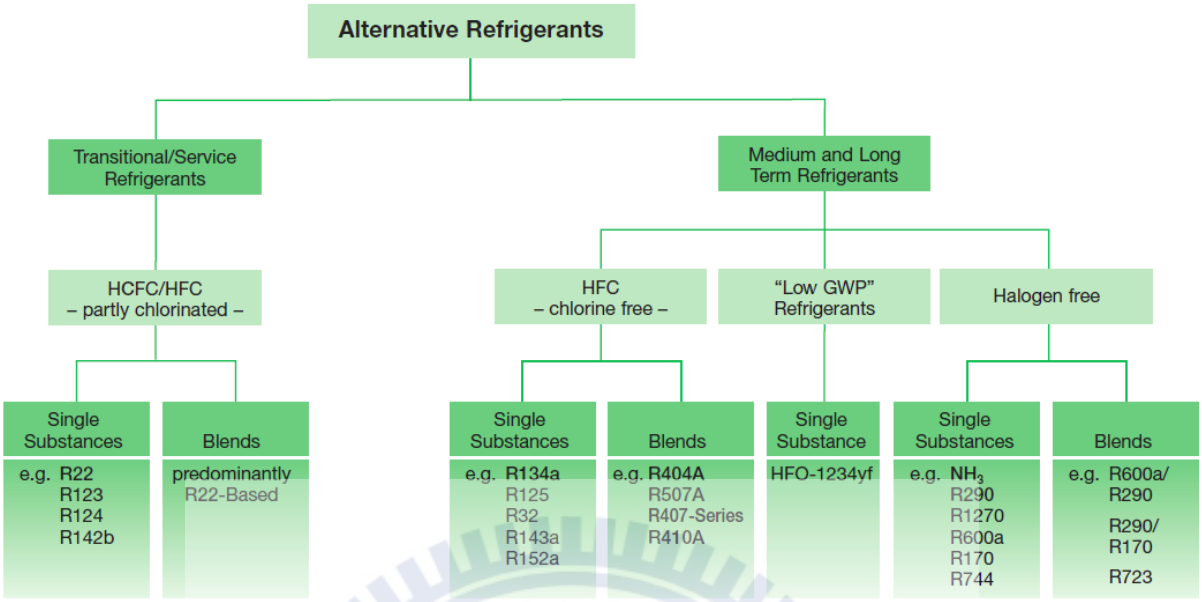

Fig. 5. 1 List of R22 alterative refrigerants

Table 5-1 Refrigerant comparison

REFRIGERANT COMPARISON

Refrigerant Type		*R22*	*R410A*	*R404A*	*R744*
ENVIRONMENT	*ODP*	*0.05*	*0*	*0*	*0*
	GWP	*1,700*	*1,900*	*3,760*	*1*
SAFETY	*Flammability/Toxicity*	*N/N*	*N/N*	*N/N*	*N/N*
THERMO-DYNAMIC	*Molecular Mass (kg/kmol)*	*87*	*73*	*98*	*44*
	Critical Pressure (bar)	*50*	*48*	*37*	*74*
	Pressure @ Room Temp (20 ℃) (bar)	*9.1*	*14.5*	*10.8*	*57.3*
	CriticalTemperature (℃)	*96*	*70*	*72*	*31*
	Normal Boiling Point (℃)	*-41*	*-53*	*-48*	*-78*
	Refrigeration Capacity (kJ/m^3)	*4,356*	*6,763*	*5,074*	*22,545*
HISTORICAL	*First Commercial Use as a refrigerant*	*1,936*	*1,998*	*1990s*	*1,869*

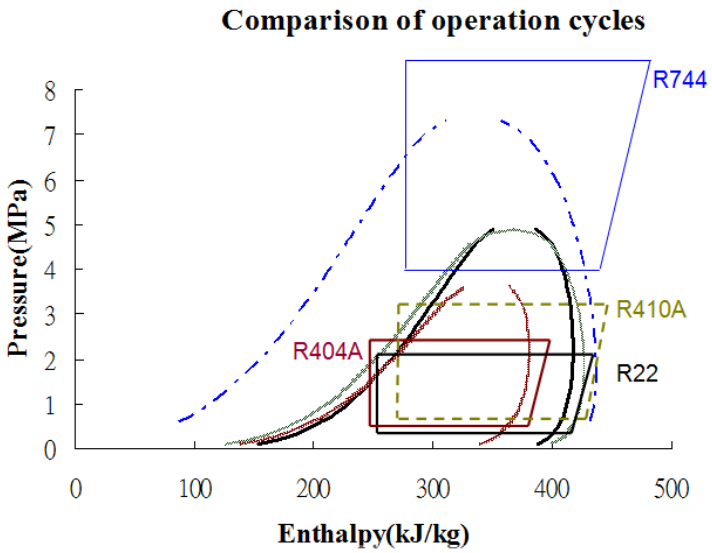

Fig. 5.2 Different operation cycles with different refrigerants

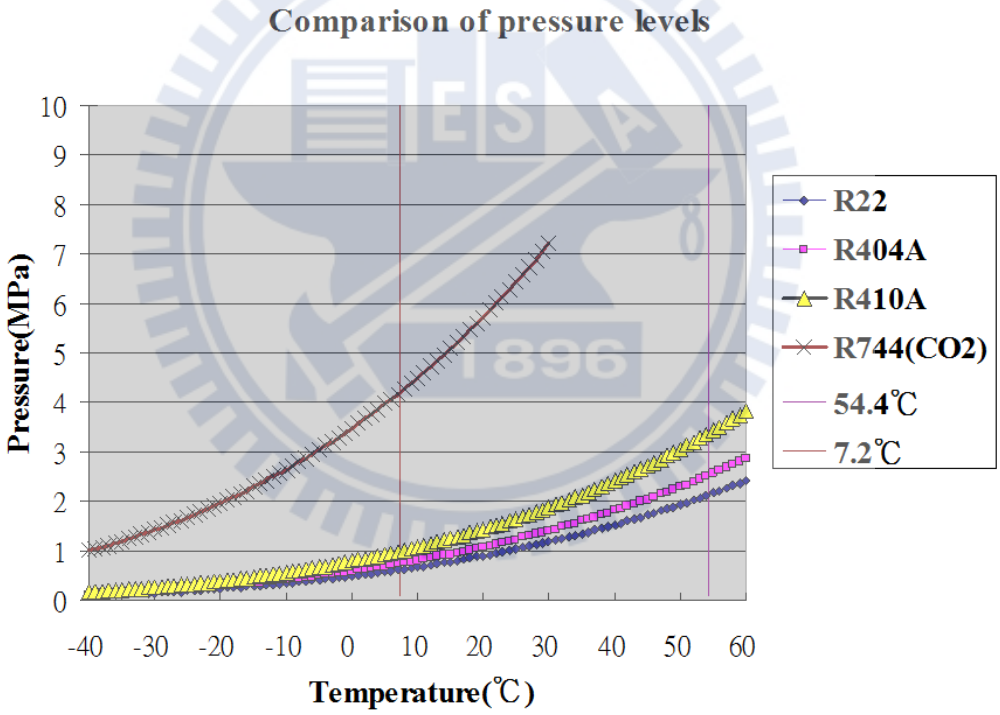

Fig. 5.3 Comparison of refrigerants in terms of pressure and temperature

where
h_f = head loss (m)
f = friction factor
L_l = length of pipe work (m)
D_l = inner diameter of pipe work (m)
v = velocity of fluid (m/s)
g = acceleration due to gravity (m/s²)

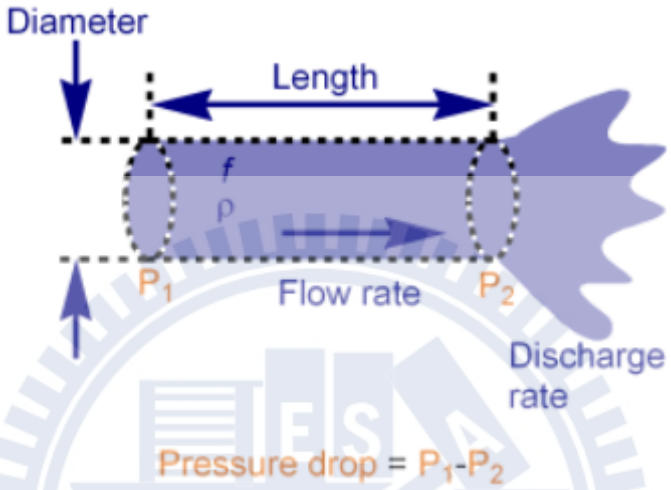

Fig. 5.4 Pressure drop in circular pipe

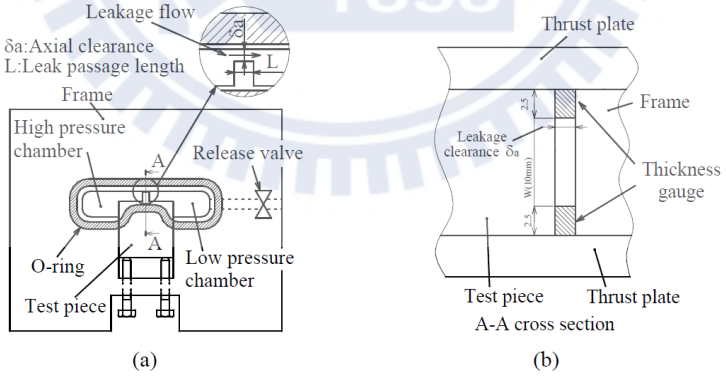

Fig. 5.5 Axial clearance model for gas leakage tests in STCs:

(a) Plane view; (b) Cross-sectional view [51]

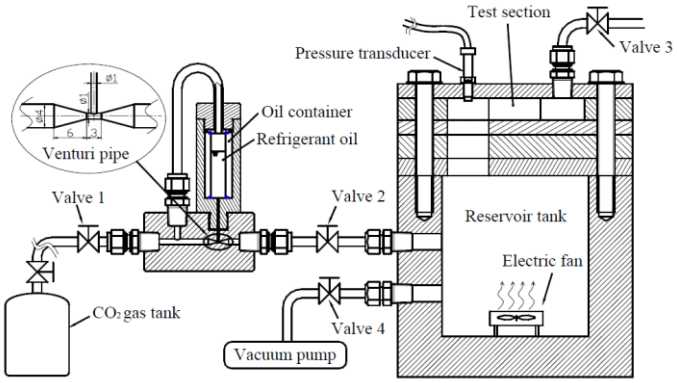

Fig. 5.6 Layout of leakage experiments with oil-mixing device [52]

Table 5-2 Parameter list of CO_2 compressor [51]

			Dry CO_2	Wet CO_2
Suction volume		Vs [cm³]	4.25	
Cooling capacity		[kJ/h]	727	
Operationg speed		[rpm]	3498	
Involute base circle		r_b [mm]	1.4 ~ 2.8	
Scroll height		B [mm]	9.7 ~ 3.6	
Scroll thickness		t [mm]	3.0	
Cylinder disameter		D [mm]	67.54	
Volume ratio			2.07	
Pressure ratio			2.57	
Specific heat ratio		κ	1.30	
Suction temperature		Ts [°C]	10.5	
Suction pressure		P_s [MPa]	3.5	
Discharge pressure		P_d [MPa]	9.00	
Axial clearance		δ_a [μm]	3.0	3.0, 0
Radial clearance		δ_r [μm]	6.0	
Empirical fric. factor	axial	λ_a	$0.0032+0.35Re^{-1.52}$	$0.0032+0.30Re^{-1.22}$
	radial	λ_r		
Moment of Crankshaft		I_0[kg·m²]	0.107~0.114	
Orbiting scroll mass		m_s[kg]	0.116~0.112	
Oldham ring mass		m_0[kg]	0.037	
Crankshaft radius		r_O[mm]	8.0	
Crankpin radius		r_S[mm]	8.0	
Fric. coef . at oldham ring			0.055	
Fric. coef . at thrust bearing				
Fric. coef. at crankpin			0.011	
Fric. coef. at crank journal				
Fric. coef. at ball bearing			0.0013	

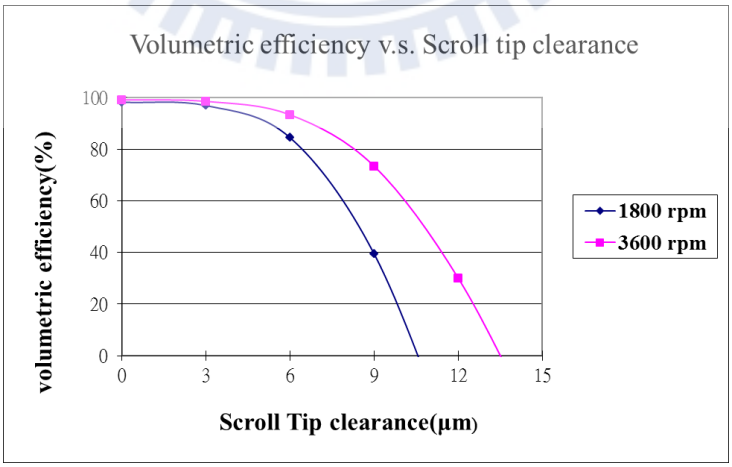

Fig. 5. 7 Numerical simulation results of leakage effect in the R410A LPS STC

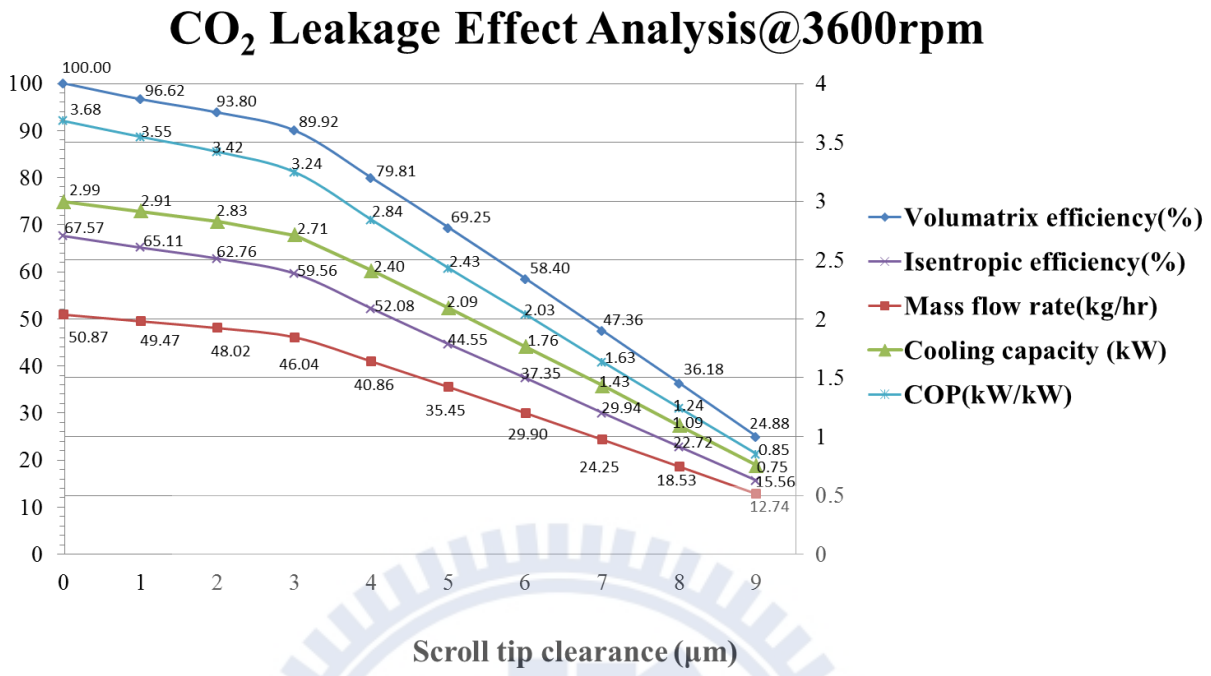

Fig. 5. 8 Numerical simulation results of leakage effect in the R744 LPS STC

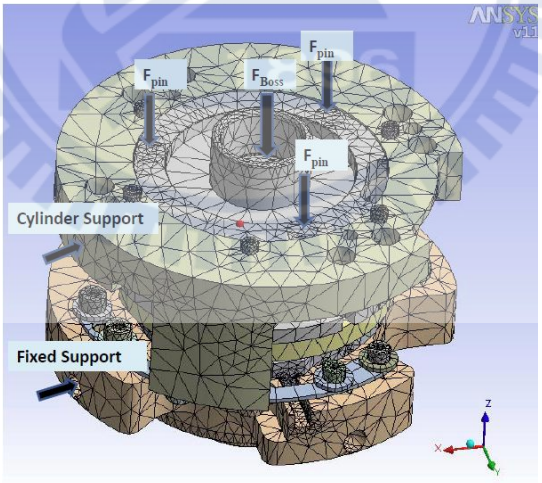

Fig. 5.9 CAE model and boundary conditions

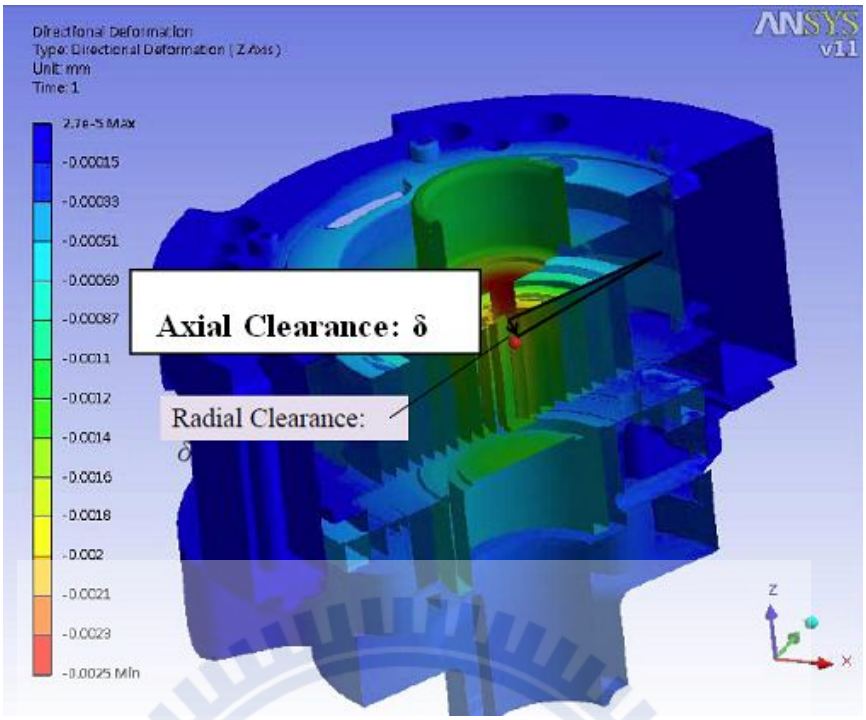

Fig. 5.10 CAE simulation results: Axial clearance

Table 5-3 Boundary conditions for CAE simulations (I)

Pd (kgf/cm^2)	Ps (kgf/cm^2)	ΔP (kgf/cm^2)	T_condensor (℃)	F_chamber (kgf/cm^2)	F_lower (kgf/cm^2)	F_backpressure (kgf/cm^2)
27.73	10.16	17.57	45.00	562.64	275.55	287.09
31.16	10.16	21.00	50.00	572.96	275.55	297.41
34.45	10.16	24.29	54.40	582.46	275.55	306.91
38.29	10.16	28.13	60.00	600.88	273.73	327.15
43.54	10.16	33.38	65.00	635.96	271.29	364.67
48.50	10.16	38.34	70.00	676.54	270.07	406.47

Table 5-4 Boundary conditions for CAE simulations (II)

Fpin (kgf/cm^2)	**Fboss** (kgf/cm^2)	T_condensor (℃)	**Fpin+boss** (kgf/cm^2)	Fspring (kgf/cm^2)	Pin_area (mm^2)
112.71	169.04	45.00	281.75	-	-
134.71	202.04	50.00	336.75	-	-
155.81	233.70	54.40	389.51	82.61	73.21
180.45	270.64	60.00	451.09	123.94	56.51
214.12	321.15	65.00	535.28	170.61	43.52
245.94	368.87	70.00	614.82	208.35	37.60

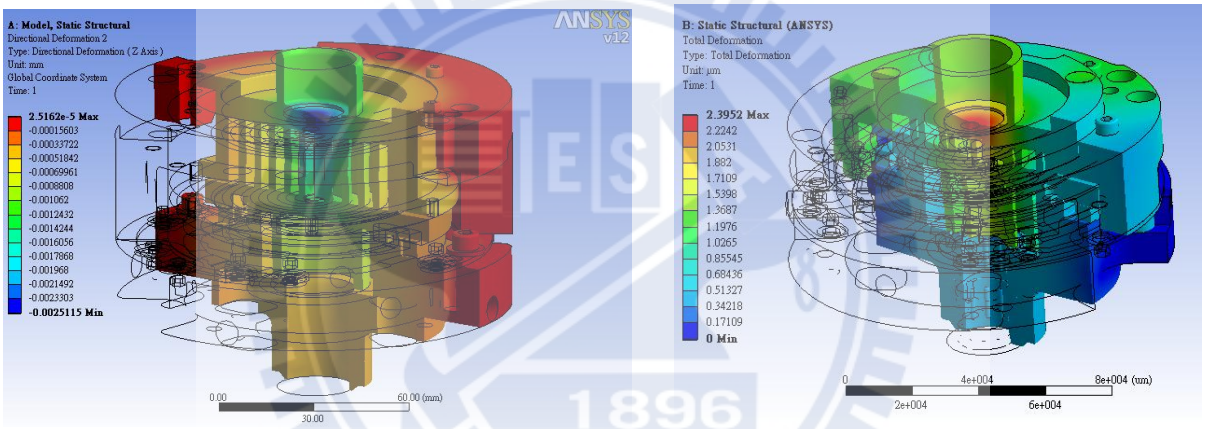

(a) Maximum axial deformation of R410A scroll pump

(b) Maximum axial deformation of R744 scroll pump

Fig. 5.11 CAE simulation results of ACM for R410A & R744 STC pump

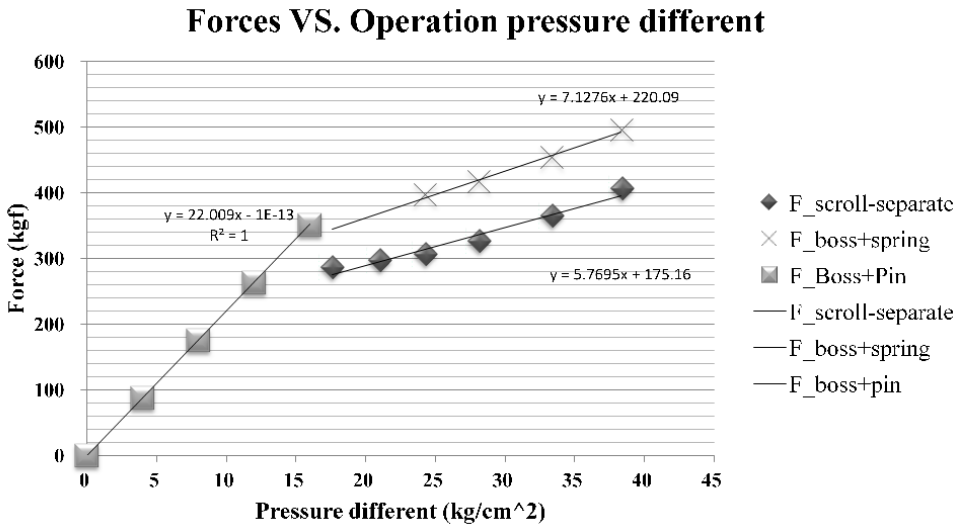

Fig. 5.12 Results of analysis of forces in backpressure mechanism

Table 5-5 R410A STC parameters and experimental operating conditions

Parameters of the LPS STC	
Parameters	Value
Radius of the basic circle of the scroll (r_b) (mm)	1.989
Thickness of the scroll (t) (mm)	2.75
Involutes angle of the scroll (φi) (degrees)	1050
Scroll pitch (Tp) (mm)	11.926
Scroll wrap height (hs) (mm)	18.7
Experimental operating conditions	
Environmental conditions	Value
Condenser Temperature (℃)	54.4
Evaporator Temperature (℃)	7.2
Superheat (K)	10
Subcool (K)	8.3
Expansion valve temperature (℃)	46.1
Refrigerant	R410A
STC operating speed	
Condition	Frequency setting (Hz) / Actual revolution (rpm)
MS Motor	60 / 3540

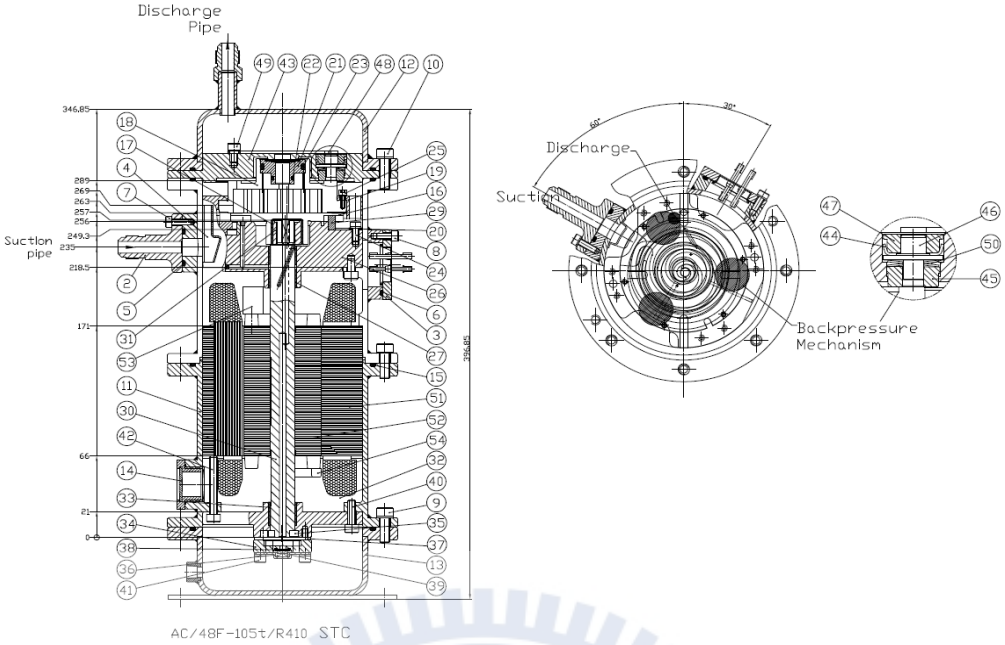

(a) Section of semihermetic vertical R410A STC prototype

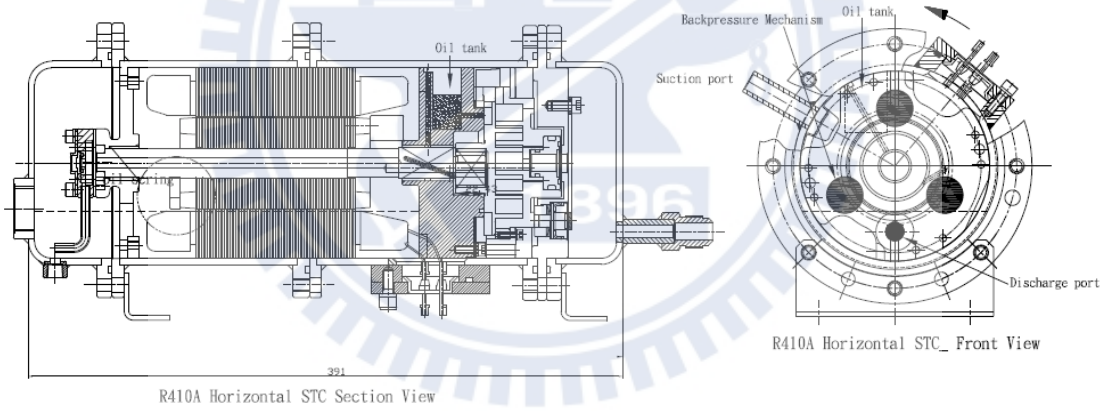

(b) Section of semihermetic horizontal R410A STC prototype

Fig. 5.13 Sections of semihermetic vertical and semihermetic horizontal STC prototypes

(a) Testing of semihermetic horizontal R410A STC prototype

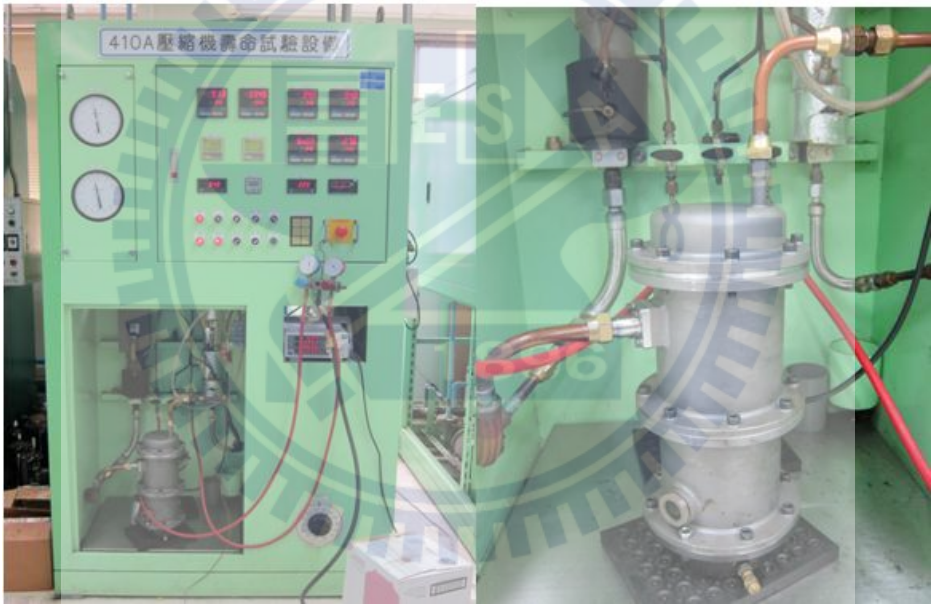

(b) Testing of semihermetic vertical R410A STC prototype

Fig. 5.14 Semihermetic vertical and semihermetic horizontal STC prototypes

Fig. 5.15 Hermetic horizontal R410A STC prototype and its testing

Table 5-6 Test results of R410A prototypes

Result \ Type	ITRI Package Simulation	Semihermetic Vertical	Semihermetic Horizontal	Hermetic Horizontal
EER (kcal/h/w)	2.55	2.42	2.56	2.41
COP (-)	2.96	2.81	2.97	2.8
motor input power (w)	1993	2300	2200	2442
refrigerant mass flow rate (kg/h)	117.98	129.6	130.8	136.8
refrigerating capacity (kcal/h)	5078	5576	5628	5886
Discharge Temp.	112℃	103.5℃	102.5℃	95.4℃

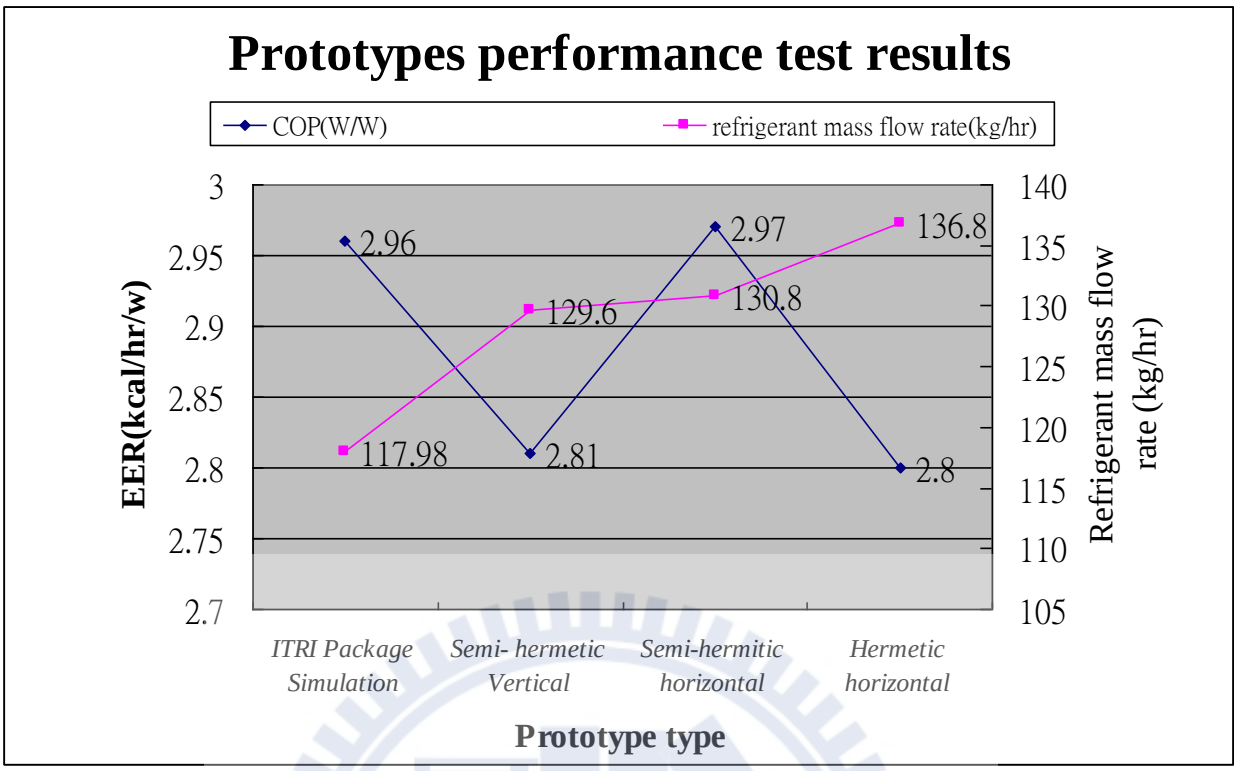

Fig. 5.16 COP performances of prototypes

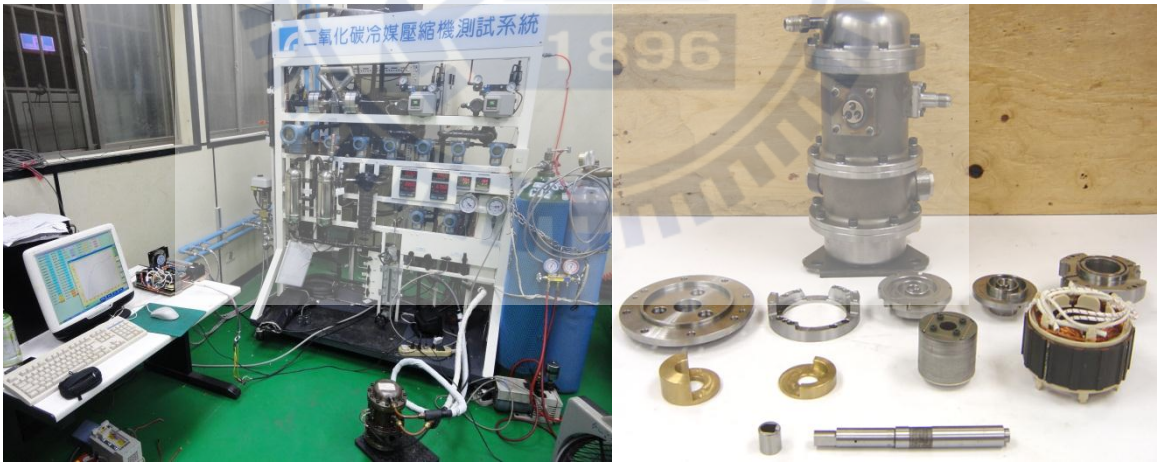

Fig. 5.17 R744 semihermetic STC for CO_2 heat pump water heater application

Fig. 5.18 Testing of R744 LPS hermetic STC for CO_2 heat pump water heater application

Table 5-7 R744 STC parameters and experimental operating conditions

Parameters of the LPS STC		
Parameters		Value
Radius of the basic circle of the scroll (r_b) (mm)		1.91
Thickness of the scroll (t) (mm)		3.0
Involutes angle of the scroll (φi) (degrees)		930
Scroll pitch (Tp) (mm)		12
Scroll wrap height (hs) (mm)		3.6
Experimental operating conditions		
Environmental conditions		Value
Condenser Temperature (℃)		54.4
Evaporator Temperature (℃)		-10/-5/0
Superheat (K)		20
Subcool (K)		0
temperature Out of gas cooler (℃)		20/35
Refrigerant		R744
STC operating speed		
Condition	Frequency setting (Hz)	Actual revolution (rpm)
MS Motor	60	3450

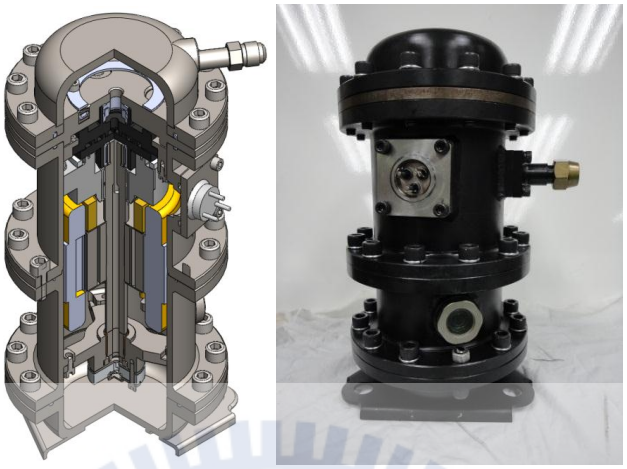

Fig. 5.19 3D model of R744 LPS STC and prototype for CO_2 bottle cooler

(a) Components of CO_2 bottle cooler LPS STC prototype

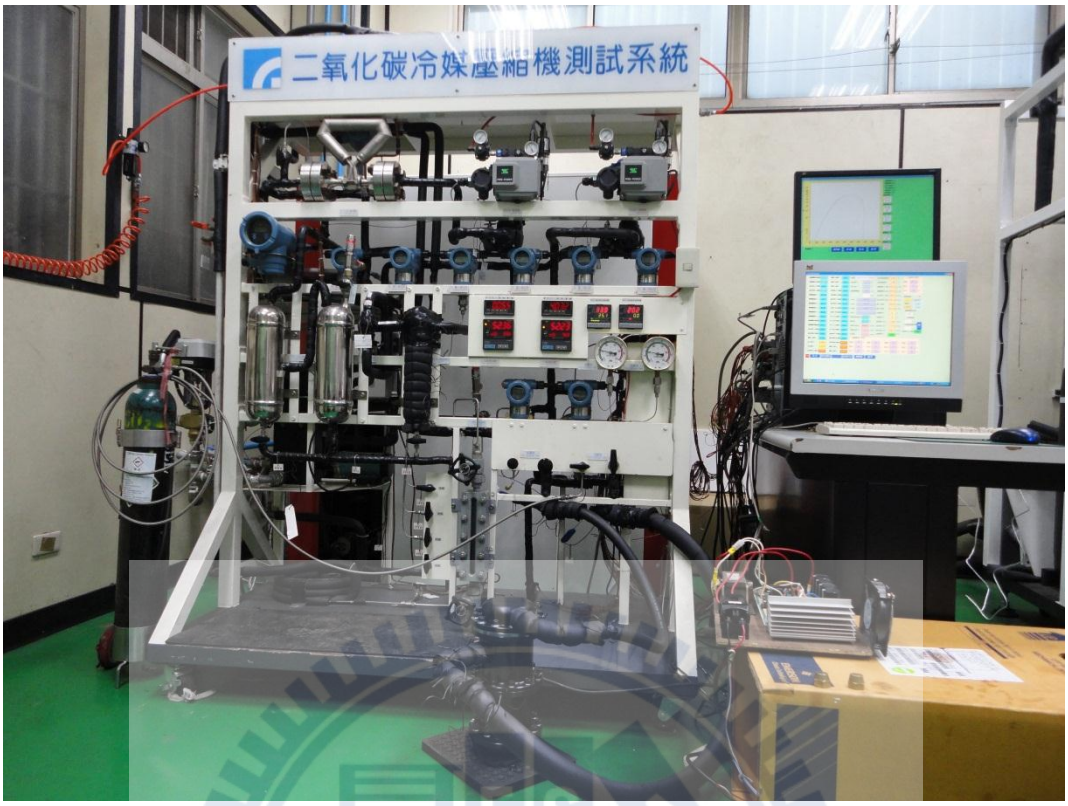

(b) Testing of CO_2 bottle cooler LPS STC prototype

Fig. 5.20 CO_2 bottle cooler LPS STC prototype

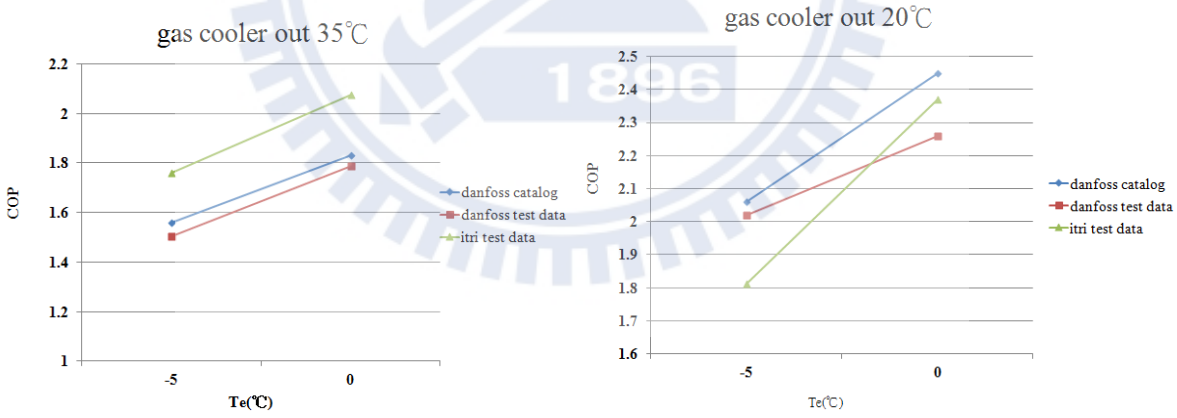

Fig. 5. 21 Test results of R744 CO_2 bottle cooler LPS STC prototype

CHAPTER 6 CONCLUSIONS AND FUTURE WORK

6.1 Conclusions

The main objective of this study is to comprehensively study the performance improvement potential of the low pressure side (LPS) STCs with the axial-compliance mechanism (ACM) both theoretically and experimentally. This objective has been accomplished by conducting a series of simulation and experimental studies. It has been found that the ACM is favorable in extended operating speed of the LPS STC.

In this research, several critical techniques for accomplishing a high-performance, variable-speed LPS STC with an ACM have been developed and investigated. Further, based on the well-developed STC mathematical model and the STC-performance computer simulation package, the leakage-control techniques for improving STC performance and providing wider operating capacities for a variable-speed STC have been developed, tested, and verified in this study.

First, the mathematical model of axial leakage value was constructed, and the advantages of this model were confirmed by numerical simulations and experimental validations with the developed ACM in an R22 LPS STC prototype. Second, several ACM design modules were constructed and integrated into the STC prototypes. Case studies demonstrated that the prototypes were powerful and offered advantages such as aiding in designing power-conserving STC products with extended operating considerations. Furthermore, one ACM design process concerning the different refrigerant applications in the LPS STC was formulated. Experimental studies were also conducted to evaluate its strengths and weaknesses.

Overall, this study provides important and comprehensive design information for the implementation of the ACM design technique in variable speed LPS STC applications under severe operating speeds and alternative refrigerants. The important contributions and accomplishments of this research are summarized as follows.

(1) The hypothesis assumed the axial clearance (δ) must be considerably smaller than the scroll thickness (b); i.e., $\delta/b << 1$. In this assumption, the mathematical leakage model shows that the length of leakage path and the pressure difference between the scroll suction side and discharge side are the two main parameters to the inner leakage effect.

(2) The value of 6 μm for axial clearance was obtained for the given geometry and operating condition for R22 STC by numerical simulations. The manner in which it can be affected by variation in geometrical and operating parameters is the most important aspect in this research for designing the ACM.

(3) The leaf spring's rigidity is depended on its thickness. In this study, the forces acting on a 0.8-mm-thick leaf spring can be decreased to nearly half of those acting on the 1.0-mm-thick one.

(4) The dynamic characteristics of a fixed scroll have been analyzed, simulations for measuring the displacement in the leaf spring and controlling the clearance between the fixed scroll and the orbiting scroll have been performed, and a new ACM for a STC has been developed.

(5) This new ACM is proposed for a R22 LPS STC and the compressor performance for the prototype has been measured. In the experiment results, the suspension-compliance mechanism functioned well when the prototype was under the standard compressor testing condition (ASHARE T), and its measured noise value was low.

(6) The suspension ACM functions well at operating speeds ranging from 80 Hz (condition E) to 40 Hz (condition A). The test results show that the overall COP of the R22 STC prototype increases from 4.7% to 13.5%.

(7) The limiting ring structure constrained the fixed scroll and limited it to movements only in the axial direction. In addition, the backpressure acting on the fixed scroll transferred its forces to the frame via springs and caused a sufficient downward sealing force, leading to COP enhancement by higher volumetric efficiency.

(8) The limiting ring prevented the scrolls from crashing, which led to reductions in the operating noise at extended operating speeds.

(9) The different refrigerants have different operating pressure differences. In this study, R22 refrigerant can be treated as the design baseline for other refrigerant applications and design of the ACM in LPS STCs should be determined with a focus on the backpressure mechanism.

(10) The axial clearance can be considered to be 6.0 μm in the R22, R410A applications.

(11) The axial clearance can be considered to be 3.0 μm in the R744 applications.

(12) The case studies of the ACM in R22, R410A, and R744 LPS STCs show a very good performance. The ACM design seems very suitable for all the refrigerants that can be used in the LPS STC.

6.2 Scope for the future work

Although the design of a high-efficiency STC with variable speed can be addressed by the leakage mathematical model and the simulation package constructed in this study, further research is required and certain issues must be resolved in the future.

(1) The LPS STC with the ACM has been initially verified by the study of the R22 STC with 5.5-in frame diameter. For more understanding of ACM design for different STC size, more backpressure mechanism design should be carried out to obtain enough data for modifying and correcting the ACM prototype models.

(2) The R410A STC with a 4.8-in frame size and R744 STC with a 4.4-in frame size have been described in this dissertation. Experiments for the other frame sizes in LPS STCs should also be carried out to validate the accuracy of the developed ACM models.

(3) The design of the ACM mechanism arrangements may not be optimum, for example, the constraint ring may cause frictional loss, and the suspension element can be simplified further via optimum geometric design. These effects may lower the compression efficiency. Therefore, the suitable mechanism arrangements and the parametric design of the ACM for different design requirements should be considered by using the optimization methods.

(4) The R744 LPS STC ACM design for the bottle cooler application is simply a case studied in this dissertation. Many other optimization problems can also be investigated, such as deriving the optimization thermal efficiency for the open-type showcase application and for the subcritical cycle frozen application.

(5) The presented ACM design is a limited mechanism design for maintaining the best scroll-axial clearance on the basis of the designed pressure difference. Therefore, further study of detail CAE simulation is necessary for solving the commercialize engineering.

REFERENCES

[1] **L. Cruex,** "Rotary Engine", U.S. Patent 801182, 1905.

[2] **J. L. Jones,** "Scroll Pump", U.S. Patent 2841089, 1958.

[3] **Y. Youn, N. K. Cho, B. C. Lee, and M. K. Min,** "The characteristics of tip leakage in scroll compressors for air conditioners", in Proc. of the 2000 Int. Compressor Conference at Purdue, pp. 797-806, 2000.

[4] **H. Li, Q. Liao, R. Wang,** "Research and development of variable-speed scroll compressor", in Proc. of the 2002 Int. Compressor Conference at Purdue, C24-4, July, 2002.

[5] **N. Ishii, M. Yamamura, H. Morokoshi, M. Fukushima, S. Yamamoto, and M. Sakai,** "On the superior dynamic behavior of a variable rotating speed scroll compressor", in Proc. of the 1988 Int. Compressor Conference at Purdue, pp. 75-82, July, 1988.

[6] **H. Richardson and G. Gatecliff,** "Comparison of the high side vs. low side scroll compressor design", in Proc. of the 1992 Int. Compressor Conference at Purdue, pp. 603-608, July, 1992.

[7] **Y. C. Chang, C. H. Tseng, G. D. Tarng, and L. T. Chang,** "Scroll compressor with solid axial sealing mechanism", in Proc. of the 4th International Conference on Compressor and Refrigeration, Xi'an City, China, pp. 189-196, October, 2003.

[8] **T. Qureshi and S. Tassou,** "Variable speed capacity control in refrigeration systems", Applied Thermal Engineering, 16, pp. 103-113,1996.

[9] **N. Ishii, M. Yamamura, H. Morokoshi, M. Fukushima, S. Yamamoto, and M. Sakai,** "On the superior dynamic behavior of a variable rotating speed scroll compressor", in Proc. of the Purdue International Compressor Engineering Conference, pp.75-82, 1988.

[10] **L. Hongqi, L. Quanping, and W. Ruixiang,** "Research and development of variable-speed scroll compressor", in Proc. of the Purdue International Compressor Engineering Conference, C24-4, 2002.

[11] **E. Morishita, M. Sugihara, and T. Nakamura**, "Scroll compressor dynamics (1st report, The model for the fixed radius crank)", Bulletin of JSME, 29 (248), pp. 476-482, 1986.

[12] **B. Wang, X. Li, and W. Shi,** "A general geometrical model of scroll compressors based on discretional initial angles of involute", International Journal of Refrigeration, 28, pp. 958-966, 2005.

[13] **K. Tojo, N. Ikegawa, N. Maeda, S. Machida, M. Shiibayashi, and N. Uchikawa,** "Computer modeling of scroll compressor with self adjusting back pressure mechanism", in Proc. of the Purdue International Compressor Engineering Conference, pp. 872-886, 1986.

[14] **J. J. Nieter, "**Dynamics of suction process", in Proc. of the Purdue International Compressor Engineering Conference, pp. 165-174, 1988.

[15] **M. Hayano, H. Sakata, S. Nagatomo, and H. Murasaki,** "An analysis of losses in scroll compressor", in Proc. of the Purdue International Compressor Engineering Conference,

pp.189-197, 1988.

[16] **H. Richardson and G. Gatecliff,** "Comparison of the high Side vs. low side scroll compressor design", in Proc. of the Purdue International Compressor Engineering Conference, pp. 603-610, 1992.

[17] **J. Lee, S. Kim, S. Lee, and Y. Park,** "Investigation of axial compliance mechanism in scroll compressor", in Proc. of the Purdue International Compressor Engineering Conference, pp. 459-464, 1996.

[18] **Y. C. Park, Y. Kim, and H. Cho,** "Thermodynamic analysis on the performance of a variable speed scroll compressor with refrigerant injection", International Journal of Refrigeration, 25, pp. 1072-1082, 2002.

[19] **Y. C. Chang, C. E. Tsai, C. H. Tseng, G. D. Tarng, and L. T. Chang,** "Computer simulation and experimental validation of scroll compressor", in Proc. of the Purdue International Compressor Engineering Conference, C016, 2004.

[20] **Y. Chen, N. Halm, J. Braun, and E. Groll,** "Mathematical modeling of scroll compressor -part II: overall scroll compressor modeling", International Journal of Refrigeration, 25, pp. 751-764, 2002.

[21] **N. -K. Cho, Y. Youn, B. -C. Lee, M. -K. Min,** "The characteristics of tangential leakage in scroll compressors for air-conditioners", in Proc. of the Purdue International Compressor Engineering Conference, Volume I, pp. 807-814, 2000.

[22] **P. Howell,** "Fluid mechanical modeling of the scroll compressor", Mathematics for Science and Engineering, Cambridge University Press, Cambridge, UK, pp. 32-56, 2001.

[23] **L. Liansheng,** "Scroll compressors. Mechanical industry", Beijing, China, 1998.

[24] **C. Schein and R. Radermacher,** "Scroll compressor simulation model", Journal of Engineering for Gas Turbines and Power of ASME, 123, pp. 217-225, 2001.

[25] **Y. Youn, N.-K. Cho, B.-C. Lee, and M.-K. Min,** "The characteristics of tip leakage in scroll compressors for air conditioners", in Proc. of the Purdue International Compressor Engineering Conference, Volume I, pp. 797-805, 2000.

[26] **T. Yanagisawa and T. Shimizu,** "Leakage losses with a rolling piston type rotary compressor II - leakage losses through clearances on rolling piston faces", International Journal of Refrigeration, 8, pp. 152-158, 1985.

[27] **E. W. Lemmon, M. O. McLinden, and M. L. Huber,** "REFPROP 8.0", NIST, MD, USA.

[28] **Y. C. Chang**, "Family design of scroll Compressors with Optimization", National Chiao Tung University, Ph.D. Dissertation, 2007.

[29] **Hsiao et al.,** "Scroll compressor with back pressure regulation mechanism", U.S. Patent 6,368,088Bl, 2002.

[30] **Y. Tang and C. Hung,** "Study of a novel compliant suspension mechanism in low side type scroll compressor", in Proc. of the Purdue International Compressor Engineering Conference, C1302, 2008,.

[31] **K. Tojo, M. Ikegawa, N. Maeda, S. Machida, M. Shiibayashi, and N. Uchikawa**, "Computer modeling of scroll compressor with self adjusting back-pressure mechanism", in Proc. of the International Compressor Engineering Conference at Purdue, pp. 872-885, 1986.

[32] **K. Suefuji, M. Shiibayashi, and K. Tojo, "**Performance analysis of hermetic scroll compressor", in Proc. of the International Compressor Engineering Conference at Purdue, pp. 75-84, 1992.

[33] **J. W. Bush, D. K. Haller, and C. R. Galante,** "General stability and design specification of the back-pressure supported axially compliant orbiting scroll", in Proc. of the International Compressor Engineering Conference at Purdue, pp. 853-860, 1992.

[34] **A. J. Marchese,** "Dynamics of an orbiting scroll with axial compliance, Part 2 experimental techniques", in proc. of the International Compressor Engineering Conference at Purdue, pp. 871-882, 1992.

[35] **J. Lee, S. Kim, S. Lee, and Y. Park,** "Investigation of axial compliance mechanism in scroll compressor", in proc. of the International Compressor Engineering Conference at Purdue, pp. 459-464, 1996.

[36]**Y. C. Park, Y. Kim, and H. Cho,** "Thermodynamic analysis on the performance of a variable speed scroll compressor with refrigerant injection", International Journal of Refrigeration, 25, pp. 1072-1082, 2002.

[37] **ANSYS**, ANSYS Workbench V.12 help.

[38] **ASHRAE Standard ANSI/AHRAE-23,** "ASHRAE Method of Testing for Rating Positive Refrigerant Compressor and Condenser Units", 1993.

[39] **S. Devotta, A. S. Padalkar, N. K. Sane**, "Performance assessment of HCFC-22 window air conditioner retrofitted with R-407C", Applied Thermal Engineering, 25, pp. 2937-2949, 2005.

[40] **K. Park and D. Jung,** "Performance of heat pumps charged with R170/R290 mixture", Applied Energy, 86, pp. 2598-2603, 2009.

[41] **B. O. Bolaji,** "Experimental analysis of reciprocating compressor performance with eco-friendly refrigerants", in Proc. of the Institution of Mechanical Engineers Part A: Journal of Power and Energy, 224, pp. 781-786, 2010.

[42] **M. Fatouh, T. A. Ibrahim, and A. Mostafa,** "Performance assessment of a direct expansion air conditioner working with R407C as an R22 alternative", Applied Thermal Engineering, 30, pp. 127-133, 2010.

[43] **B. O. Bolaji,** "Investigating the performance of some environment-friendly refrigerants as alternative to R12 in vapor compression refrigeration system", Ph.D. Thesis, Department of Mechanical Engineering, Federal University of Technology, Akure, Nigeria, 2008.

[44] **W. Chen,** "A comparative study on the performance and environmental characteristics of R410A and R22 residential air conditioners", Applied Thermal Engineering, 28, pp. 1-7,

2008.

[45] **E. Torrella, R. Cabello, D. Sanchez, J. A. Larumbe, and R. Llopis,** "On-site study of R22 substitution for HFC non-azeotropic blends (R417A, R422D) on a water chiller of a centralized HVAC system", Energy and Buildings, 42, pp. 1561-1566, 2010.

[46] **Bitzer,** Refrigerant Report, 13th ed., Bitzer International, 71065 Sindelfingen, Germany, 2007, http://www.bitzer.de (accessed 24.06.07).

[47] **B. O. Bolaji,** "Performance analysis of R12 alternatives in adiabatic capillary tube of a vapour compression refrigeration system", Engineering Review, 0, pp. 83-90, 2010.

[48] **ARI,** Soft-optimized system tests conducted with several possible R22 and R502 alternatives, Air-conditioning and Refrigeration Institute (ARI), Arlington, Virginia, USA, 1997.

[49] **J. Fernandez-Seara, F. J. Uhia, R. Diz, and J. A. Dopazo,** "Vapour condensation of R22 retrofit substitutes R417A, R422A and R422D on CuNi turbo C tubes", International Journal of Refrigeration, 33, pp. 148-157, 2010.

[50] **C. Aprea and A. Greco,** "An exergetic analysis of R22 substitution", Applied Thermal Engineering, 22, pp. 1455-1469, 2002.

[51] **C. Aprea, F. D. Rossi, A. Greco, and C. Renno,** "Refrigeration plant exergetic analysis varying the compressor capacity", International Journal of Energy Research, 27, pp. 653-669, 2003.

[52] **N. Ishii, K. Bird, K. Sano, M. Oono, S. Iwamura, and T. Otukura,** "Refrigerant leakage flow evaluation for scroll compressors", in Proc. of the International Compressor Engineering Conference at Purdue, Vol. II, pp. 633-638, 1996.

[53] **S. G. Kandlikar,** "Roughness effects at microscale – reassessing Nikuradse's experiments on liquid flow in rough tubes", Bulletin of the Polish Academy of Science, Technical Sciences, 53, 2005.

[54] **N. Ishii, S. Yamamoto, K. Sano, K. Sawai, A. Hiwata, T. Nakamoto, and H. Kawano,** "Efficiency simulations of a compact CO_2 scroll compressor and its comparison with same cooling capacity R410A scroll compressor", in Proc. of the International Compressor Engineering Conference at Purdue, C22-2, 2002.

[55] **N. Ishii, S. Kawamura, S. Yamamoto, K. Sawai, A. Hiwata, T. Nakamoto, H. Kawano, and K. S. Ting,** "Efficiency simulations with consideration of heat losses of R410 compact scroll compressor for its optimal performance", in Proc. of the International Compressor Engineering Conference at Purdue, C22-3, 2002.

[56] **N. Ishii, M. Sakai, K. Sano, S. Yamamoto, and T. Otokura,** "A fundamental optimum design for high mechanical and volumetric efficiency of compact scroll compressors", in Proc. of the International Compressor Engineering Conference at Purdue", Vol. II, pp. 639-644, 1996.

[57] **T. Oku, K. Anami, N. Ishii, C. W. Knisely, K. Yasuda, K. Sawai, K. Sano, and T.**

Morimoto, "Gas leakage in CO_2 and R22 scroll compressors and its use in simulations of optimal performance", in Proc. of the International Conference on Compressors and their Systems, pp. 403-412, 2005.

APPENDIX A-Patent research of axial-compliant sealing

Patent research of axial-compliant sealing

Axial-compliance patent list

Item	Types / Assignees	Sealing Element	Back gas pressure on orbiting scroll	Back gas pressure on fixed scroll	Pressing element
1	Individual Persons		US 5833442	US 3874827	
2	Arthur D. Little	US 3986799 US 3994633 US 3994635 US 3994636 US 4199308 US 4395205	US 3884599 US 3994633		
3	Hitachi Ltd.	US 4487560	US 4216661 US 4357132 US 4365941 US 4596520 US 4861245	US 5829959 US 6174150 US 6589035	
4	Trane Co.	US 4415317 US 4416597 US 4462771			
5	Sanden Corp.	US 4437820 US 4453899 US 4460321 US 4627799 US 4701115 US 4722676 US 4753583 US 4890987 US 4968232 US 5122041 US 5702241 US 6126421	US 5082432		
6	American Standard Inc.	US 6126422 US 6270713	US 4522575		
7	Mitsubishi Denki Kabushiki Kaicha	US 4564343 US 4732550 US 4740143 US 4824343		US 5743720 US 5846065	US 4846639
8	Toshiba		US 4696630		
9	Copeland			US 4767293 US 4877382 US 5102316 US 5156539 US 5482450 US 5580230	
10	Iwata Air Comperessor Co. (Anest Iwata Corp.)	US 4869658 US 6179590			
11	Tecumseh		US 4884955 US 5088906 US 5131828 US 6139294 US 6168404		US 5383772
12	Carrier Corp.	US 5383772	US 4938669 US 4992032 US 4993928 US 5040956 US 5085565 US 5090878 US 5145345 US 5256044 US 5873711 US 6149413 US 6517332		
13	Toyoda	US 5076771 US 5364247 US 5545020 US 5547353			
14	MHI	US 6585501		US 5186616 US 5257920 US 5447418	
15	General Motor Corp.	US 6074185			
16	Sanyo Electric Co.		US 5252046	US 5242284	
17	ITRI				US 5277563 US 5474433 US 5527166 US 6048184 US 6368088
18	Goldstar Co.				US 5487653 US 5540572

19	Matsushita Electric Industrial Co., Lt	US 5562434	US 5848883 US 5630712		US 5520526 US 5951272
20	LG Electronics , Inc.			US 5562435 US 5823757	
21	Nippondenso Co.	US 5580228 US 6074141			
22	Bristol Compressors, Inc.		US 5588820 US 5593295	US 6030192	
23	Air Squared, Inc.	US 5632612 US 6511308			
24	Scroll Technologies		US 5989000 US 6077057 US 6224059 US 6290478 US 6527528 US 6554592	US 6309197 US 6416301	
25	Varian, Inc.	US 6068459			
26	Mind Tech Corp.	US 6071101			
27	Rechi Precision Co., Ltd.			US 6537044	US 6257852
28	Fujitsu General, Ltd.		US 6389837 US 6561776		
29	Dakin Industries, Ltd.		US 6533561	US 6514060	

Mathematical model of sealing path

B-1 Scroll profile

As the involute curve is generated on the basis of a base circle (see Fig. A-1), the mathematical equations for the involute curve can be obtained using simple trigonometry. The equations can be obtained by referring to the following figure. The involute starts from the base circle.

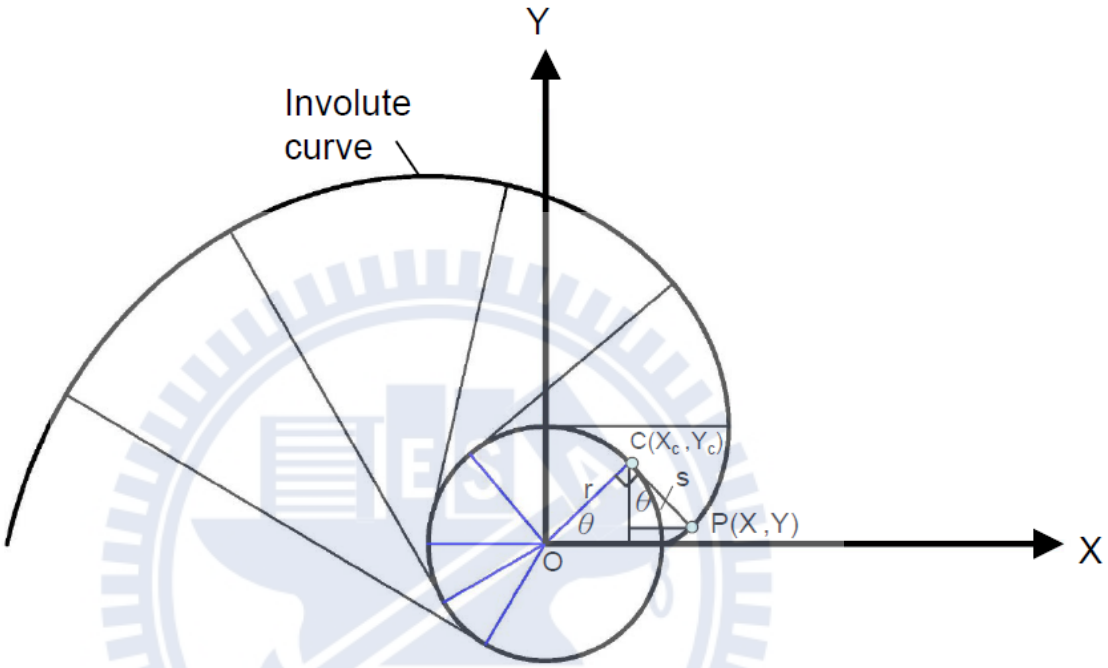

Fig. B-1 Development of involute curve

From two similar triangles, we obtain the following:

$$Xc = r\cos\theta \qquad X = Xc + s\sin\theta$$
$$\text{and} \qquad \text{(B-1)}$$
$$Yc = r\sin\theta \qquad Y = Yc - s\cos\theta$$

Here, $s = r\theta$

Then, the curve can be defined as

$$\begin{cases} X = r\cos\theta + r\theta\sin\theta \\ Y = r\sin\theta - r\theta\cos\theta \end{cases} \qquad \text{(B-2)}$$

The above equation can represent a moving line for a cutting tool (see the following figure).

The tooling radius is set as k, following equation (A-2), and the scroll wrap profile can be defined as follows:

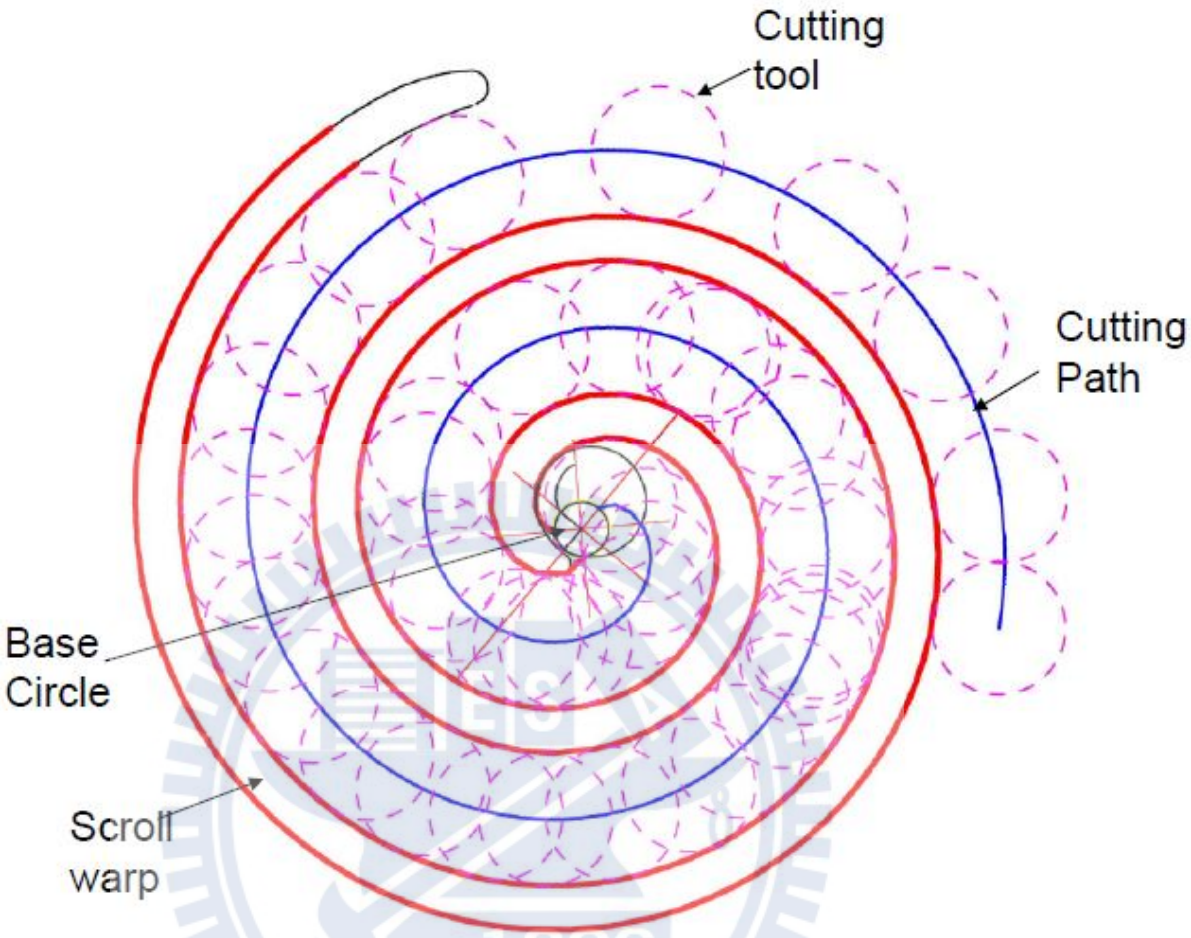

Fig. B-2 Movement path of cutting tool

The center of the cutting tool is $S_1(X_1Y_1)$; then, the path can be represented as

$$R_1 = \begin{bmatrix} X_1 \\ Y_1 \end{bmatrix} = \begin{bmatrix} r\cos\phi + r\phi\sin\phi \\ r\sin\phi - r\phi con\phi \end{bmatrix} \quad \text{(B-3)}$$

The coordinate of any point on the outer surface of the cutting tool can be represented as

$$R_3 = \begin{bmatrix} X_3 \\ Y_3 \end{bmatrix} = \begin{bmatrix} k\cos\theta \\ k\sin\theta \end{bmatrix} \quad \text{(B-4)}$$

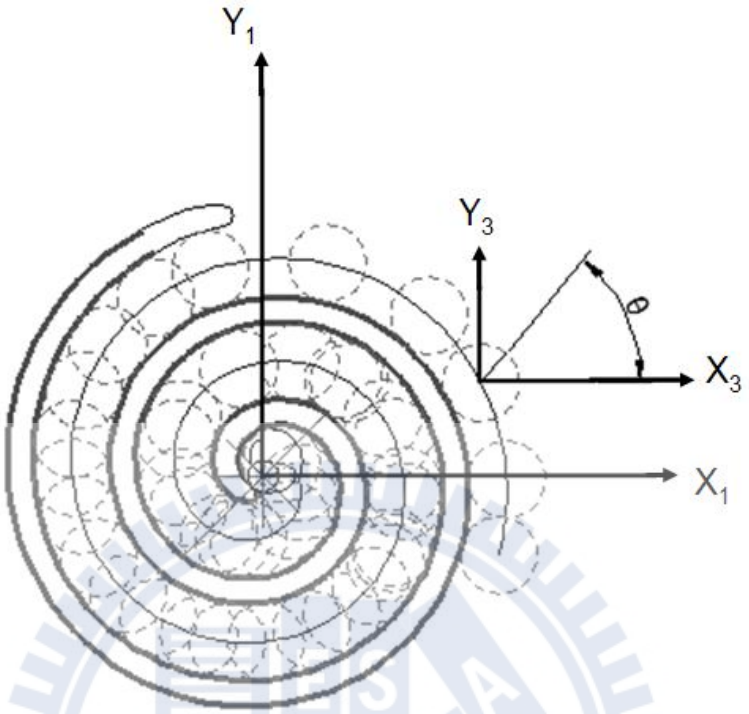

Fig. B-3 Coordinate of any point on outer surface of cutting tool

Thus, coordinate S_3 is transferred to the fixed coordinate S_1 as

$$R_{1c} = \begin{bmatrix} X_1 + X_3 \\ Y_1 + Y_3 \end{bmatrix} = \begin{bmatrix} r\cos\phi + r\phi\sin\phi + k\cos\phi \\ r\sin\phi - r\phi\cos\phi + k\sin\phi \end{bmatrix} \tag{B-5}$$

The scroll is fixed (the velocity is 0) while the tool moves with velocity V_2

$\because$

$$V_2 = \frac{dR_{1c}}{dt} = \frac{dR_{1c}}{d\phi}\frac{d\phi}{dt} = \omega\frac{dR_{1c}}{d\phi} = \omega\begin{bmatrix} r\phi\cos\phi \\ r\phi\sin\phi \end{bmatrix} \tag{B-6}$$

$\therefore$

$$V_{12} = V_1 - V_2 = -\omega\begin{bmatrix} r\phi\cos\phi \\ r\phi\sin\phi \end{bmatrix} \tag{B-7}$$

Then,

$$n_1 = \begin{bmatrix} -\cos\theta \\ -\sin\theta \end{bmatrix} \tag{B-8}$$

From the theory on involute gear meshing, we obtain

$$n_1 \bullet V_{12} = 0 \tag{B-9}$$

From equation (A-8) & (A-7), we obtain the result as follows:

$$r\phi\cos(\theta - \phi) = 0 \qquad \text{or} \qquad \theta = \phi \tag{B-10}$$

The above equation is the round cutter and scroll meshing function.
From the above equations, we can express the fixed scroll wrap functions as follows:

$$\begin{cases} R = \begin{bmatrix} r_b\cos\phi + r_b\phi\sin\phi + r\cos\theta \\ r_b\sin\phi - r_b\phi con\phi + r\sin\theta \end{bmatrix} \\ \theta = \phi \end{cases} \tag{B-11}$$

As the cutting tool forms the inner and outer scroll wrap profiles simultaneously, the inner cutting point is opposite to the outer cutting point and they are angled 180° from each other. Then, they can be represented as

$$\begin{cases} R_{io} = \begin{bmatrix} r_b\cos\phi + r_b\phi\sin\phi + r\cos\theta \\ r_b\sin\phi - r_b\phi con\phi + r\sin\theta \end{bmatrix} \\ \theta = \phi \end{cases} \tag{B-12}$$

Further,

$$\begin{cases} R_{fo} = \begin{bmatrix} r_b\cos\phi + r_b\phi\sin\phi + r\cos(\theta + \pi) \\ r_b\sin\phi - r_b\phi con\phi + r\sin(\theta + \pi) \end{bmatrix} \\ \theta = \phi \end{cases} \tag{B-13}$$

The orbiting scroll is moving around the fixed scroll, and thus, the equations of the orbiting scroll can be represented as

1. Inner orbiting scroll profile:

$$\begin{cases} R_{oi} = [M_\Phi]\begin{bmatrix} r_b\cos\phi + r_b\phi\sin\phi + r\cos\theta \\ r_b\sin\phi - r_b\phi con\phi + r\sin\theta \end{bmatrix} + [R_\beta] \\ = \begin{bmatrix} r_b\cos(\phi+\Phi) + r_b\phi\sin(\phi+\Phi) + r\cos(\theta+\Phi) + L_b\cos\beta \\ r_b\sin(\phi+\Phi) - r_b\phi\cos(\phi+\Phi) + r\sin(\theta+\Phi) + L_b\sin\beta \end{bmatrix} \\ \theta = \phi \end{cases} \quad \text{(B-14)}$$

In this equation, the assembly phase angle of the fixed scroll and the orbiting scroll is Φ and the orbiting bias is L_b. The orbiting angle of the orbiting scroll is β.

In addition, the transfer matrix ($[M_\Phi]$) and the moving vector of the orbiting scroll ($[R_\beta]$) are

$$[M_\Phi] = \begin{bmatrix} \cos\Phi & -\sin\Phi \\ \sin\Phi & \cos\Phi \end{bmatrix} \quad \text{(B-15)}$$

and

$$[R_\beta] = \begin{bmatrix} L\cos\beta \\ L\sin\beta \end{bmatrix} \quad \text{(B-16)}$$

2. Outer orbiting scroll profile:

$$\begin{cases} R_{oo} = [M_\Phi]\begin{bmatrix} r_b\cos\phi + r_b\phi\sin\phi + r\cos\theta \\ r_b\sin\phi - r_b\phi con\phi + r\sin\theta \end{bmatrix} + [R_\beta] \\ = \begin{bmatrix} r_b\cos(\phi+\Phi) + r_b\phi\sin(\phi+\Phi) + r\cos(\theta+\Phi+\pi) + L\cos\beta \\ r_b\sin(\phi+\Phi) - r_b\phi\cos(\phi+\Phi) + r\sin(\theta+\Phi+\pi) + L\sin\beta \end{bmatrix} \\ \theta = \phi \end{cases} \quad \text{(B-17)}$$

B-2 Contact analysis of scrolls

From the definition of meshing equations, we know that the condition of scroll contact is that the scroll profile position vector should equal the scroll profile normal vector at the contact point. Further, the scroll profile position vector should equal the scroll profile tangential vector at the contact point.

$$R_f = R_o \tag{B-18}$$

$$n_f = n_o \tag{B-19}$$

$$\tau_f = \xi\tau_o \Rightarrow \frac{\tau_{fx}}{\tau_{ox}} = \frac{\tau_{fy}}{\tau_{oy}} = \xi \tag{B-20}$$

Fixed scroll outer profile contact with orbiting scroll inner profile:

$$R_{fo} = R_{oi} \Rightarrow$$
$$\begin{Bmatrix} r_b\cos\phi_1 + r_b\phi_1\sin\phi_1 + r\cos\theta_1 = r_b\cos(\phi_4+\Phi) + r_b\phi_4\sin(\phi_4+\Phi) - r\cos(\theta_4+\Phi) + L\cos\beta \\ r_b\sin\phi_1 - r_b\phi_1\cos\phi_1 + r\sin\theta_1 = r_b\sin(\phi_4+\Phi) - r_b\phi_4\cos(\phi_4+\Phi) - r\sin(\theta_4+\Phi) + L\sin\beta \end{Bmatrix} \tag{B-21}$$
and
$\theta_1 = \phi_1$
$\theta_4 = \phi_4$

For the tangent vector of fixed scroll and orbiting scroll at the contact point,

$$\begin{aligned} &\because R_{fo} = R_{oi} \\ &X_{fo} = X_{oi} \\ &Y_{fo} = Y_{oi} \\ &\therefore \\ &\frac{\frac{\partial X_{fo}}{\partial\theta_{fo}}}{\frac{\partial X_{oi}}{\partial\theta_{oi}}} = \frac{\frac{\partial Y_{fo}}{\partial\theta_{fo}}}{\frac{\partial Y_{oi}}{\partial\theta_{oi}}} \end{aligned} \tag{B-22}$$

Fixed scroll inner profile contact with orbiting scroll outer profile:

$$R_{fi} = R_{oo} \Rightarrow$$

$$\left\{\begin{array}{l} r_b \cos\phi_2 + r_b\phi_2 \sin\phi_2 + r\cos\theta_1 = r_b\cos(\phi_3+\Phi) + r_b\phi_3\sin(\phi_3+\Phi) + r\cos(\theta_3+\Phi) + L\cos\beta \\ r_b \sin\phi_2 - r_b\phi_2 \cos\phi_2 + r\sin\theta_2 = r_b\sin(\phi_3+\Phi) - r_b\phi_3\cos(\phi_3+\Phi) + r\sin(\theta_3+\Phi) + L\sin\beta \end{array}\right\} \quad \text{(B-23)}$$

and

$$\theta_2 = \phi_2$$

$$\theta_3 = \phi_3$$

For the tangent vector of the fixed scroll and the orbiting scroll at the contact point,

$$\because R_{fi} = R_{oo}$$

$$X_{fi} = X_{oo}$$

$$Y_{fi} = Y_{oo}$$

$$\therefore \quad \frac{\dfrac{\partial X_{of}}{\partial\theta_{of}}}{\dfrac{\partial X_{oo}}{\partial\theta_{oo}}} = \frac{\dfrac{\partial Y_{of}}{\partial\theta_{of}}}{\dfrac{\partial Y_{oo}}{\partial\theta_{oo}}} \quad \text{(B-24)}$$

The above equations can make up the contact equation, which are non-linear simultaneous equations. The unknowns are $\phi_1, \phi_2, \phi_3, \phi_4, \theta_1, \theta_2, \theta_3, \theta_4$, L, Φ, and β. If the orbiting angle (β) and the orbiting bias (L) are given, the contact coordinate can be calculated.

B-3 Sealing line calculation

According to the above contact analysis, the radial sealing line is the involute line between two contact points. Further, this involute line section can be called the radial leakage line.

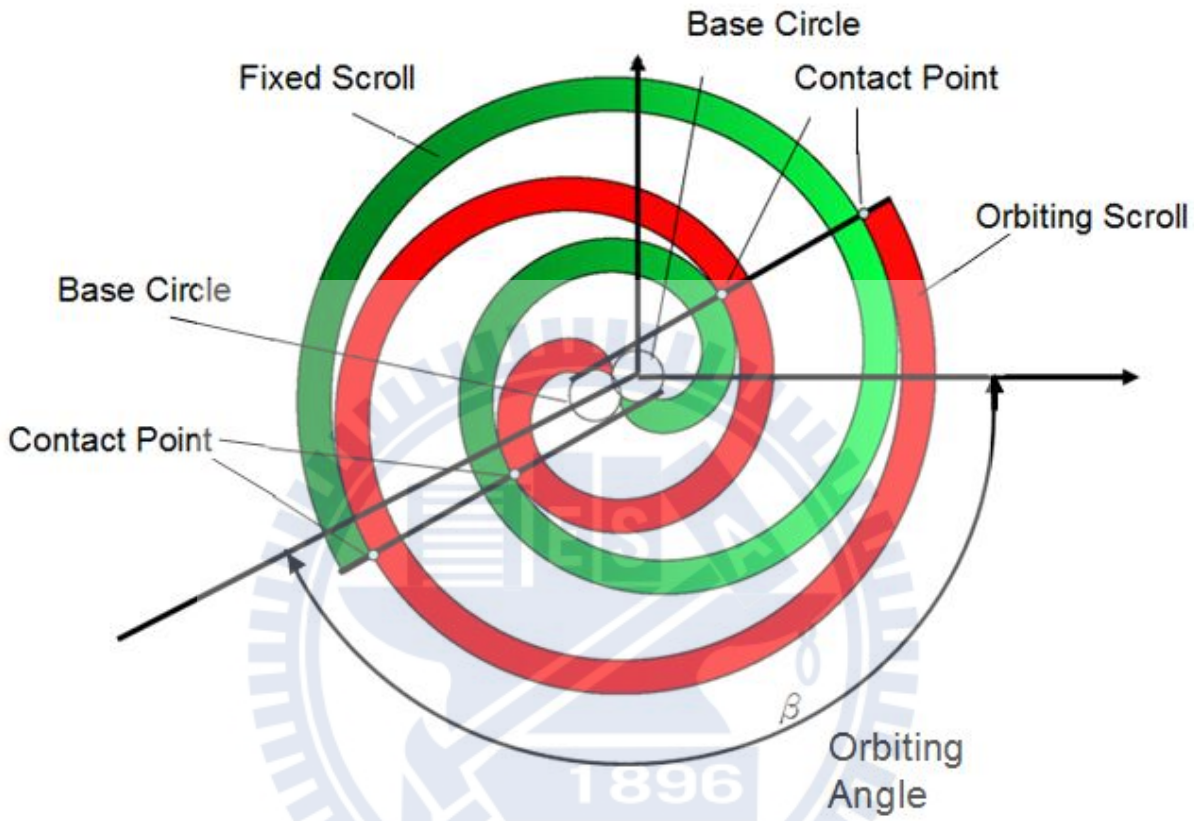

Fig. B-4 Inner and outer profiles of fixed scroll

$$\left|\overline{dL}\right| = \Delta l = \sqrt{dx^2 + dy^2} = \sqrt{\left(\frac{dx}{d\phi}\right)^2 + \left(\frac{dy}{d\phi}\right)^2}\, d\phi \qquad \text{(B-25)}$$

From the involute extension angles ($\phi_1, \phi_2, \phi_3, \phi_4$), the length of a sealing line between two angles ϕ_1 and ϕ_2 can be calculated as

$$l = \int_{\phi_1}^{\phi_2} \sqrt{\left(\frac{dx}{d\phi}\right)^2 + \left(\frac{dy}{d\phi}\right)^2}\, d\phi \qquad \text{(B-26)}$$

To simplify the calculation, the leakage line is based on half-ring leakage paths that are equivalent to the original involute leakage line. The scroll wrap thickness (t) is equivalent to the mean radius (rm) ± the half-wrap thickness (t/2), whereas the mean radius (rm) is l/2l (Fig. 3).

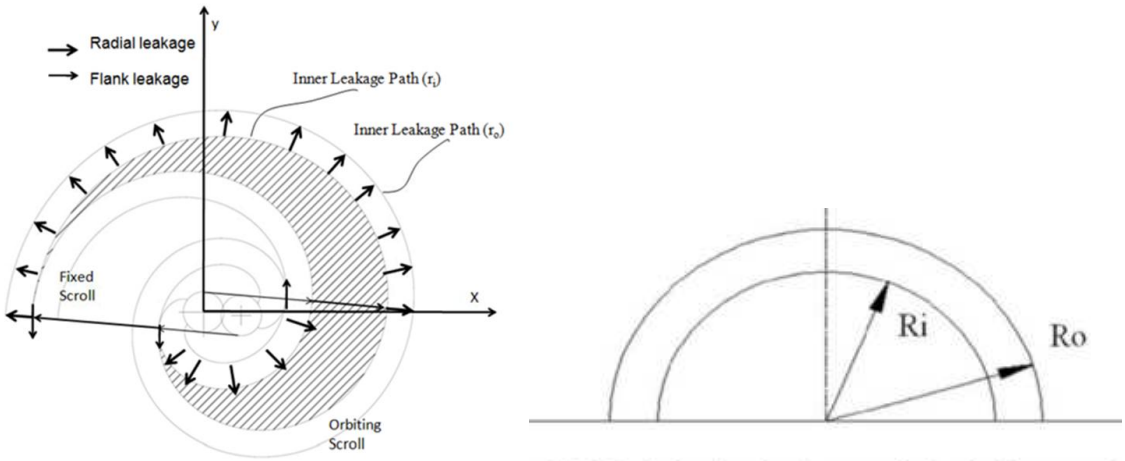

Fig. B-5 Half-ring leakage paths

$$R_i = \frac{l}{2\pi} - r_b\beta = \frac{l}{2\pi} - \frac{t}{2} \quad \text{(B-27)}$$

$$R_o = \frac{l}{2\pi} + r_b\beta = \frac{l}{2\pi} + \frac{t}{2} \quad \text{(B-28)}$$

B-4 Case study of sealing line calculation:

Table B- 1 Scroll parameters

Parameter	Value
Base circle radius (r_b)	1.9099 (mm)
Bias eccentricity (L)	3 (mm)
Orbiting angle (β)	120°

Fig. B-6 Orbiting angle (r) from 60° to 120°

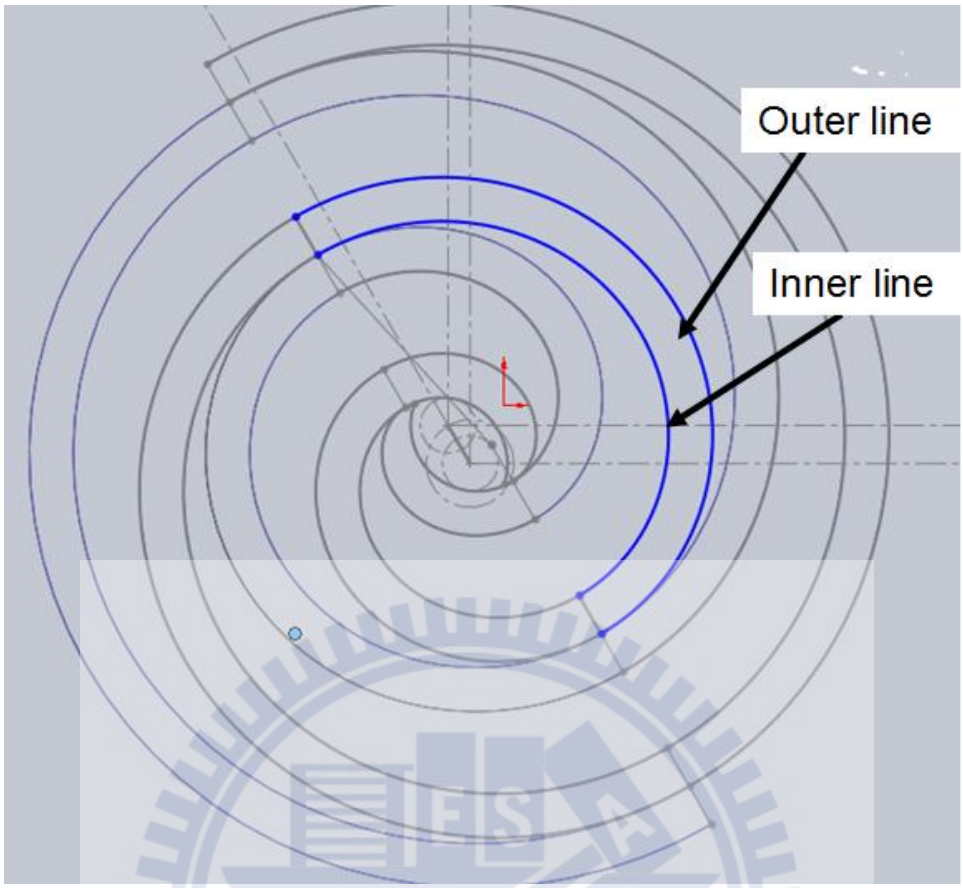

Fig. B-7 Scroll sealing lines

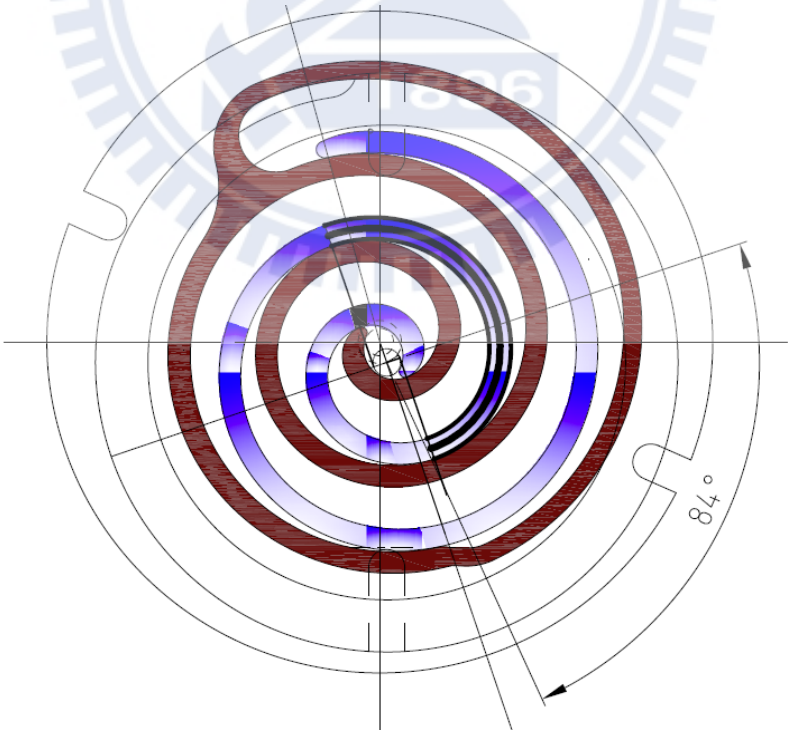

Fig. B-8 Section of center sealing line (black curve)

$$L_{leakage,center} = \int_{\phi_1}^{\phi_2} r_b \phi d\phi = \frac{1}{2} r_b \phi^2 \Big|_{\phi_1}^{\phi_1+\pi} = r_b \pi \phi + \frac{1}{2} r_b \pi^2 \quad \text{(B-29)}$$

$\phi_1 = 45° + 360° + 84° = 489°$

$\phi_2 = \phi_2 + \pi = 669°$

$L_{leakage,center} == r_b \pi \phi_1 + \frac{1}{2} r_b \pi^2 = 60.637(mm)$

$$R_i = \frac{60.637}{2\pi} - \frac{3}{2} = 8.15 \quad \text{(B-30)}$$

$$R_o == \frac{60.637}{2\pi} + \frac{3}{2} = 11.15 \quad \text{(B-31)}$$

$$L_{leakage,circle} = 2\pi \bar{r} = 2\pi \times \left(\frac{8.15 + 11.15}{2} \right) = 60.632$$

$L_{leakage,center} \fallingdotseq L_{leakage,circle}$

The calculate error of the length of circle leakage path and involute leakage path:

(60.637-60.632)/100=0.00005%

Computer added engineering (CAE) for the scroll deformation

C-1 Introduction

The computer added engineering (CAE) method was introduced to check the deformations of scrolls caused by the compressed refrigerant pressure and temperature. First of all, once the profile of fixed scroll and the orbiting scroll was designed, the compression chamber limited the deformation of scroll by the pressure and thermal condition (also called operating condition). Second, here, the presented CAE simulations for the understanding to the interference by scroll deformation. The results help to determine the thickness of soft surface coating on scrolls. For this coating, after the run-in of the scroll compressor, the scrolls will built its optimum axial clearance. In this dissertation, the optimum axial clearance maintained by the axial-compliance mechanism (ACM) was checked by the finite element method. All the scroll designs has consider the coating engineering. The following sections will show a case study for finding the suitable coating thickness (20 μ m).

C-2 Boundary conditions

The boundary conditions of compression chamber pressures and temperatures were calculated by the software, STC-performance simulation package, and the harsh condition is the moment of discharge. The boundary condition on compression chambers is shown in Fig. C-1. From the center of the scroll to the outer side, the pressure and temperature are distributed as high to low by radial direction. In this study, the high pressure is the discharge pressure of 8.6 MPa and the high temperature is the discharge temperature of 112℃. The low pressure and temperature are suction situation of 3.2MPa and 20℃. The middle pressure condition is 6.8MPa. The coordinate system is setting along the scroll profile by Z, X and Y (i.e.Θ). And the positive vertical direction (+Z) is downward to the feet of compressor (see fig. 1.1) as shown in fig. C-2.

The material of the scrolls is FC300.

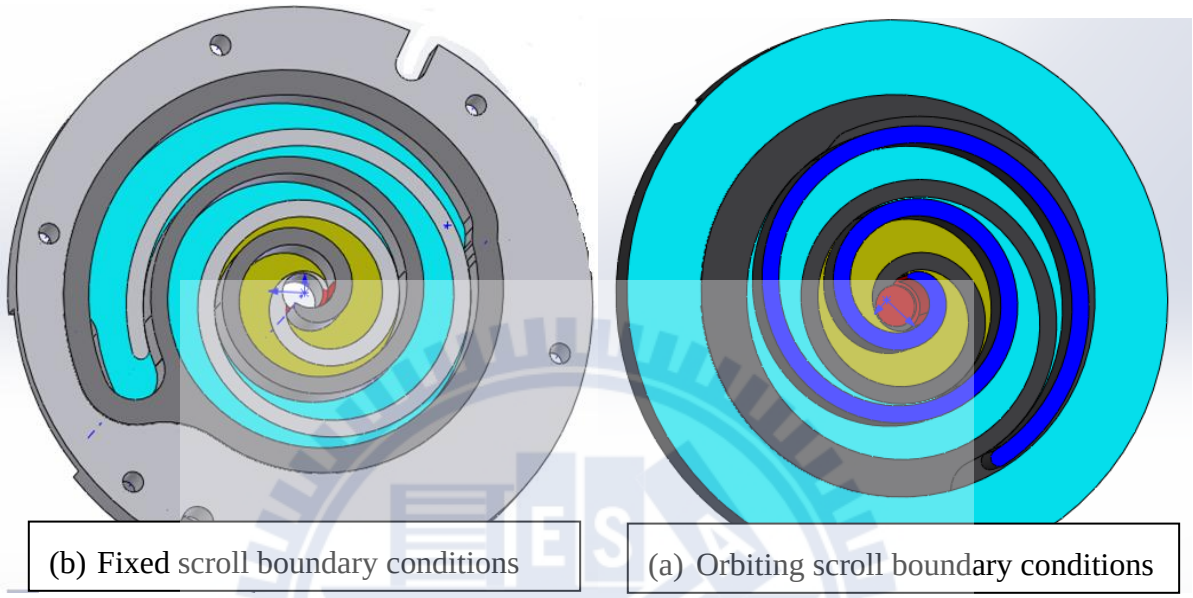

(b) Fixed scroll boundary conditions

(a) Orbiting scroll boundary conditions

Fig. C- 1 The scroll chamber for boundary condition setting

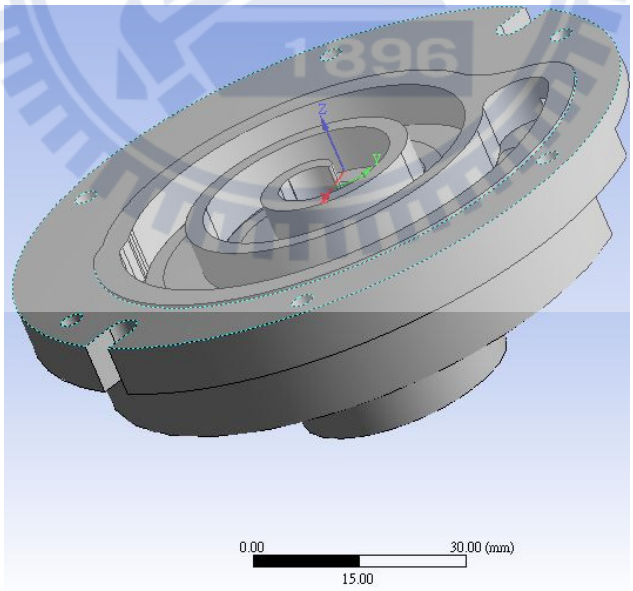

Fig. C-2 The coordinate system setting

C-3 Case study results

The simulation results shown in fig. C-3~fig.C-5.

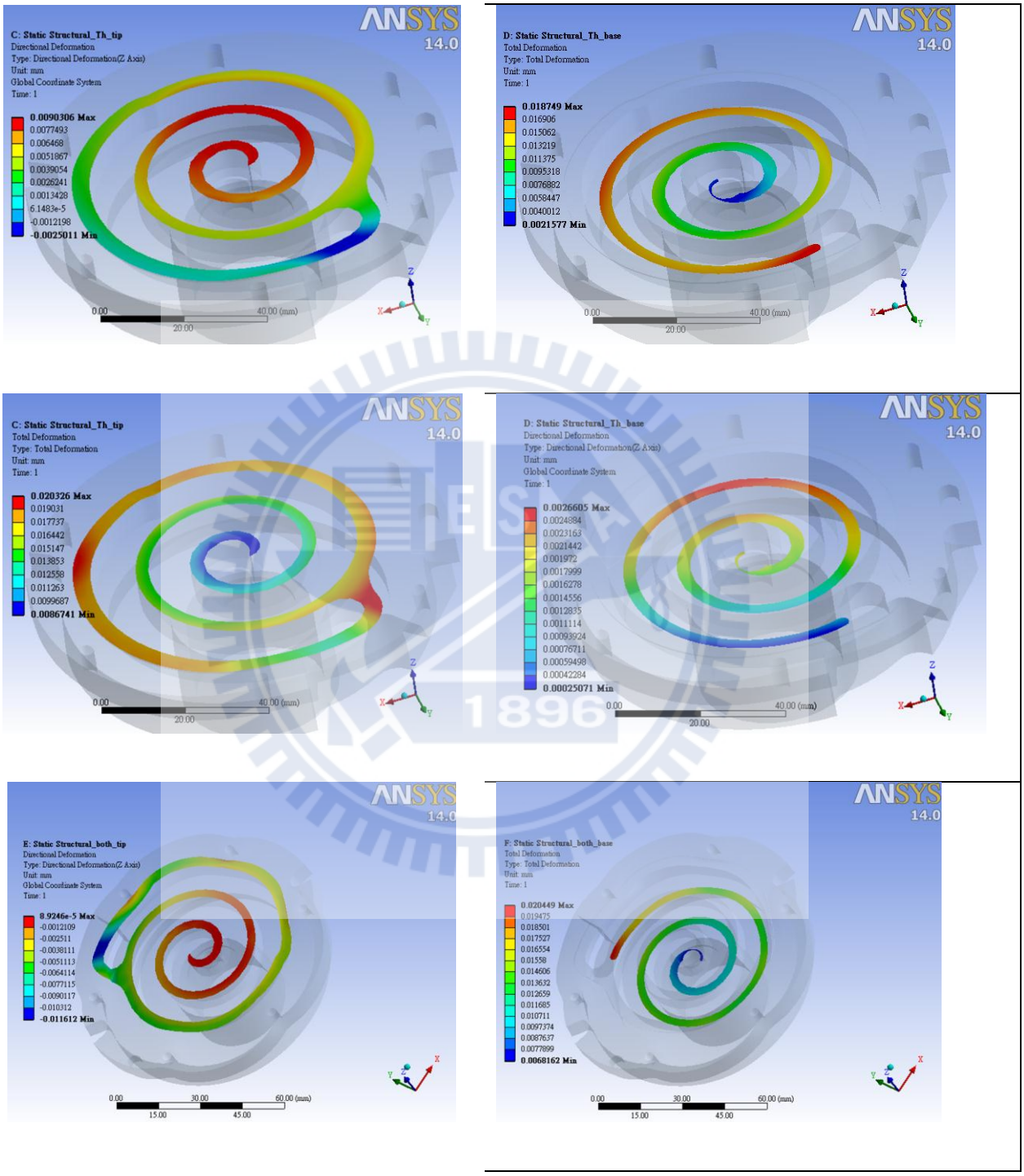

Fig. C- 3 Simulation results I

The z direction deformations of fixed scroll tip and base plate, the total deformations of fixed scroll tip and base plate, the z direction deformations of orbiting scroll tip and base plate, the total deformations of orbiting scroll tip and base plate, all of them are only thermal deformations and deformations by both thermal and forces (from pressures).

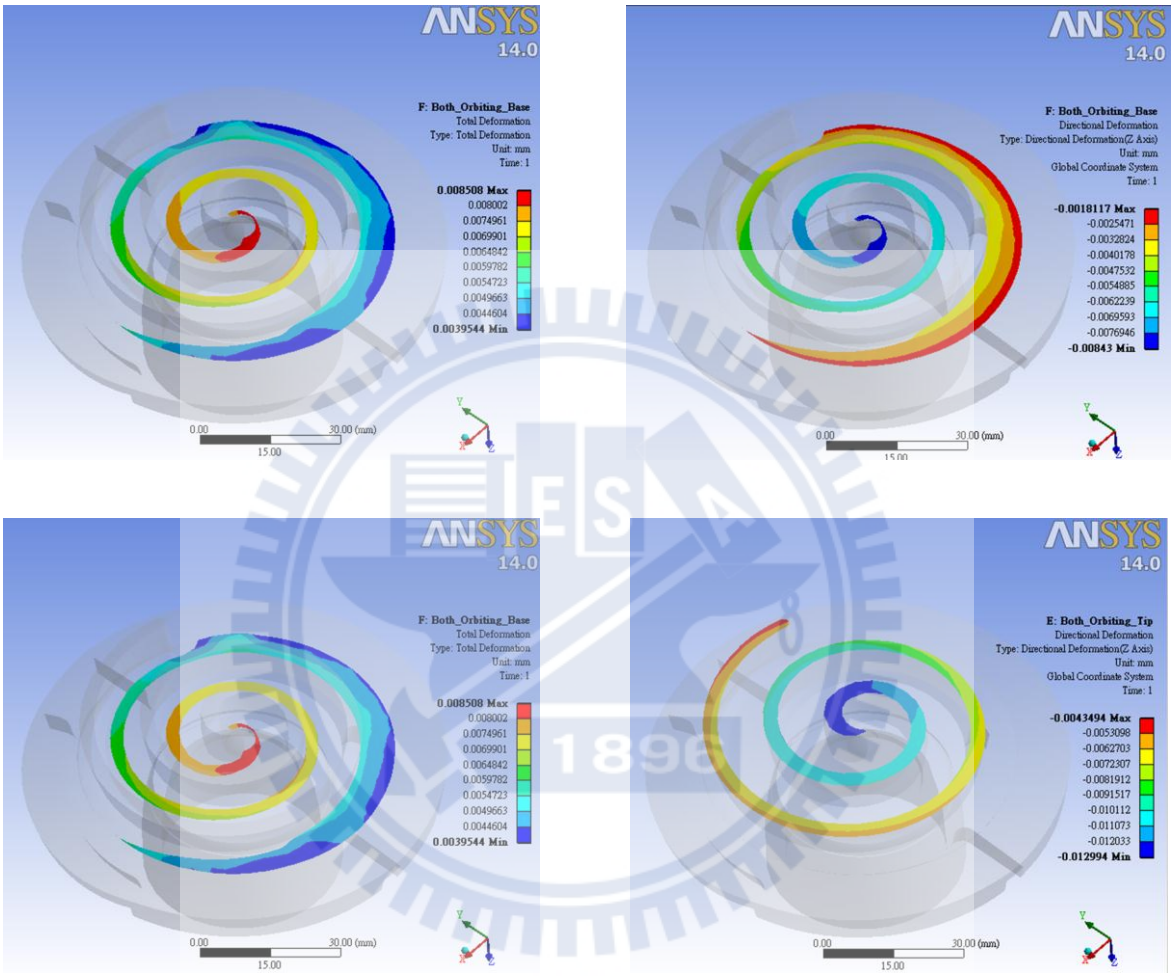

Fig. C- 4 Simulation results II

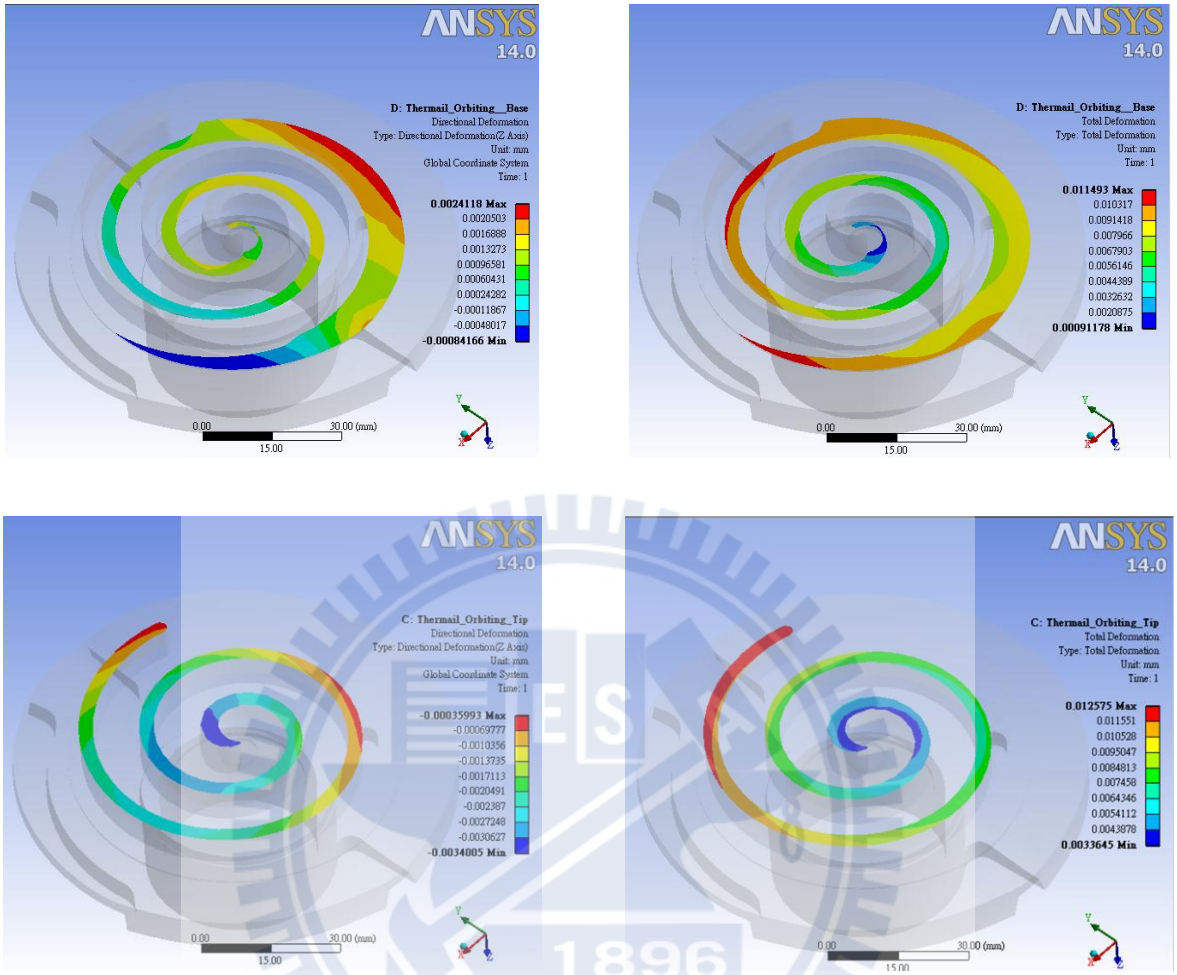

Fig. C- 5 Simulation results II

From the results of C-3~C-5, the interference of scrolls from the deformations can be obtained as showing on fig. C-6~C-7. Also, the maximum deformation may within±0.02mm, and the actual interference of scrolls may within 0.006mm.

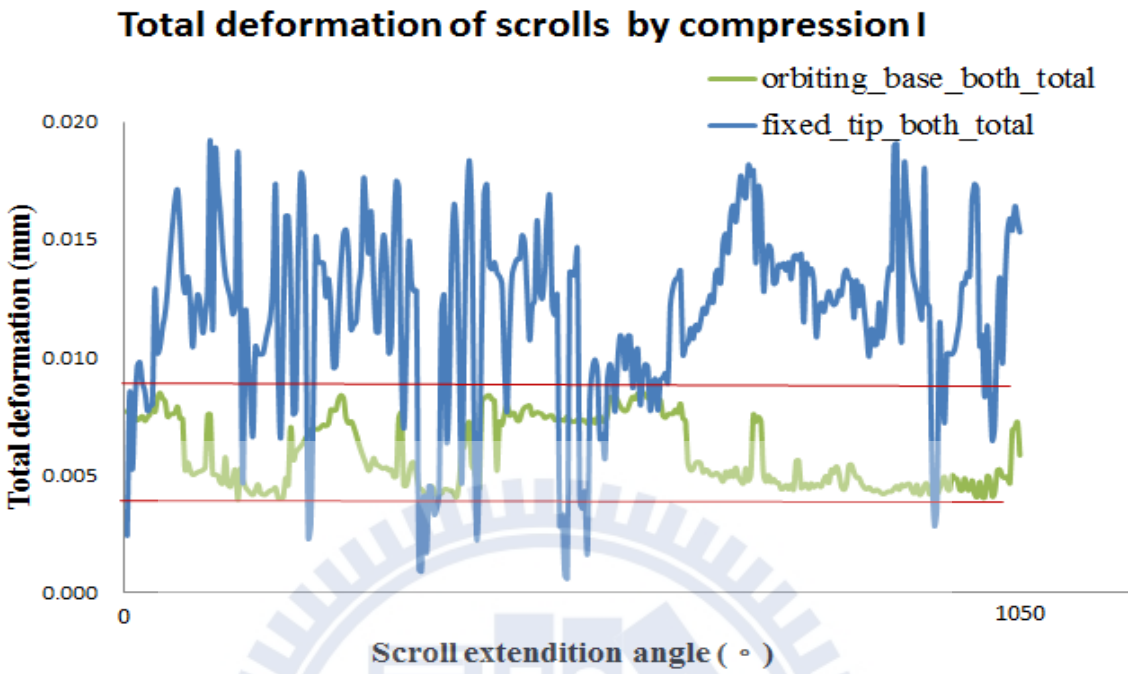

Fig. C- 6 The interference from deformations I

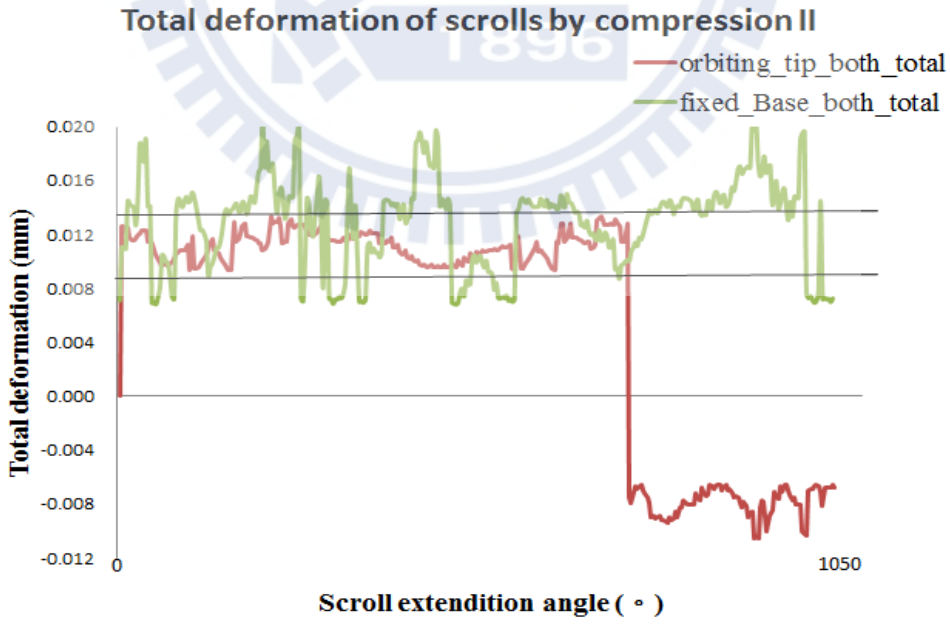

Fig. C- 7 The interference from deformations I

C-4 Discussions

From the case study, the thickness of soft coating of the scrolls can be found, and all of the simulation results can help the compressor designer to design optimum scroll pumps by considering the special run-in action of scrolls. That is to say, the axial –compliance mechanism can only consider the axial forces balancing and adjustment under the steady-state thermal conditions.

Technical specifications of CO_2 Compressor test rig

D-1 OBJECTIVE

ITRI needs calorimeters for testing the efficiency and lifespan of hermetic compressors using CO_2 as the refrigerant. Key design criteria for the desired calorimeter operational range are as follows:

- Operation in transcritical pressure region, i.e., the suction pressure should be below the critical pressure and the discharge pressure should be above the critical pressure
- Evaporation temperature range: -40℃to +15℃.
- Suction superheat range: 0–32 K.
- Discharge pressure range: 70–160 bars.

This report describes a test stand for testing compressors in the desired operating range.

D-2 DESCRIPTION OF PROCESS CYCLE

The described test stand is nearly identical to the current SINTEF calorimeter. It was designed to provide maximum flexibility with respect to testing aspects influencing CO_2 compressors, such as those mentioned below.

- Variation of the suction and discharge pressure. Lower and upper limits are 10 bars and 150 bars, respectively
- Variation of the suction superheat from 0 to 50 K
- Lubricant discharge separation and metering
- Dynamic pressure measurement in a compressor cylinder
- Measurement of compressor efficiencies
- CO_2 mass flow rates from 0.1 to 2 kg/min

The test rig is primarily designed for gas cycle operation, i.e., operation in the superheated gas region, as shown in Fig. D-2. See further explanation in section D-2. Operation with evaporation is also possible, but the heating capacity and evaporator area (TB-2 and HX-2, Fig. D-1) are

limiting factors in this respect.

The load stand consists of five main units:

- The process cycle loop
- The lubricant separation and return loop
- The heat rejection loop.
- The suction gas temperature adjustment loop
- The instrumentation, monitoring, and data acquisition system.

A schematic of the load stand demonstrating all significant components is shown in Fig. D-1, and a description of the function of each unit is given later in this chapter.

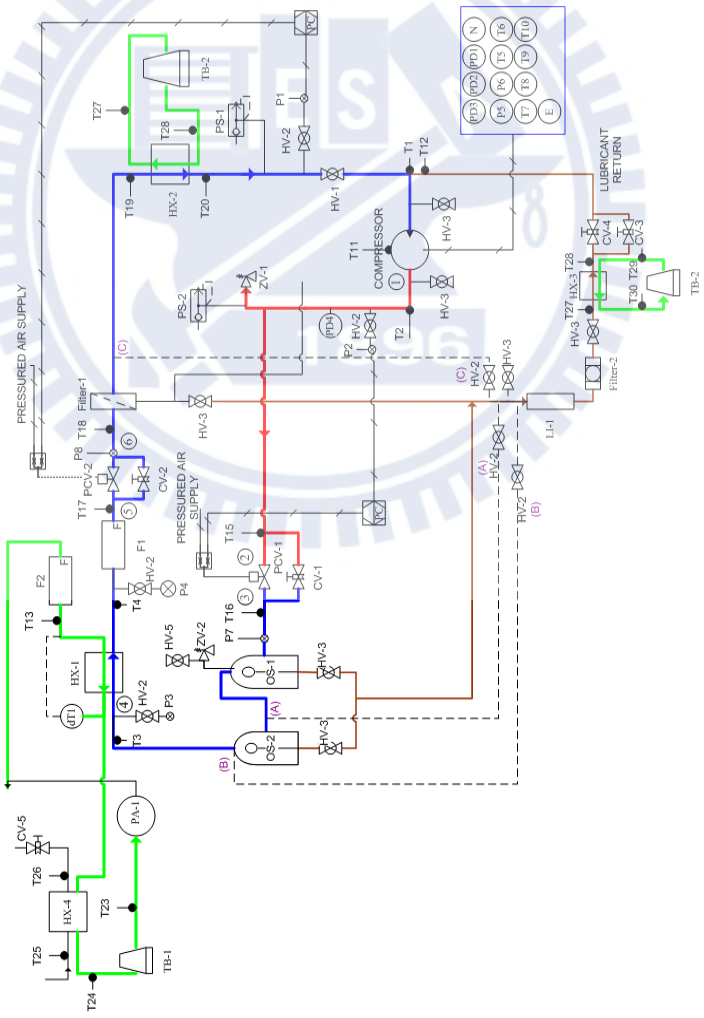

Fig. D-1 Schematic of load stand

D-3 DESCRIPTION OF PROCESS CYCLE LOOPS

The process cycle loop is determined in three different pressure ranges:

1. The discharge pressure section, from state point 1 to state point 2 in Fig. D-1 and Fig. D-2, has a maximum operating pressure of 15 MPa. This consists of an insulated stainless steel tube with an OD/ID ratio of 8/6 (mm).
2. The intermediate pressure section, from state points 3 to 5, has a maximum operating pressure of 10 MPa. It consists of lubricant separators OS1 and OS2 and heat exchanger HX-1 for cooling or heating CO_2, connected with a stainless steel tube with OD/ID of 10/8 (mm).

The separators OS-1 and OS-2 also perform the function of storing refrigerant gas and dampening the pressure pulses created by the compressor. Typical operating pressure varies between 7.5 and 9.0 MPa, and operating temperature range is between 35 and 100℃. If the temperature goes below the critical temperature for CO_2—31℃—condensation can occur in the receivers and liquid CO_2 may be drained with the lubricant. The separators are not insulated, and considerable heat loss can occur at high discharge temperature.

HX-1, from state points 4 to 5, is normally operated as a gas cooler and for calorimetric calculation of CO_2 mass flow. To improve the calculation accuracy, it is essential to have as large a temperature (enthalpy) differential as possible in/out of the gas cooler. As can be seen in Fig. D-2, the difference can be increased by insulating the separators. In our operation range, the accuracy has been satisfactory without separator insulation. However, in a new test rig designed for testing one-stage fractional HP size compressors only, insulating the separators is recommended for increasing the temperature difference in HX-1.

With the present peripheral cooling/heating system, TB-1, it is also possible to increase the CO_2 temperature in HX-1 (from 4-5) by heating the gas. This is useful in tests with low discharge temperature because operation to the left of the saturation curve is undesirable during normal

operation or if larger enthalpy difference is desired for improving the measurement accuracy.

3. The suction pressure section, from state points 6 to 1, has a maximum operating pressure of 10 MPa. It consists of a filter, Filter-1, and a heat exchanger, HX-2, connected with OD/ID 10/8 (mm) tubing.

Filter-1 serves as a potential CO_2 liquid droplet and lubricant separator.

HX-2 heats or cools the suction gas to the desired compressor inlet temperature.

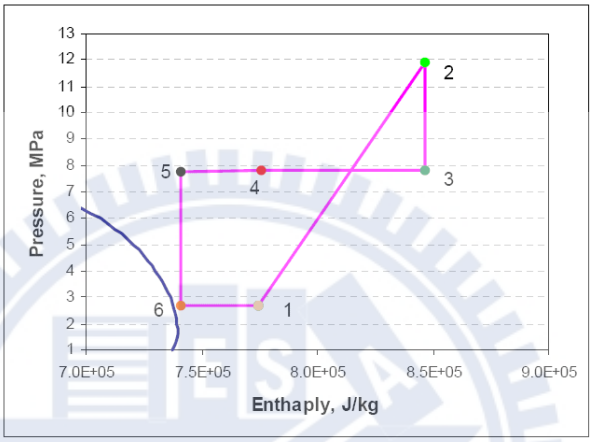

Fig. D-2 Normal process cycle with state point notation in a logarithmic-pressure enthalpy diagram. The saturation border is shown in the left corner.

D-4 DATA ACQUISITION

All the sensors are connected to a data acquisition system including a monitoring computer. The measured static values are logged by a Fluke 34970A data logger. An Excel-based data acquisition and reduction program is used for processing and recording data. The dynamic values are measured by means of a National Instruments data acquisition board (AT-MIO-16E_10) linked to a Lab-windows/CVI program in the PC.

The load stand is shown below.

Fig. D-3Test rig for compressor long-term (life) testing

AUTHOR'S PUBLICATION LIST

1. REFERED PAPERS

1. **Yuehju Tang**, Chinghua Hung, Yuchoung Chang, "Performance improvements in low side scroll compressor with extended operation speeds", Applied Thermal Engineering Volume 31 (2011), P. 3542~3551 (published)
2. Yangguang Liu, **Yuehju Tang**, Yuchoung Chang, Yaubin Yang, "Optimum design of scroll profiles created from involute of circle with variable radii by using finite element analysis", Mechanism and Machine Theory Volume 55 (2012), P. 1–17 (published)

2. CONFERENCE PAPERS

1. **YUEH-JU TANG,** YU-CHOUNG CHANG, CHUN-CHUNG YANG, "A Study of Design 35RT Aluminum Alloy Scroll Compressor" **in**: Purdue International Compressor Engineering Conference Proceedings (2006), C-6(18), pp. C031, USA.
2. **YUEH-JU TANG,** YU-CHOUNG CHANG, CHINGHUA HUNG, **"**Study of a Novel Compliant Suspension Mechanism in Low Side Type Scroll Compressor", in: Purdue International Compressor Engineering Conference Proceedings (2008), pp. C1302, USA.
3. **YUEH-JU TANG,** CHINGHUA HUNG**,** BIENDE SHEN**,** YU-CHOUNG CHANG, ROBERT YIE-ZU HU, **"**Structure Design and Analysis for Leaf Spring Type Axial Compliant Mechanism of Scroll Compressor", in: Proceedings of the 4th ACRA (Asian Conference on Refrigeration and Air-conditioning) (2009), #166, Taipei.
4. Yang Guang Liu, Chinghua Hung, **Yueh Ju Tang,** Ling-Yu Chao, "Scroll Compressor Simulation Program and Optimization", in: Proceedings of 7th International Conference on Compressor and Coolants, (2009), pp.446~453, Slovak.
5. **YUEH-JU TANG,** YANG GUANG LIU, "Development of a R744 Low Side Variable Speed Scroll Compressor for Bottle Cooler" **in**: Purdue International Compressor Engineering Conference Proceedings (2012), #1249, USA.

3. PATENTS

1. **湯岳儒,** 黃淑娥, 余培煜, 張鈺炯, "動力裝置及其組合結構", 中華民國專利, 發明, 專利號 I322226, 2010 年 4 月.
2. 梁坤億, 黃淑娥, 楊錞忠, **湯岳儒,** 張鈺炯, 劉陽光, "渦卷式壓縮機", 中國大陸, 發明, 專利號 ZL200810000283.4, 2010 年 12 月.
3. 梁坤億, 黃淑娥, 楊錞忠, **湯岳儒,** 張鈺炯, 劉陽光, "渦卷式壓縮機", 中華民國, 發明, 專利號 I353418, 2011 年 12 月.
4. Kun-Yi Liang, Shu-Er Huang, Chun-Chung Yang, **Yueh-Ju Tang,** Yu-Choung Chang, Yang-Kuang Liu," Structure for controlling lubricant's flow rate in scroll compressor", U.S. Patent 7,736,135, Jun. 15, 2010.

4. OTHERS

1. 湯岳儒,淺談汽車空調用渦卷式壓縮機技術,冷凍空調與熱交換,(75),pp.17-23, 2006 年 10 月.
2. 湯岳儒,二氧化碳汽車空調系統之研究進展,冷凍空調與熱交換, (76), pp.13-19, 2007 年 1 月.
3. 湯岳儒　微型渦卷式壓縮機的性能解析　「冷凍空調與熱交換」, (78), pp.1-6, 20070501
4. 湯岳儒　渦卷式壓縮機平衡機構設計　「冷凍空調與熱交換」, (82), pp.1-11, 20080116
5. 湯岳儒,蔡慶營　二氧化碳冷媒壓縮機性能測試探討　「冷凍空調與熱交換」,(87), pp.1~8,　20081115
6. 湯岳儒　,"淺談渦卷壓縮機之並聯應用",冷凍空調與熱交換, (91), pp.1-8, 20090715
7. 湯岳儒, "渦卷壓縮機排量調節關鍵技術專利簡介",冷凍空調&能源科技雜誌, (61), pp.29-43, 20100203
8. 楊堯斌,湯岳儒,張鈺炯　,"應用有限元素法於商業用渦卷式壓縮機的關鍵零組件開發",冷凍空調與熱交換, (97), pp.8-17,20100701
9. 王柏欽,湯岳儒,"　高壓冷媒磨耗試驗簡介",冷凍空調與熱交換, (103), pp.29-39, 20111118
10 湯岳儒,"　2011 年倫敦城市大學 7th 國際壓縮機與系統研討會紀要 ",冷凍空調與熱交換,(103),pp.61-75,2011111
11 湯岳儒　,"淺談天然冷媒渦卷壓縮機於冷藏設備之應用 ", 冷凍空調&能源科技雜誌,(72),pp.17-32,20111210

VITA

姓名: 湯岳儒 (Tang,Yueh-Ju)

生日: 民國 61 年 12 月 24 日

籍貫: 台灣省新竹市

學歷:

台北市立中正高中	1988/9~1991/6
私立淡江大學機械工程學系學士	1992/9~1996/6
國立雲林科技大學機械工程學系碩士	1999/9~2001/6
國立交通大學機械工程學系博士班	2004/9~2013/1(預計)

經歷:

光寶科技股份有限公司影像事業部雷射印表機研發專案工程師 2001~2002

士林電機(廠)股份有限公司機器事業處開關技術部研發工程師 2002~2005

工業技術研究院能源與資源研究所熱流技術組壓縮機研究室 2005~2006

工業技術研究院能源與資源研究所冷凍空調與電能技術組壓縮機研究室 2006~2007

工業技術研究院能源與環境研究住商節能商技術組節能關鍵元件研究室 2007~2010

工業技術研究院綠能與環境研究所智慧節能系統技術組機電系統研究室 2010~ 2012

工業技術研究院綠能與環境研究所智慧節能系統技術組空調系統研究室 2012.10~

現職:

工業技術研究院綠能與環境研究所智慧節能系統技術組空調系統研究室

能源專案計畫子項計畫主持人 2009~ 2012

科專跨領域前瞻計畫主持人 2012~

101

博士論文

渦卷壓縮機軸向順從機構設計與應用之研究

交通大學 工學院
機械工程學系

湯岳儒